Fall 2016

Development and Implementation of High Fidelity Human Models for the Investigation of Blast and Non-Penetrating Projectile Impact

Candice F. Cooper
University of New Mexico

Candice F. Cooper
Candidate

Mechanical Engineering
Department

This thesis is approved, and it is acceptable in quality and form for publication:

Approved by the Thesis Committee:

Dr. Tariq Khraishi, Chairperson

Dr. Paul Taylor

Dr. Yu-Lin Shen

DEVELOPMENT AND IMPLEMENTATION OF HIGH FIDELITY HUMAN MODELS FOR THE INVESTIGATION OF BLAST AND NON-PENETRATING PROJECTILE IMPACT

by

CANDICE F. COOPER

B.S., BIOLOGY, UNIVERSITY OF NEW MEXICO

THESIS

Submitted in Partial Fulfillment of the
Requirements for the Degree of

Master of Science
Mechanical Engineering

The University of New Mexico
Albuquerque, New Mexico

December, 2016

DEDICATION

To the man who provided tremendous support throughout this endeavor, Ryan Kamm. Without your encouragement and genuine belief in my capabilities my path would have been much different. Thank you, truly.

ACKNOWLEDGEMENTS

I would like to thank my advisor, Dr. Khraishi, for assisting in my not-quite-traditional transition from an undergraduate degree in biology to my master's degree in mechanical engineering, Dr. Shen for accepting me into the program with confidence in my ability to make said transition and for agreeing to serve on my committee, and Dr. Taylor for creating an opportunity which allowed me to begin my career at Sandia National Laboratories and for the endless hours spent providing me with the guidance necessary to complete this research.

This research was funded by the Laboratory Directed Research and Development program at Sandia National Laboratories. I gratefully acknowledge the support of my colleagues and management at Sandia National Laboratories without which I wouldn't have had the opportunity to conduct this research. Sandia National Laboratories is a multi-program laboratory managed and operated by Sandia Corporation, a wholly owned subsidiary of Lockheed Martin Corporation, for the U.S. Department of Energy's National Nuclear Security Administration under contract DE-AC04-94AL85000. SAND2016-10410 T.

Development and Implementation of High Fidelity Human Models for the Investigation of Blast and Non-Penetrating Projectile Impact

by

Candice F. Cooper

B.S., Biology, University of New Mexico, 2013

M.S., Mechanical Engineering, University of New Mexico, 2016

ABSTRACT

Military operations abroad have highlighted the effects of several types of physical traumas including traumatic brain injury and behind armor blunt trauma. While previous approaches toward understanding and mitigating trauma caused by blast or blunt impact relied upon physical testing of animal subjects, post mortem human subjects, or human tissue surrogates, recent advances in computational capability have spurred a growing area of research in computational investigations into wound injury and its mitigation. The development of high-fidelity human torso and head-neck-torso models are presented here. These models are employed in blast and non-penetrating projectile impact simulations in order to demonstrate the value of the models and the associated simulation approach in assessing potential wound injury mechanisms and conducting relative merit assessments of armor designs. Also, a study comparing truncated head-neck and torso models to the more complete head-neck-torso model is conducted in order to assess the appropriateness of employing truncated models. The results of this study suggest that, in general, the use of truncated models does not necessarily capture the complete physical behavior of blast impact in comparison to the more complete head-neck-torso model and full human models may be invaluable to future research of physical trauma.

Contents

List of Figures

List of Tables

Nomenclature

ICP	Intracranial Pressure
TBI	Traumatic Brain Injury
CSF	Cerebrospinal Fluid
PMHS	Post Mortem Human Subject
BABT	Behind Armor Blunt Trauma
HN	Sandia National Laboratories Head-Neck model
HNT	Sandia National Laboratories Head-Neck-Torso model
EOS	Equation-of-State
CTH	Sandia Shock Wave Physics Simulation Computer Code (not an acronym)
M-G	Mie-Gruneisen
T-B	Tillotson-Brundage
FMJ	Full Metal Jacket
TI	Transversely Isotropic
RMSD	Root Mean Square Deviation

1 Introduction

Recent military operations abroad have highlighted the disastrous effects of physical traumas such as traumatic brain injury and behind armor blunt trauma. These physical traumas have spurred great interest in understanding wound injury mechanisms and assessing body armor effectiveness within the research community. Several approaches are taken by the research community toward this end including a large subset of physical experimentation utilizing various test objects such as live animals, human cadavers, animal tissue and organs, human tissue and organs, and human tissue surrogates. Many difficulties are associated with utilizing these test objects in physical experimentation such as keeping biological tissues in post mortem environments that maintain tissue properties and biomechanical behaviors consistent with that of living tissue or quantifying the deviation between animal tissue and human tissue responses in order to produce results that are relevant to research directed at the human condition. It is also often the case that these test objects can only be utilized once during testing, resulting in small test samples or large costs. The development of high fidelity human models and a modeling and simulation approach toward investigating wound injury mechanisms and conducting merit assessments of body armor provides an appealing addition to this research area.

The research presented here describes the development of high fidelity human torso and head-neck-torso models as well as a simulation methodology with which to conduct in-silico wound injury investigations. This modeling and simulation approach presents a significant advantage over physical experimentation by providing a simulation capability

with which to investigate wound injury mechanics and to optimize armor designs while reducing the need for extensive field testing. Furthermore, this approach can be conducted ad infinitum without the use of human cadavers, animal testing, or expensive physical surrogates. These wound injury simulation results can be post-processed to provide stress, strain, energy, stress power, acceleration, and damage measures at as many sites within the virtual model as desired; quantities that are not easily measured, especially at a large number of sites, within physical surrogates when exposed to blast or blunt impact.

It is often the case in biomechanical research employing a modeling and simulation approach that truncated models are utilized for the sake of simplicity. This allows researchers to focus on a region of interest while eliminating the need to create overly extensive models which incorporate regions outside of the particular region of interest, and in doing so, reducing computational expense. While it is desirable to utilize truncated models, it is important to assess potential boundary effects and investigate whether or not a truncated model captures the complete physical response to a given condition relative to a more complete model. Research on the utilization of a truncated torso model and a truncated head-neck model in comparison to the more complete head-neck-torso model is also presented here. This research is foundational in achieving a multiphase objective toward creating a full human male model.

2 Historical Review

Head and thoracic trauma can occur as a result a variety of events such as blast impacts, projectile impacts, motor vehicle accidents, and sports injuries. Computational modeling and simulation has become an increasingly powerful tool with which to study the traumas associated with these injurious events and to research possible mitigation techniques.

Several truncated head models have been developed and employed in computational studies within the past several years. Moore et al. [1], Chafi et al. [2], Rezaei et al. [3],Tan et al.[4], and Cotton et al. [5] have all utilized truncated head models to assess blast impacts. Moore et al. [1] suggests a comparison between a 50% lethal dose blast relative to lung injury with a concussive injury. Chafi et al. [2] illustrates the ability of their model to predict intracranial pressure (ICP) as well as shear and principal strains and highlights the difficulty of identifying specific ICP thresholds that would lead to traumatic brain injury (TBI). Rezaei et al. [3] employ their head model in the investigation of blast impact within open and confined spaces and their results show that the walls of a confined space enhance the risk of blast injuries due to reflective waves creating numerous increases in ICP. Tan et al. [4] studied the impact of complex waves usually caused by multiple blast sources. They utilized a truncated head model equipped with a helmet and assessed the effect of multiple blast directions and detonation sequences.

Cotton et al. [5] introduce a model generation methodology which they employ to create a head model of high bio-fidelity. The model generation methodology suggested by Cotton et al. is similar to the methodology described previously by Taylor et al. [6,7] in

creating a high fidelity head model, employed by Cooper et al. [8] in creating a high fidelity torso model, and also utilized in creating the models presented here.

Haniff et al. [9] employed the head model developed by Taylor et al. [6] to investigate the phenomena of blast induced cavitation within the fluid filled regions of the brain. They then created microscale models of the superior sagittal sinus to research cavitation bubble collapse as a potential damage mechanism. Blast induced cerebrospinal fluid (CSF) cavitation as a potential injury mechanism has also been studied previously by Panzer et al. [10].

Likewise, several truncated torso models have also been developed and employed in computational investigations of blast and blunt impact. Goumtcha et al. [11] investigated a single blast impact to a truncated torso model and Zhou et al. [12] employed a simplified torso model to investigate blast in complex environments with various wall arrangements. Cooper et al. [8] and Taylor et al. [7] have previously described the development and utilization of the truncated torso model described here for both blast and blunt impact studies. To research blunt trauma, Shen et al. [13] developed both human and swine torso models and validated these models against testing conducted on swine subjects and historical data from post mortem human subject (PMHS) impact tests respectively.

Roberts et al. [14–16] has developed a truncated torso model which they have employed to study non-penetrating ballistic impact and behind armor blunt trauma (BABT). By use of this method, Roberts et al. has suggested that the current National Institute of Justice standard for ballistic resistance of personal body armor may not be suitable to protect

against BABT [15]. BABT has also been studied employing clay or gelatin by coupling experimental and numerical approaches [17,18]. Physical experiments researching BABT have been conducted using PMHS by Bass et al. [19] and using swine test subjects by Gryth et al, Sonden et al, and Kunz et al [20–22] respectively.

High fidelity combined head-neck-torso models or full human models have not yet been developed as extensively as truncated head or torso models. The more complete models that have been developed often have less fidelity with respect to the internal organs and are generally utilized in the research of events leading to large rigid-body motion such as automobile accidents. Gayzik et al. have developed a simplified full body model in the seated position [23] as well as a higher fidelity full body model in the seated position [24] for future use in injury prediction and prevention simulations. Shigeta et al. [25] have developed a high-fidelity human model in both the seated and standing positions for use in predicting organ injury due to impact events typically seen in automobile accidents.

Computational studies of physical trauma comprise a vast and growing research area as evidenced by the extensive array of research and development conducted relatively recently. The use of truncated models is common throughout the research community. This is an issue that has not been investigated thoroughly and part of the efforts described here are intended to assess the appropriateness of such a practice. Furthermore, the development and implementation of more complete high-fidelity human models may prove to be invaluable in capturing the complete physical behavior in injurious event simulations.

3 Methods

3.1 Geometric Models

3.1.1 Torso Model

The torso model is based on the National Library of Medicine's Visible Human Project male data set [26]. The model is constructed by segmenting 495 CT slices and one millimeter thick axially sliced cryosections of the Visible Human male into the soft tissues, organs, and bone comprising the torso. The model initiates at the base of the neck and terminates just superior to the pelvic region. Figure 1 depicts the segmentation process which consists of creating regions of interest for each distinct material from the CT slices and high resolution images of cryosections. The regions of interest for each material are then converted into ByteMaps.

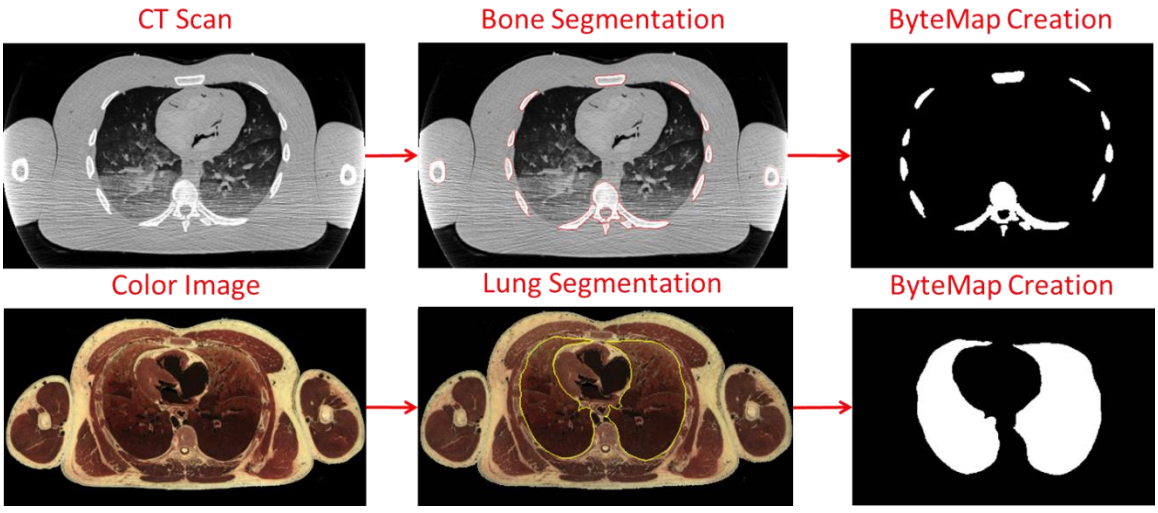

Figure 1: Segmentation technique. Top Row: Segmentation of bone material from CT scan, inferior to superior slice orientation – image right is body left. Bottom Row: Segmentation of lung material from high resolution color images of cryosections, superior to inferior orientation–image right is body right.

As seen in Figure 2, anatomically correct representations of 19 distinct materials including bone, cartilage, intervertebral discs, vasculature/blood, airways/air, lungs, liver, kidneys, spleen, heart, muscle, larynx, stomach, stomach contents, spinal cord, cerebrospinal fluid (CSF), thyroid, abdominal cavity contents, and skin/fat were created by utilizing this segmentation technique.

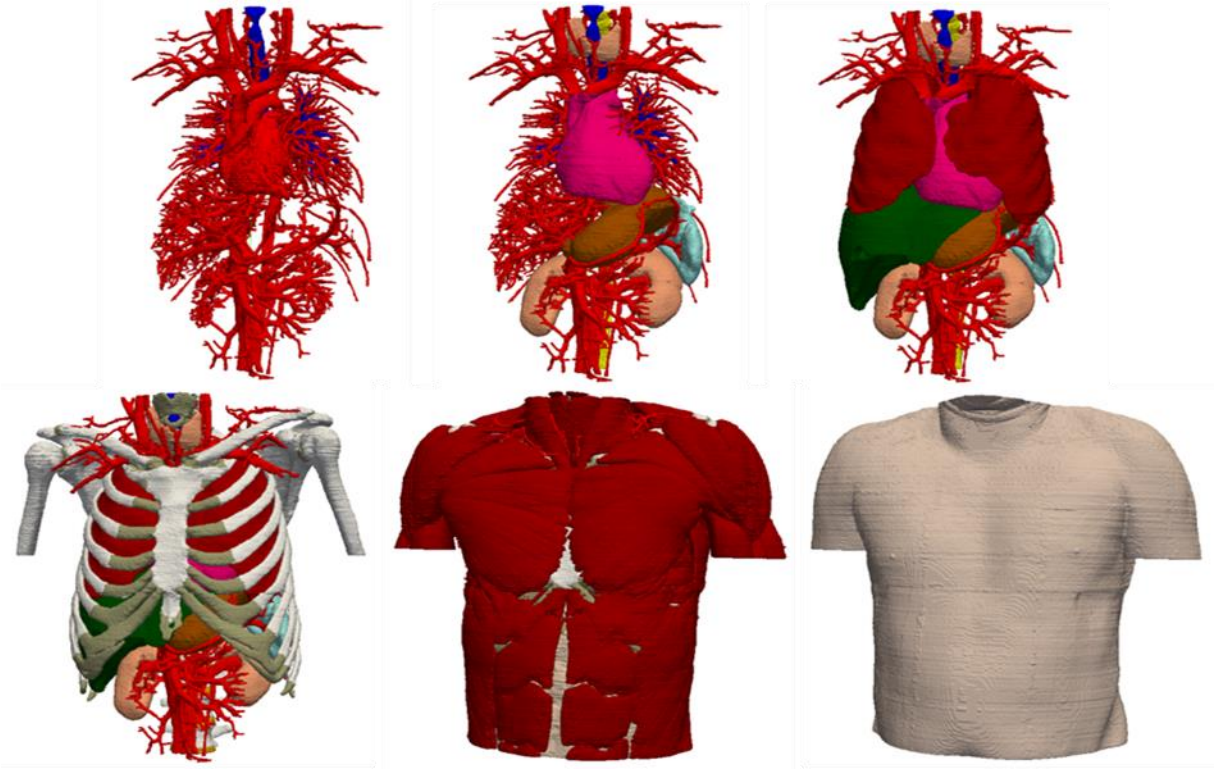

Figure 2: Evolution of Torso Model. Top Left: blood/vasculature and airways. Top Center: addition of heart, thyroid, spinal cord, CSF, spleen, kidneys, and stomach. Top Right: addition of lungs and liver. Bottom Left: addition of bone, cartilage, larynx and intervertebral discs. Bottom Center: addition of muscle and abdominal cavity contents. Bottom Right: addition of fat/skin.

The segmentation process maintains high anatomical fidelity with a spatial resolution of 1 millimeter. The torso model can be represented in both finite volume and finite element forms, consisting of roughly 42 million elements, for use with Eulerian, Lagrangian, or coupled Lagrangian-Eulerian codes. To create the finite element model, the ByteMap

files of each segmented constituent material are converted to a finite element mesh using local software developed specifically for this purpose [27].

3.1.2 Head-Neck Model

The torso model is a continuation of the previously completed Sandia Head-Neck (HN) model [6] shown in Figure 3. The Sandia Head-Neck and Sandia Torso models were created from the same Visible Human Project male data set [26] with the torso model initiating where the HN model terminates. Because of this relation, the HN and Torso models can be joined to create a complete Head-Neck-Torso model.

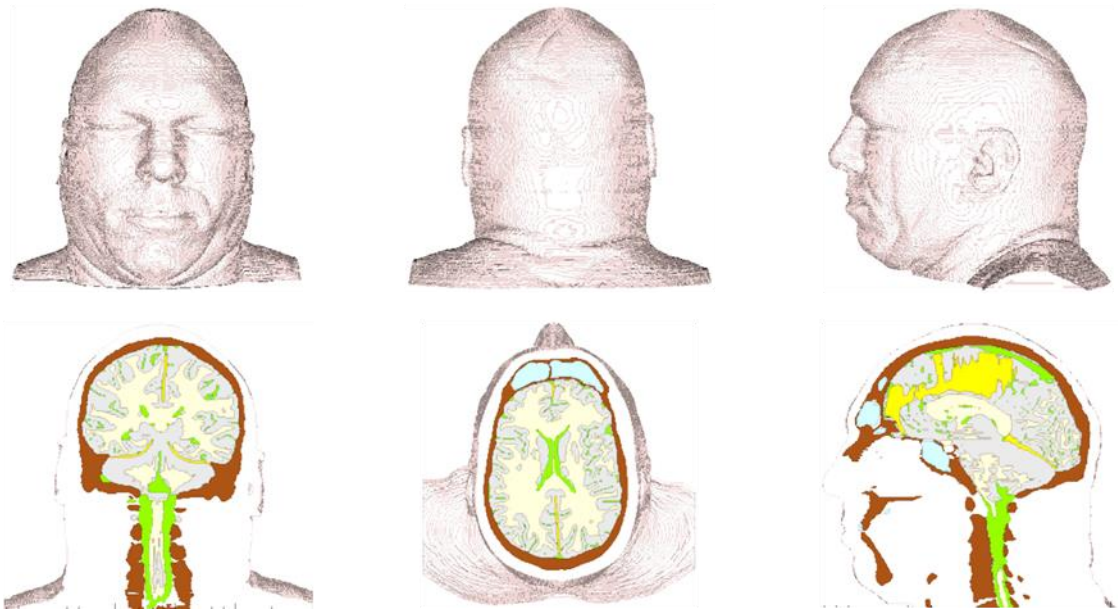

Figure 3: Sandia Head-Neck model.

3.1.3 Head-Neck-Torso Model

The Sandia Head-Neck-Torso model (HNT) is created by joining the torso model with the preexisting Sandia Head-Neck model (HN). In addition to containing the materials representing the constituents of the torso, the combined model also contains the cervical

vertebra, skull with mandible, white matter, gray matter, falx/tentorium membranes, cerebrospinal fluid (CSF), and air –filled sinus cavities. Figure 4 displays the composite HNT model in both an external and sectional view with the junction plane indicated by a red dashed line.

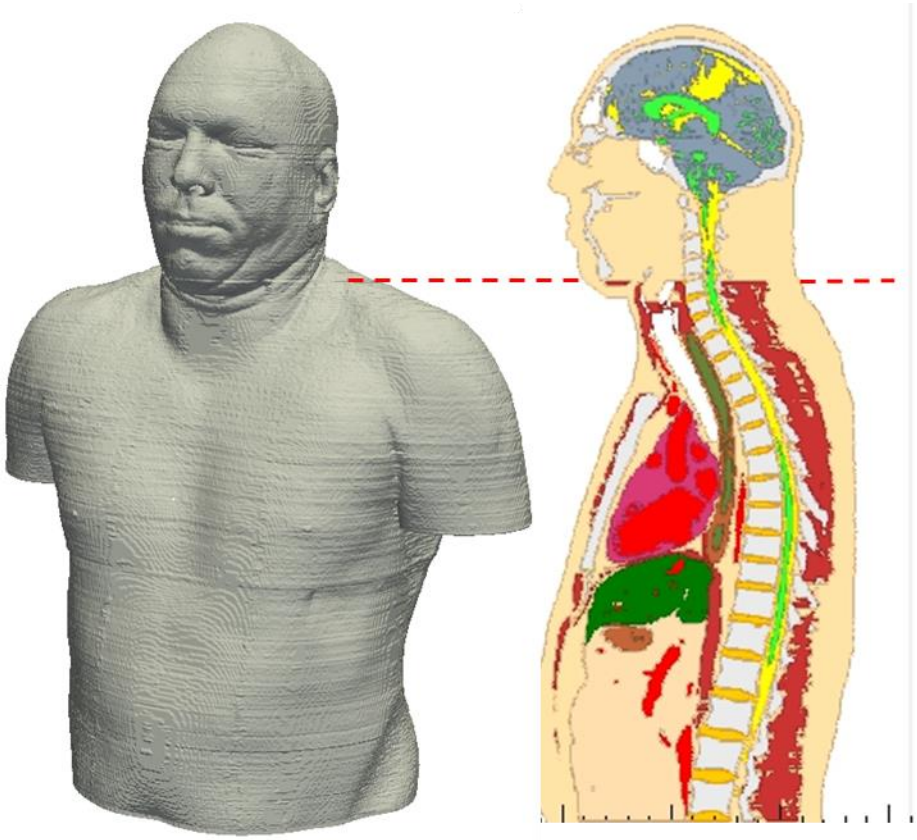

Figure 4: Merged Head Neck and Torso model prior to additional modifications to Head Neck model. Dotted line indicates junction plane between Head-Neck model and Torso model.

Both qualitative and quantitative approaches were taken to verify continuity at the junction plane between the HN and torso models. Figure 5 presents a pressure time-progression sequence of a 260 kilopascal (kPa) overpressure frontal blast exposure in three different sagittal plane cross-sections across the junction plane. A qualitative

verification of model continuity is made by visually assessing the pressure behavior in the materials across the junction plane.

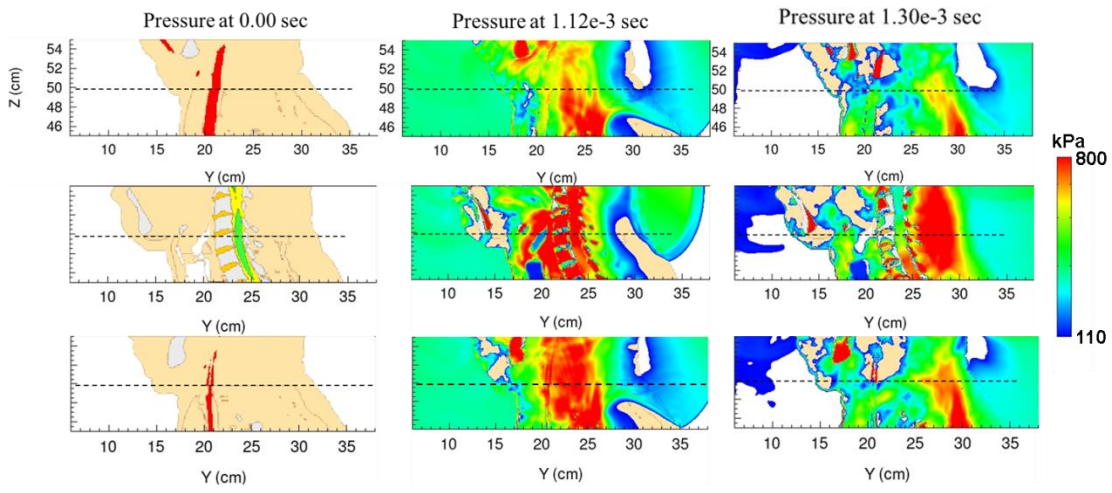

Figure 5: Pressure time-progression sequence of a 260kPa frontal blast. Each row of images depicts a different sagittal plane of the head-neck-torso junction with the pressure propagation through time to qualitatively verify model continuity over the head-neck to torso model junction.

Additionally, Lagrangian tracer points were placed in multiple vertical columns across the horizontal junction plane. Continuity was verified quantitatively by assessing the pressure, Lagrangian strain, and stress histories within each column of tracers for consistency. There were minimal deviations for any given history variable within any one column of tracers. The deviations that were identified are due to those specific Lagrangian tracers being located in computational cells comprised of multiple materials, also called mixed material cells, and/or due to temporal and spatial effects. For brevity, this data has been placed in Appendix A.

Modifications to the HN model were required to further ensure model continuity. These modifications consisted of the additional segmentation and inclusion of the intervertebral discs, musculature, airway, and vasculature, which were not previously included in the

HN model. The complete HNT model with the additional modifications can be seen in Figure 6.

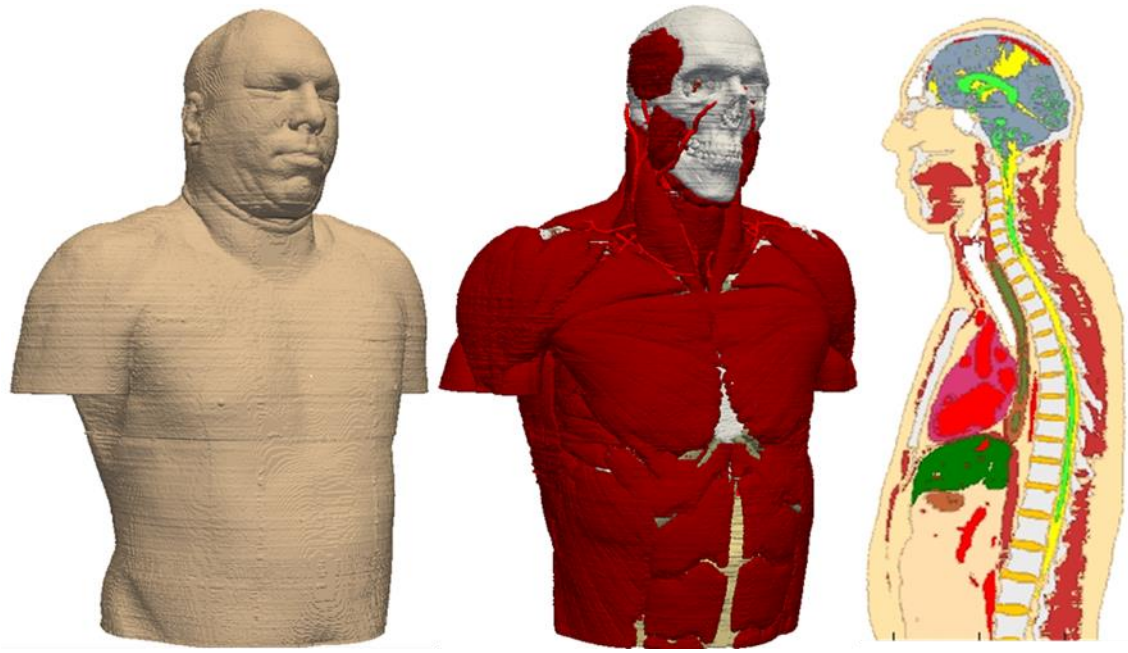

Figure 6: Merged Head-Neck-Torso model with updated head neck model including muscle, intervertebral discs, vasculature, and airway.

Furthermore, previous research employing the HN model by Taylor et al. [6] illustrated a deficiency in the thickness of the anterior table of the frontal sinuses. The thin bone was manually corrected to an average anterior table thickness of 4.0 mm [28] to prevent non-physical behavior as seen in late time results by Taylor et al. [6].

3.2 Equation-of-State and Constitutive Models

The dynamic mechanical response of each material comprising the human models is represented by a distinct equation-of-state and deviatoric constitutive model. These models incorporate relevant material properties reported in the scientific literature. An equation-of-state (EOS) describes the material's behavior as it undergoes volumetric

changes, which can be either compressive or dilatational. In general, an EOS is defined by the following relations:

$$P = \hat{P}(\rho, E) \tag{1}$$

and

$$T = \hat{T}(\rho, E) \tag{2}$$

where P is pressure, T is temperature, ρ is mass density, and E is internal energy. EOS models from the existing CTH library [29] have been utilized to represent the materials comprising the human models. More specifically, either a Mie-Gruneisen EOS [29] or a Tillotson-Brundage EOS [30] has been assigned to each material.

The Mie-Gruneisen (M-G) EOS describes the volumetric response of a material experiencing thermomechanical states within some proximity to the material's shock response as described by its shock Hugoniot curve. The shock Hugoniot curve is considered to be a material property and is described in depth within the LASL Shock Hugoniot Data book authored by Marsh [31]. The Mie-Gruneisen EOS works well for materials that are not expected to undergo phase transformations or significant dilatational strains. For dilatational states, the M-G EOS is linearly extrapolated to the user defined point of failure, i.e. fracture. Further details regarding the Mie-Gruneisen EOS and shock Hugoniot are described by Hertel and Kerley [29].

The Tillotson-Brundage (T-B) EOS [30] is a modified version of the Tillotson EOS [32], originally developed to capture vaporization from compression release for hypervelocity impacts of metals. Brundage [30] modified the Tillotson EOS by filling in the

thermodynamic gaps in $\rho - E$ state space, adding new tensile regions, and incorporating a fluid cavitation model. Brundage then fit the T-B EOS to represent the response of cerebrospinal fluid based on data reported in references [33–35] and to human blood using the data reported in references [36,37]. The contents of the stomach are also modeled using a T-B EOS for water.

To simulate blast loading to the human models, air must be included in the simulations. Air surrounds the models at ambient conditions, occupies the sinuses, the airways, and throughout the lungs, and transmits the blast waves. A non-linear, tabular equation-of state representation for a dry air mix of N_2 (78.09%), O_2 (21.95%), and Ar (0.96%), at a reference density of 1.218e-3 g/cc , specifically developed for shock wave simulations [29] has been employed for the simulations described here. The compression Adiabat, generated from this tabular EOS representation for air, can be seen in Figure 7.

If a material is not expected to undergo large dilatational strains and fluid cavitation, the Mie-Gruneisen EOS is assigned. If instead, the material is expected to undergo dilatational conditions potentially leading to fluid cavitation, the Tillotson-Brundage EOS is assigned.

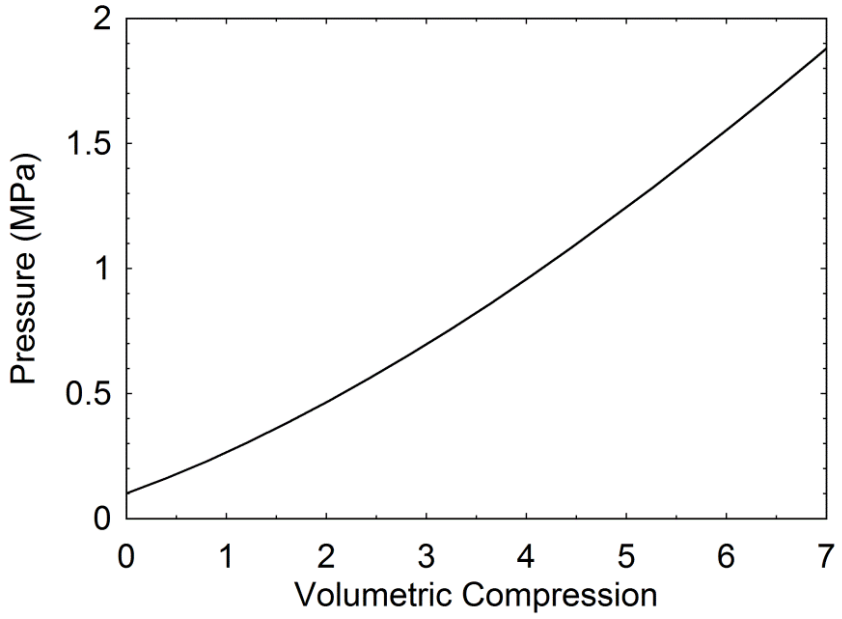

Figure 7: Compression Adiabat describing the volumetric response for dry air; calculated from the tabular EOS representation for this material. Volumetric compression is a dimensionless quantity.

The constitutive models describe the elastic, viscoelastic, or inelastic deviatoric response of the material when it is subjected to shear or distortional strains. In order to test the human modeling and simulation tools and begin to illustrate the value of such tools, many of the materials are represented by simplistic linear elastic, perfectly plastic constitutive models. Swanson hyperelastic models have been fit to the lung, heart, liver, kidney, spleen, and muscle tissues [7]; however, this model is not utilized in the current research described here as it has not undergone rigorous validation. The spinal cord, white matter of the brain, and gray matter of the brain are modeled using a viscoelastic material representation. The deviatoric response of these materials is represented by a 3-term Maxwell viscoelastic constitutive model. The time-dependent shear modulus of this material is of the form:

$$G(t) = G_\infty + (G_0 - G_\infty)e^{-\beta t} \tag{3}$$

where t denotes time, $G_0$is the short-term shear modulus, G_∞ is the long-term modulus, and β is the viscous decay constant for the material. These parameters were sourced from the paper by Zhang et al. [38] and are listed in Table 1.

The bone material is represented by a Mie-Gruneisen EOS and a linear elastic, perfectly-plastic deviatoric constitutive model with an accumulated plastic strain-to failure fracture model. The failure model introduces a damage variable,D, that is defined by:

$$D(x,t) = \int_0^t \frac{d\varepsilon^p}{\varepsilon_f^p} \tag{4}$$

where ε^p is the equivalent plastic strain, continuously updated at each time step, and $\varepsilon_f^p$is the critical value of equivalent plastic strain at fracture. $D = 0$ represents undamaged material, whereas failure is considered to have occurred when D reaches a value of 1. The damage variable, D, is calculated for each computational cell containing bone material at every time step, degrading both the plastic yield strength, Y, and fracture stress, σ_f, of the material.The plastic yield strength, Y, degrades as defined by:

$$Y(x,t) = Y_0[1 - D(x,t)] \tag{5}$$

and the fracture stress, σ_f, degrades as defined by:

$$\sigma_f(x,t) = \sigma_f^0[1 - D(x,t)] \tag{6}$$

where Y_0 denotes the undamaged value of yield stress and σ_f^0 is the undamaged value of fracture stress. The material properties of bone were sourced from Zhang et al. [38] and

Carter [39]. A list of material properties for the materials comprising the human models are presented in Table 2.

Table 1: Viscoelastic material parameters.

Material	Short-term Shear Modulus G_o (KPa)	Long-term Shear Modulus G_∞ (KPa)	Decay Constant β (sec^{-1})
Spinal Cord	41.0	7.8	40
White Matter	41.0	7.8	40
Gray Matter	34.0	6.4	40

Table 2: Physical properties of materials comprising the human models.

Material	Density (g/cc)	Bulk Modulus (MPa)	Shear Modulus (MPa)	Yield Stress (MPa)	$\sigma_{fracture}$ (MPa)	$\varepsilon_{fracture}$
Bone	1.21	4762	3279	95	77.5	0.016
Intervertebral Discs	1.0	8.33	1.79	--	77.5	--
Costal Cartilage	1.0	8.33	1.79	--	77.5	--
Larynx	1.0	8.33	1.79	--	77.5	--
Vasculature /Blood	1.05	T-B fit	--	--	--	--
Airways/Air	1.22e-3	See Figure 7	--	--	--	--
Lungs	0.7	150	0.033	--	10.0	--
Liver	1.06	280	0.190	--	10.0	--
Kidneys	1.1	276	46.65	--	10.0	--
Spleen	1.1	276	46.65	--	10.0	--
Heart	1.0	380	0.106	--	10.0	--
Muscle	1.2	34.8	5.88	--	10.0	--
Stomach	1.05	480	0.096	--	10.0	--
Stomach Contents	1.0	T-B water	--	--	--	--
Spinal Cord	1.04	T-B fit	Table 1	--	--	--
Cerebrospinal fluid	1.004	T-B fit	--	--	--	--
Abdominal Cavity Contents	1.2	34.8	5.88	--	10.0	--
Thyroid	1.2	34.8	5.88	--	10.0	--
Skin	1.2	34.8	5.88	--	10.0	--
Brain Membranes	1.133	105	5.97	--	10.0	--
Gray Matter	1.04	T-B fit	Table 1	--	--	--
White Matter	1.04	T-B fit	Table 1	--	--	--
Chest Armor Shell	1.44	2084	TI fit	--	--	--
Chest Armor Foam	0.136	4.44	3.33	--	77.5	--
9 mm FMJ Bullet	11.689	45826	8600	54	460	--

3.3 Simulations

Blast and non-penetrating projectile impact simulations were performed using the shock wave physics code CTH [40]. CTH is an Eulerian finite-volume computer simulation code that is capable of tracking 90+ materials simultaneously, simulating their interactions as they undergo blunt impact, blast loading, and penetration. This code adequately captures the fluid-solid interactions that occur between blast waves and the human models. CTH possesses an extensive array of constitutive models with which to represent bone, biological tissue, projectile materials, and both the ambient and pressurized air. For this specific application, a modified version of CTH was created to track wave physics variables that potentially correlate to tissue injury.

Ideally, the human models and simulation methodology would be validated against forensic wound data obtained from battlefield injuries due to blast and ballistic projectile impact. Since collection of this data is ongoing, the task of validation has yet to be completed. As such, the reader is cautioned that the results presented here are for illustrative purposes and, at this time, are not meant to provide quantitative assessments of wound dynamics or armor assessment. One exception here is the truncated head-neck model which has undergone validation as described in the paper by Taylor et al. [6].

3.3.1 Projectile Impact: Torso

Notional torso armor was created to demonstrate the capability of relative merit assessments between armor designs. The chest armor model is composed of a 1.5 centimeter thick composite shell. This armor model is assessed in two different configurations. One configuration consists of the armor shell backed by foam padding,

the other configuration is absent of the foam padding. The projectile used in these simulations is a mock representation of a 9-by-19 millimeter full metal jacket (FMJ) bullet with an impact velocity of 370 meters-per-second. This representation captures the geometry and mass of a 9 millimeter FMJ bullet while simplifying its composition to that of a single material projectile. The composite shell of the chest armor was represented by a Mie-Gruneisen Equation-of-State (EOS) and a Transversely Isotropic (TI) constitutive model [41] describing its deviatoric response. The TI model parameters for this material are proprietary and, as such, are not listed here. Material properties for the chest armor shell, foam backing, and the 9 millimeter FMJ bullet are listed in Table 2.

3.3.2 Blast: Torso

Frontal blast simulations were conducted both to illustrate the capability to conduct relative merit assessments between armor designs as well as to compare the use of the full Head-Neck-Torso model with the truncated Torso and Head-Neck models. The notional chest armor utilized in the relative armor merit assessment blast simulations is composed similarly to the chest armor in the projectile impact simulations, with the only difference being the thickness of the armor's composite shell which is 1.0 centimeters in the blast simulations. In each of these blast simulations, models were subjected to an identical pressure pulse of 260 kPa overpressure with a pulse width of 2 milliseconds. This specific pressure pulse is chosen to simulate the conditions that would be generated from a spherical 2.3 kilogram charge of Composition-4 located at a distance of 2.3 meters from the torso model.

To reduce computational expense, the blast wave produced from the detonating explosive is approximated without explicitly including the detonation event in the simulation. The torso model is positioned within a space containing ambient air. The blast wave is produced by introducing a slab of energized air, located approximately 36 centimeters from the torso model at time zero. The back face of the air slab is fixed by a rigid boundary, whereas the boundary at the front face of the slab, closest to the torso, is removed for times greater than zero. When the boundary at the front face of the slab is removed, the air mass flows from the energized slab, creating a pressure pulse that propagates through the surrounding air toward the torso model. The amplitude and pulse width of the blast wave is determined by setting the energized air slab to predefined conditions of energy, pressure, and slab thickness. When the pressure pulse reaches the torso the amplitude has degraded to a specified magnitude, in this case 260 kilopascals overpressure, and displays a blast pulse similar to the classical Friedlander waveform [42]. The simulated blast wave is depicted in Figure 8.

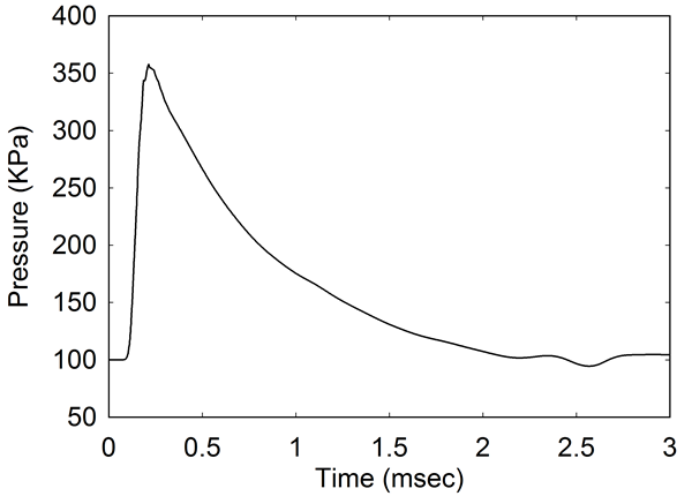

Figure 8: Simulated 260kPa (gauge) blast pulse.

The torso model is placed with both upper and lower truncated model boundaries located against the upper and lower boundaries of the computational space. This allows for the pressure pulse to travel around the torso model without allowing for the pressure pulse to travel over or under the truncated boundaries of the torso model.

3.3.3 Blast: Head-Neck-Torso

To compare the use of the truncated torso and head-neck models to the full head-neck-torso model, an identical blast simulation was conducted with the head-neck-torso model. This simulation utilizes the same blast parameters as described for the torso model but with the head-neck-torso model in place of the torso model. The head-neck-torso model is positioned with the base of the model placed against the lower boundary of the computational space. This allows for the pressure pulse to travel around and over the head-neck-torso model without allowing for the pressure pulse to travel under the truncated boundary at the inferior end of the torso.

3.3.4 Blast: Head-Neck

The same 260 kPa overpressure blast simulation was conducted with the use of the truncated head-neck model to compare against the full head-neck-torso model. This simulation utilizes the same blast parameters as described for the torso and head-neck-torso models with the head-neck model in place of the head-neck-torso model. The truncated boundary of the head-neck model, located at the inferior end of the neck, is placed against the lower boundary of the computational space. This allows for the pressure pulse to travel around and over the head-neck model without allowing for the pressure pulse to travel under the truncated boundary at the neck of the model.

4 Results

The simulations results discussed here are described by the output variables of pressure and von Mises stress, either qualitatively, i.e. visually, or quantitatively, e.g. with time history plots. The decision to use these two output variables was based on the intent of these investigations. That is to say, pressure and von Mises stress were chosen as the most convenient scalar variables with which to describe the overall dilatational and deviatoric responses across the various model configurations. The intent of these simulations was to understand the variation between the differing models and model configurations and not necessarily to investigate injury itself. In order to investigate injury or conduct relative armor merit assessments in the future, there must first be an understanding as to which model is the most appropriate to utilize for a given injury scenario.

The data presented here has been filtered to assist in viewing significant trends in the data without obscurity due to the noise caused by high frequency sampling during the simulation. The pressure history results in sections 4.1, 4.2, and 4.3 were filtered using a low-pass 4 kHz filter. The pressure history results in section 4.4 were filtered using a smoothing algorithm within the plotting software DPlot, which smooths the data over a user defined window of 20 data points [43].

Furthermore, the results described in sections 4.1, 4.2, and 4.3 have been presented in previous publications by Cooper et al.[8] and Taylor et al. [7].

4.1 Projectile Impact: Torso

This section demonstrates the value of the Sandia torso model in analyzing behind-armor blunt trauma as a result of a ballistic projectile striking protective chest armor. Specifically, a comparison is made between prototype armor backed with foam padding, and the same prototype armor without padding. This allows for a relative armor assessment between models. For this demonstration, resulting pressures and von Mises stresses are compared at specific locations in life-critical organs between the simulations conducted with the use of notional chest armor with and without padding. It is of no value to this study to consider the unprotected case since the simulations have shown that a 9 millimeter projectile with a 370 meter-per-second velocity penetrates the torso, piercing the heart, likely causing serious, if not fatal, injury.

Figure 9 and Figure 10 display time-sequenced pressure profiles that result from the 9 millimeter FMJ round striking the notional chest armor with and without foam pad backing the armor shell, respectively.

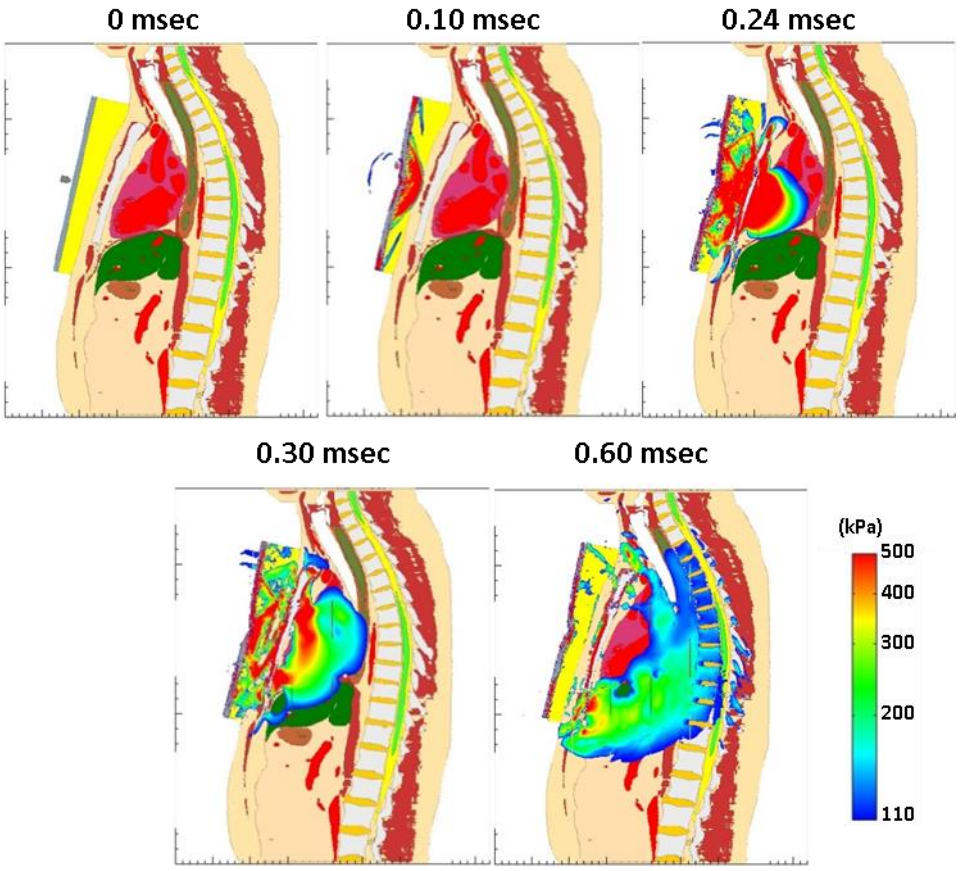

Figure 9: Pressure time-progression sequence of a 9mm ballistic projectile impact to the torso protected by chest armor backed with foam padding.

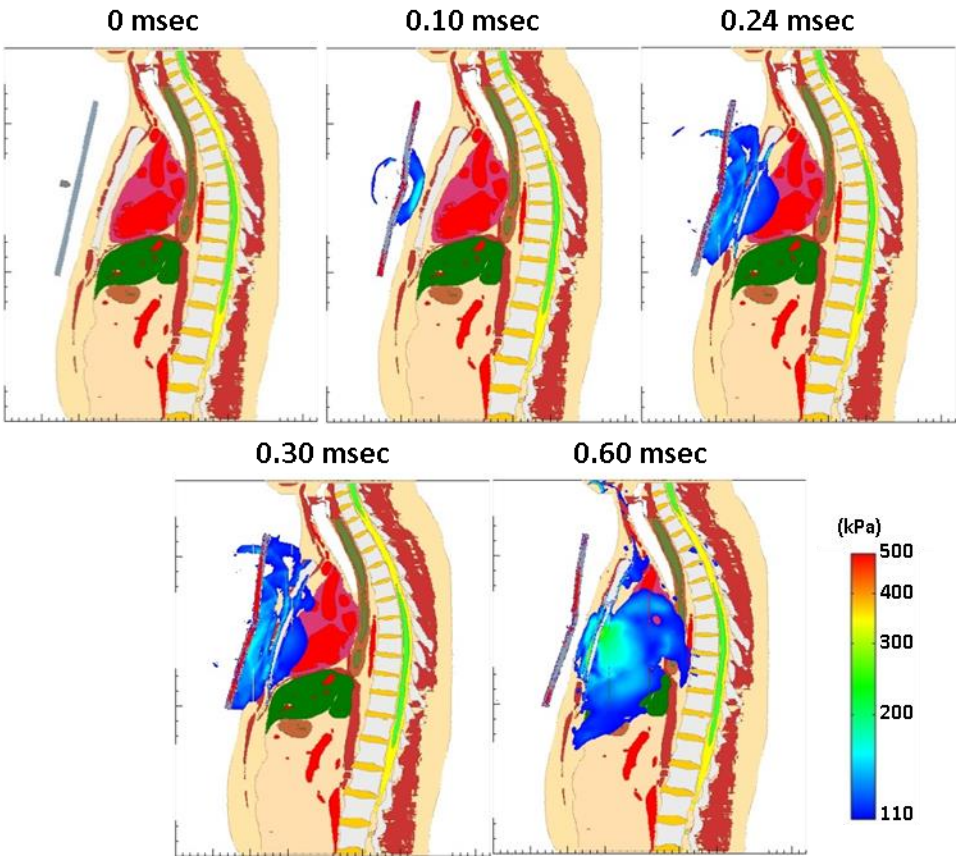

Figure 10: Pressure time-progression sequence of a 9 mm ballistic projectile impact to the torso protected by offset chest armor without foam padding.

A comparison of the pressure profiles in Figure 9 and Figure 10 demonstrates the protective advantage of armor that is separated by padding of low mechanical impedance. In this case, the chest armor backed by foam padding of realistic impedance (Figure 9) is compared with armor backed by padding possessing asymptotically small impedance, i.e. that of air (Figure 10). The presence of the foam padding permits transmission of the compressive and shear waves, formed in the armor as a result of the impact, directly into the torso at magnitudes and speeds higher than what would be possible in the absence of said padding.

These observations are corroborated by the pressure and von Mises stress histories, depicted in Figure 12 through Figure 15 , at Lagrangian tracer locations in the heart, right lung, left lung, and liver, respectively (see Figure 11). The most apparent difference between the two armor configurations can be seen in the pressure history plots for the heart and liver, Figure 12 and Figure 15, respectively. In these instances, the pressure loads to the heart and liver are all but eliminated in the armor system possessing no padding. The pressure histories in Figure 13 and Figure 14 for the lungs illustrate significant pressure reduction in the case of armor without padding; however, since the armor shell touches the torso at the lateral edges, a pressure pulse is transmitted into the torso and lungs which underlie the contact edges. The von Mises stress plots associated with the same Lagrangian tracer locations, depicted in Figure 12 and Figure 15, are consistent with the trends suggested by the pressure histories. The armor backed with padding permits significantly higher shear stresses to transfer into both the heart and liver than the armor without padding. The von Mises stress seen in both of the lungs show far less dependence on the existence of the foam padding. Once again, this is likely because the lateral edges of the armor shell are in contact with the torso, thereby permitting shear wave transmission into the torso and lungs which underlie the contact edges. This observation suggests that if the contact between the armor and torso is eliminated altogether, optimal protection from this armor may be realized.

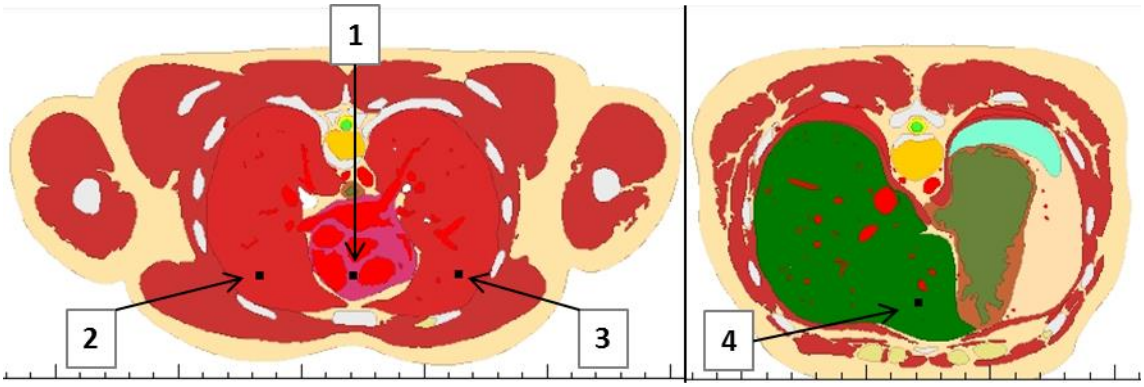

Figure 11: Lagrangian tracer point locations within the torso. (1) Heart, (2) Right Lung, (3) Left Lung, (4) Liver.

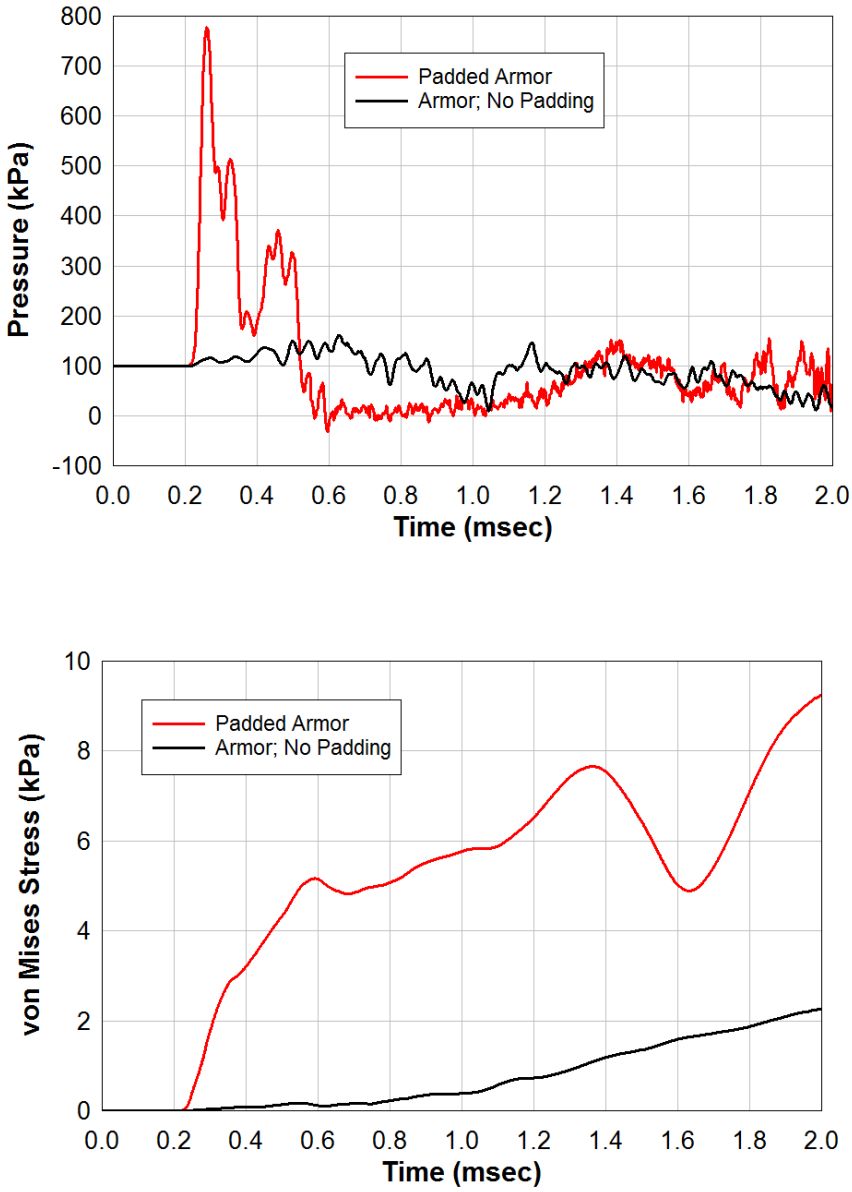

Figure 12: Heart pressure (top) and von Mises Stress (bottom) histories with the comparison between torso protected with chest armor backed by foam padding versus armor without padding.

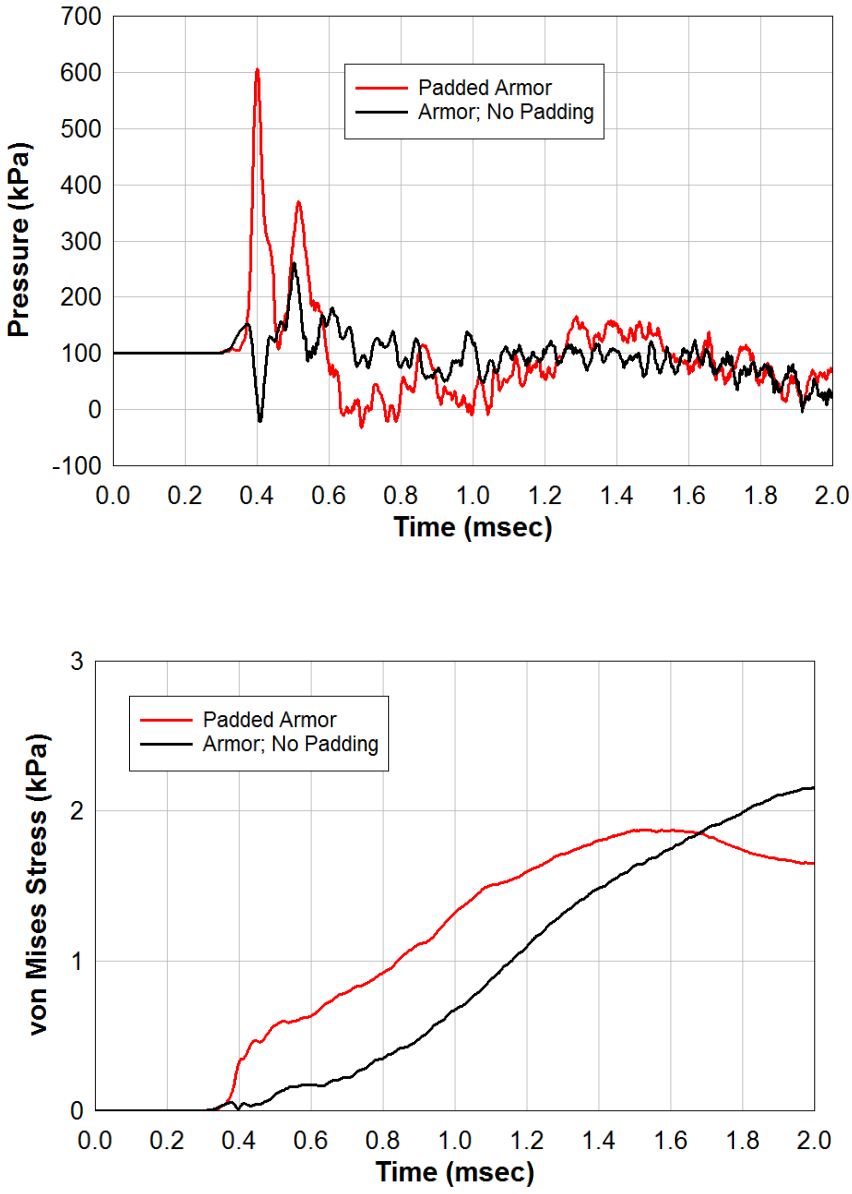

Figure 13: Right lung pressure (top) and von Mises Stress (bottom) histories with the comparison between torso protected with chest armor backed by foam padding versus armor without padding.

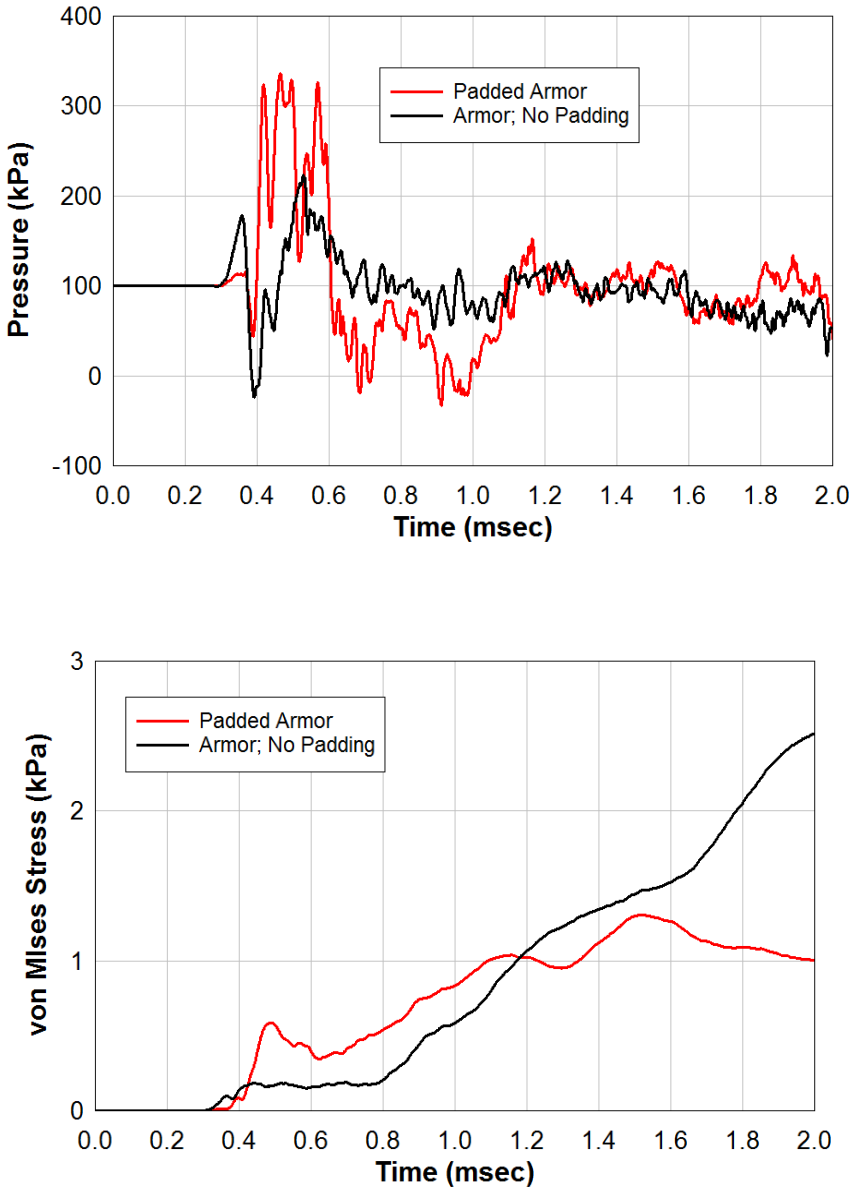

Figure 14: Left lung pressure (top) and von Mises Stress (bottom) histories with the comparison between torso protected with chest armor backed by foam padding versus armor without padding.

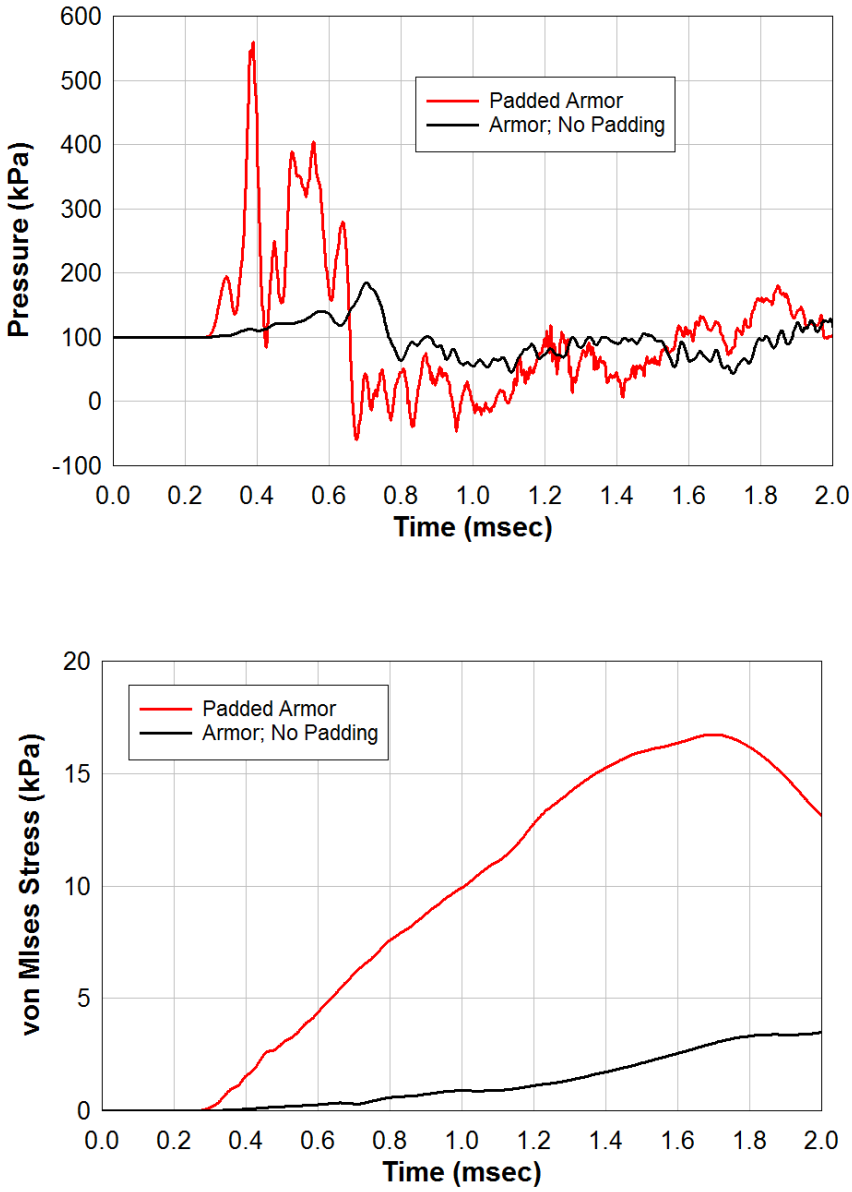

Figure 15: Liver pressure (top) and von Mises Stress (bottom) histories with the comparison between torso protected with chest armor backed by foam padding versus armor without padding.

4.2 Blast: Armored vs Unprotected Torso

This section summarizes the results of the protected and unprotected torso when exposed to a 260 kPa overpressure frontal blast. In previous chest armor assessment analysis, it has been found that mitigation of the transmitted pressure wave as it propagates through the chest armor depends highly on the existence of foam padding and its mechanical impedance. To examine this phenomenon further, blast simulations of the torso protected by chest armor both with and without padding, as well as a simulation of the torso without any protection have been conducted. The time progression pressure wave sequence of the unprotected case, armor backed by foam padding case, and armor without padding case can be seen in Figure 16, Figure 17, and Figure 18, respectively.

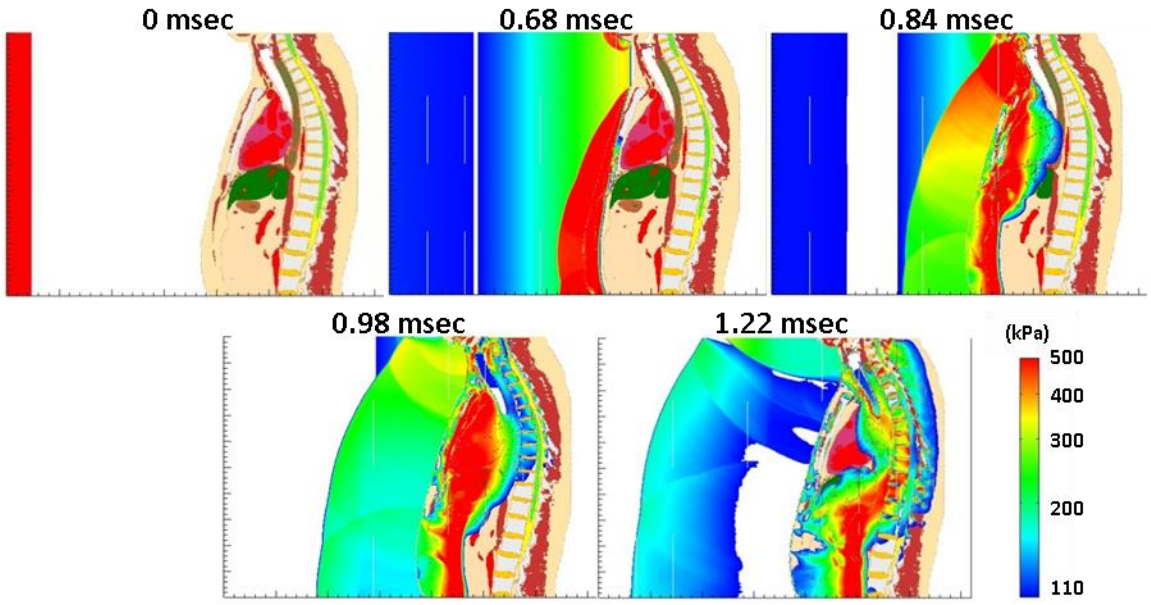

Figure 16: Pressure time-progression sequence of a 260kPa frontal blast exposure to the unprotected torso.

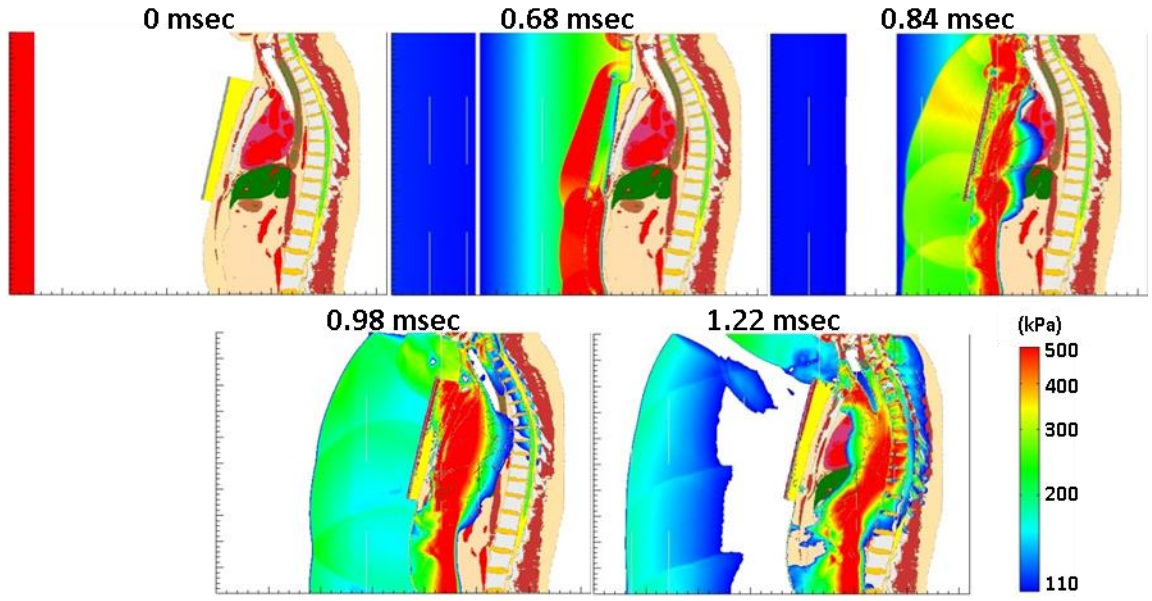

Figure 17: Pressure time-progression sequence of a 260kPa frontal blast exposure to the torso protected by armor backed with padding.

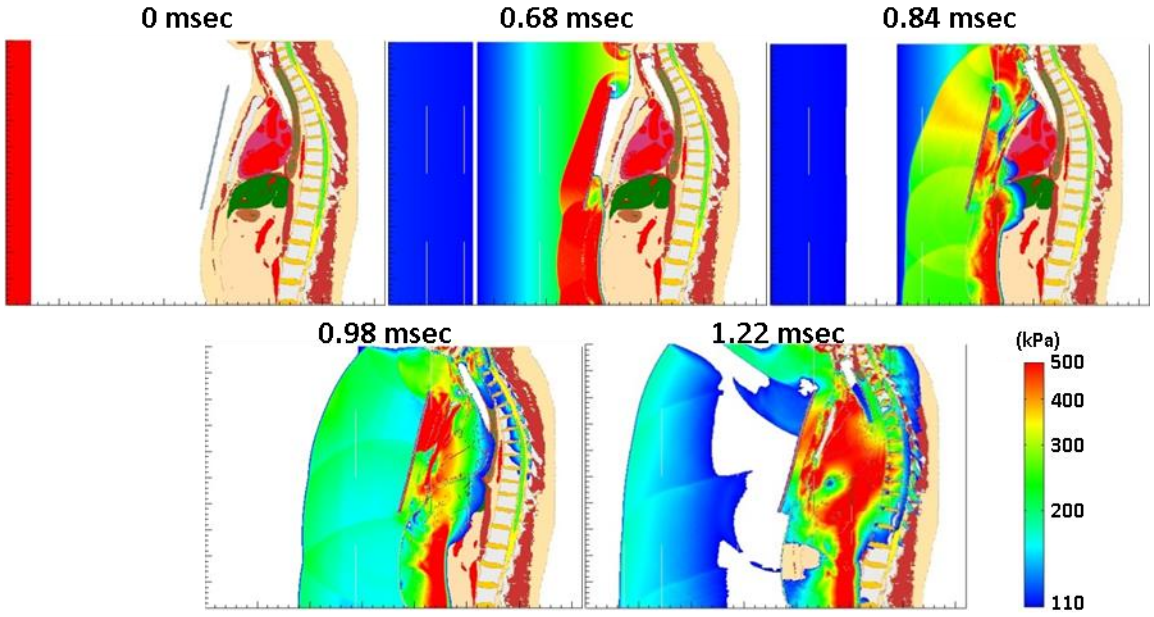

Figure 18: Pressure time-progression sequence of a 260kPa frontal blast exposure to the torso protected by offset armor without padding.

Comparing the progression of the pressure wave as it transits the torso, it can be seen that the armor without padding delays the advance of the wave into the torso. The torso is

subjected to a delayed pressure pulse formed once the air between the armor shell and torso is pressurized by the blast wave as it enters the air gaps at superior and inferior edges of the plate.

Figure 19 through Figure 22 depict the pressure and von Mises stress history plots of the Lagrangian tracer points placed within the heart, right lung, left lung and liver. These plots illustrate the pressure and von Mises stress at those points throughout the duration of the simulations. It should be noted that the addition of armor creates various changes in the pressures seen within the various organs. As seen in Figure 19 and Figure 22, with the addition of armor, both with or without padding, an increase in peak pressures within the heart and liver is seen in comparison to the unprotected case. However, the increase in peak pressure within the heart and liver is accompanied by a decrease in loading rate. The increase in peak pressure due to the presence of armor is not seen in the lungs (see Figure 20 and Figure 21). Interestingly, the armor without padding reduces the peak pressure magnitudes in the lungs. However, there is an extension in the pressure pulse width in the lungs for the armor cases both with and without padding in comparison to the unprotected case.

For all organs of interest, the unprotected case displays the minimal amount of increase in von Mises stress relative to both the case with armor backed by foam padding and the case with armor without padding. Most likely this is a result of the fact that the armor materials (i.e. the hard shell and foam padding) possess nontrivial shear strengths that permit the formation of shear waves in the armor itself during blast loading that are transmitted into the torso by means of direct contact through the padding or lateral edges of the armor shell against the torso. The greatest von Mises stress levels occur for the

case of the armor protection backed with padding. The shear waves formed in the armor and transmitted through the padding introduce shear loads in the torso significantly higher than what is experienced during the blast loading case of the unprotected torso. When the foam padding is absent, the von Mises stress levels are less than what is seen when the foam padding is present, but still greater than the unprotected case in the lungs. Once again, this is likely because of the contact of the lateral edges of the armor shell with the torso allowing for shear wave transmission into the torso and underlying lungs.

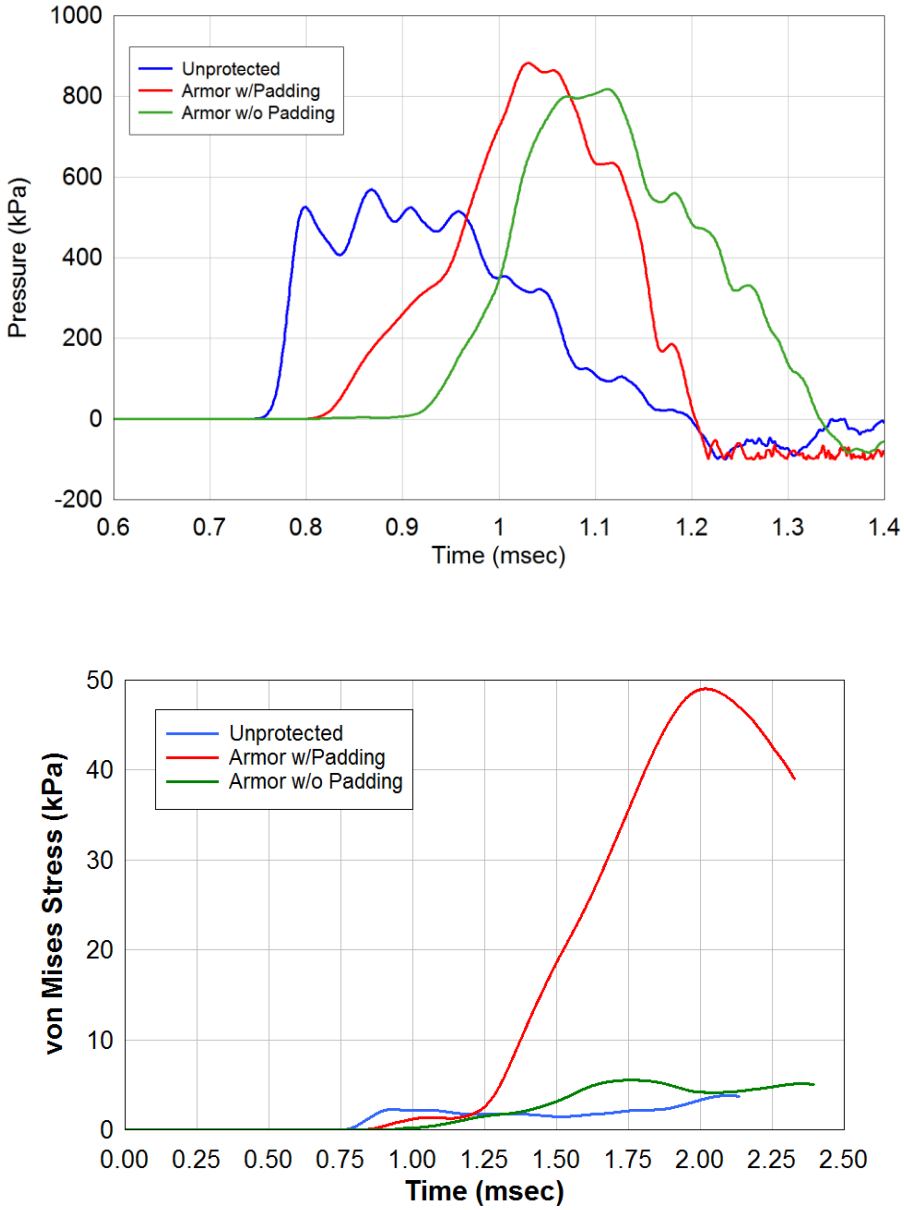

Figure 19: Heart pressure (top) and von Mises Stress (bottom) histories with the comparison between unprotected torso, torso protected with chest armor backed by foam padding, and torso protected with offset chest armor without padding.

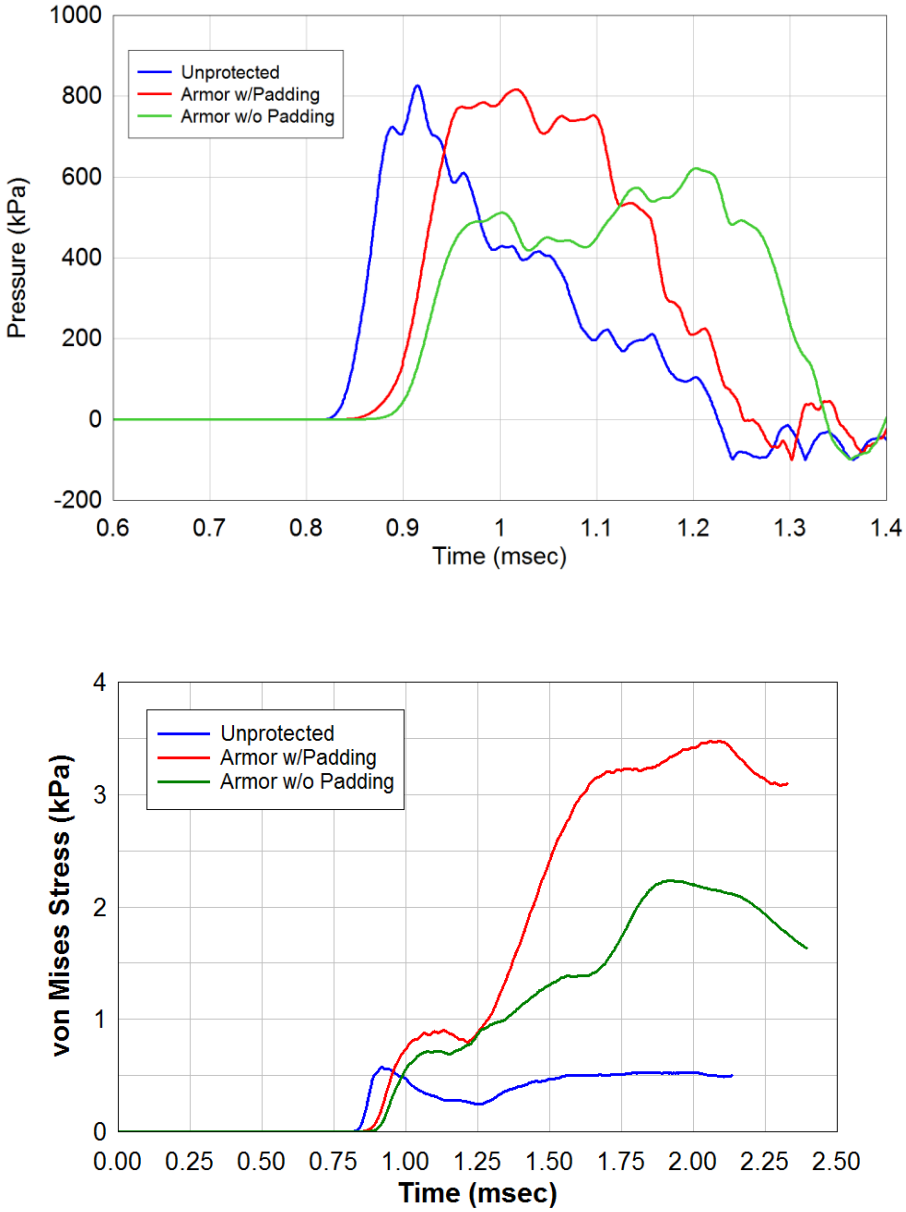

Figure 20: Right lung pressure (top) and von Mises Stress (bottom) histories with the comparison between unprotected torso, torso protected with chest armor backed by foam padding, and torso protected with offset chest armor without padding.

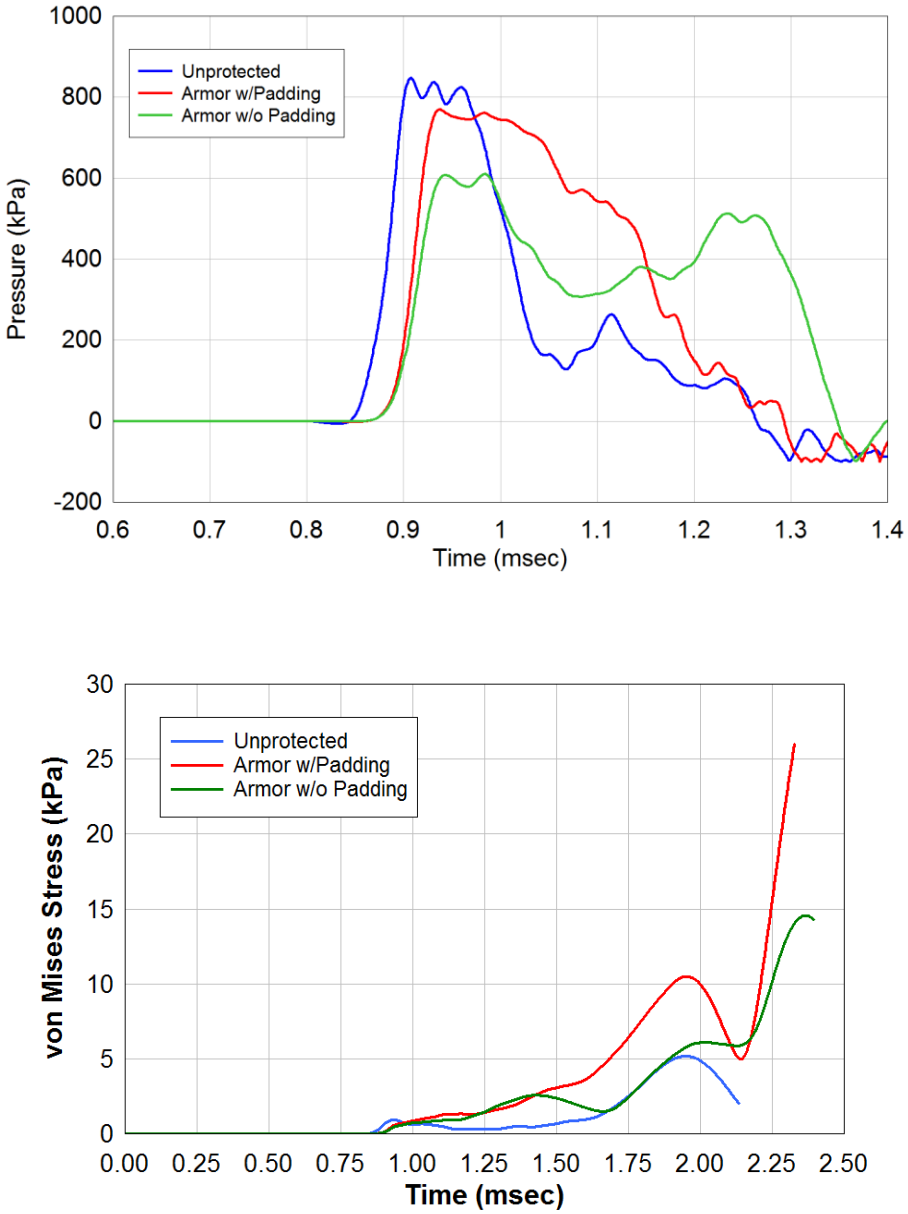

Figure 21: Left lung pressure (top) and von Mises Stress (bottom) histories with the comparison between unprotected torso, torso protected with chest armor backed by foam padding, and torso protected with offset chest armor without padding.

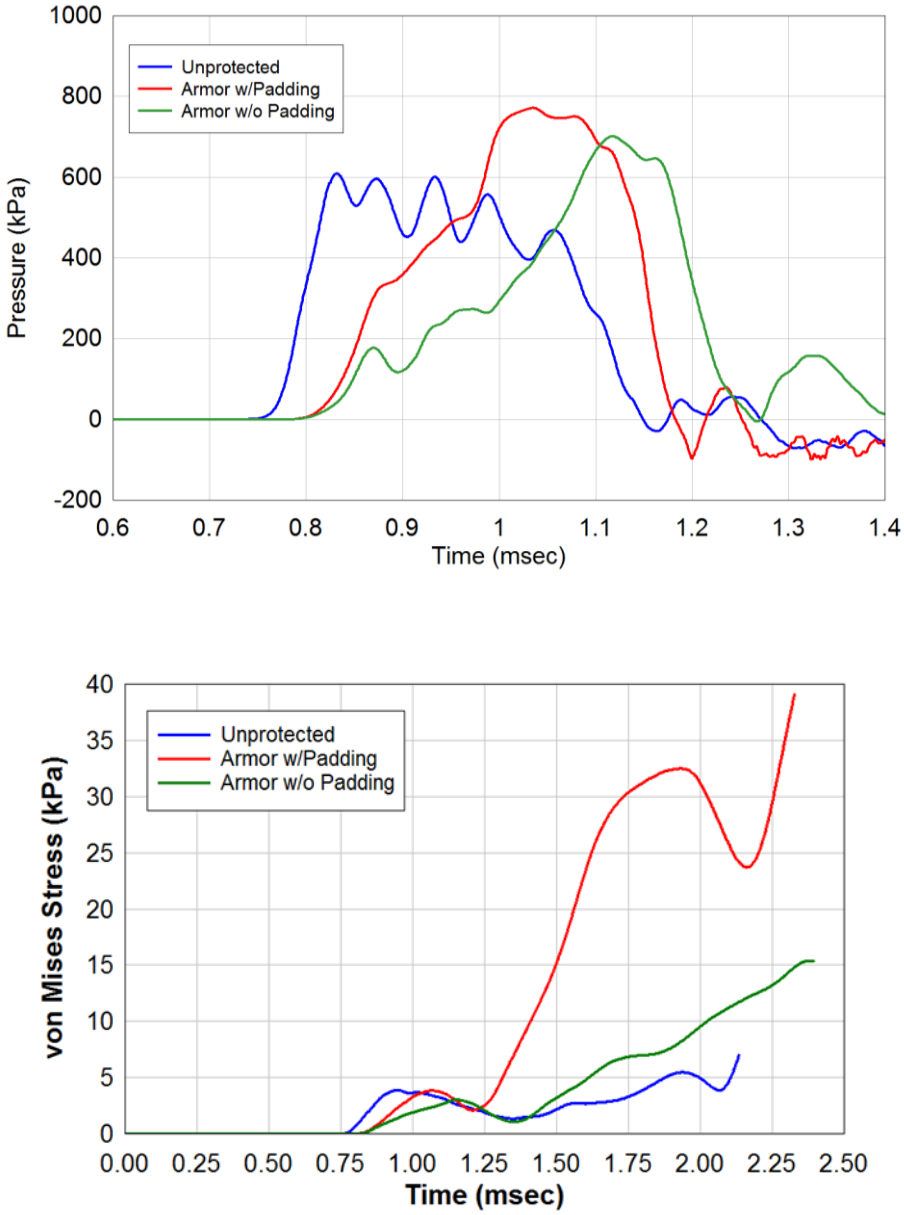

Figure 22: Liver pressure (top) and von Mises Stress (bottom) histories with the comparison between unprotected torso, torso protected with chest armor backed by foam padding, and torso protected with offset chest armor without padding.

4.3 Blast: Head-Neck-Torso vs Torso

In this section, results are presented for the unprotected head-neck-torso (HNT) model exposed to the same 260 kPa overpressure frontal blast conditions experienced by the unprotected torso model in section 4.2. Although it would appear to be beneficial to use a more complete human model to investigate wound injury and armor protection for the torso region, the computational expense in employing a complete model can be prohibitive in both computational execution time and data storage requirements. This same consideration can also be made when simulating injuries to the head using the truncated head-neck model. The intent in this instance is to assess whether simulations of wound injury to the torso can be conducted with a truncated human model of the torso or whether a more complete human model, such as the HNT model employed here, is required.

Figure 23 is an image sequence depicting the progression of the blast as it interacts with the HNT model. As with the torso model simulation depicted in Figure 16, the blast wave creates a transmitted wave that propagates through the HNT model, inducing internal wave reflections and transmissions that are influenced by the impedance differences between the different tissue types comprising the model.

Figure 24 through Figure 27 present the pressure and von Mises stress histories for the heart, right lung, left lung, and liver predicted by the simulation utilizing the HNT model in comparison to the simulation utilizing the torso model alone. It can be seen that both the pressure and von Mises stress predictions are almost identical between the simulation utilizing the truncated torso model and the simulation utilizing the HNT model. The only major distinction between the two predictions is the extent of simulated time to which the

torso model simulation was able to achieve before spurious pressure waves caused a non-recoverable error in the simulation. These spurious waves are the result of the artificial conditions imposed on the upper boundary of the torso model to approximate the presence of an otherwise absent neck and head. Without this boundary condition, the blast-induced intrathoracic pressure waves would cause the contents of the torso to eject through the upper boundary of the truncated torso. The spurious pressure waves cause the non-recoverable error prior to causing any noticeable inaccuracies in the results at the Lagrangian tracer points of interest. However, without the ability to execute the blast simulation out past 3 milliseconds of simulation time, the torso model simulations are incomplete as they miss the late-time von Mises stress increases and oscillations.

This result suggests a limitation in the utilization of the torso model alone that may reduce its usefulness unless problems with the imposed boundary conditions can be resolved. Further development of the torso model and the associated boundary conditions may potentially overcome this specific limitation.

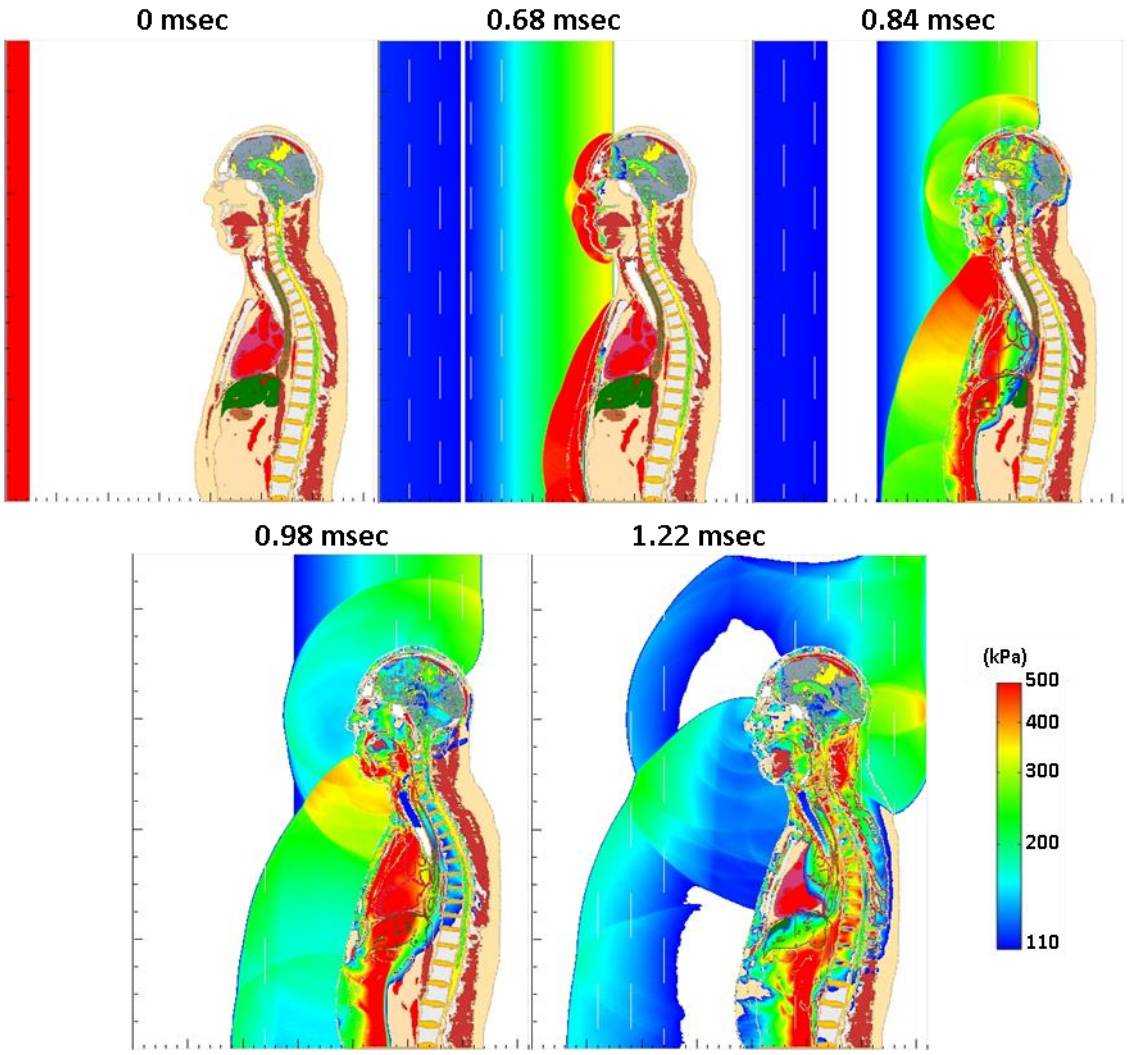

Figure 23: Pressure time-progression sequence of a 260kPa frontal blast exposure to the unprotected head-neck-torso.

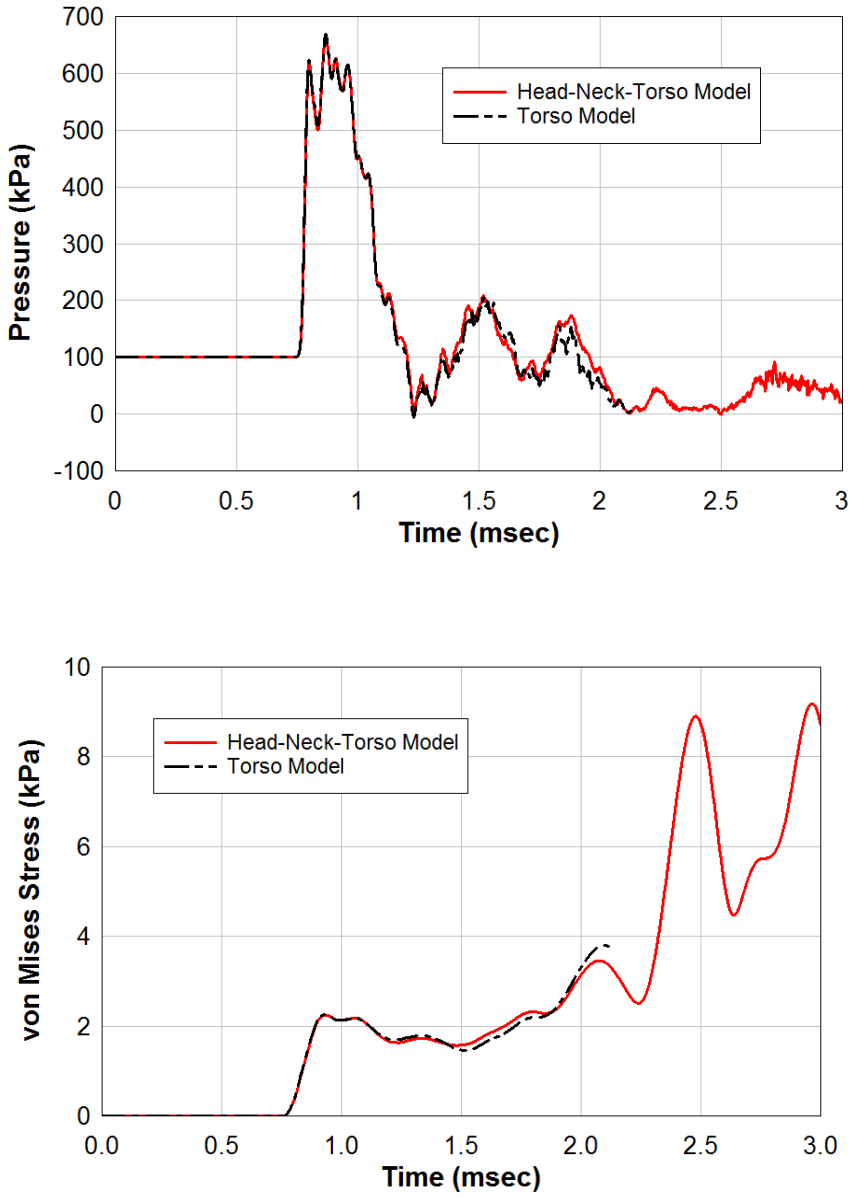

Figure 24: Heart pressure (top) and von Mises Stress (bottom) histories with the comparison between simulation predictions using the full head-neck-torso model versus the torso model.

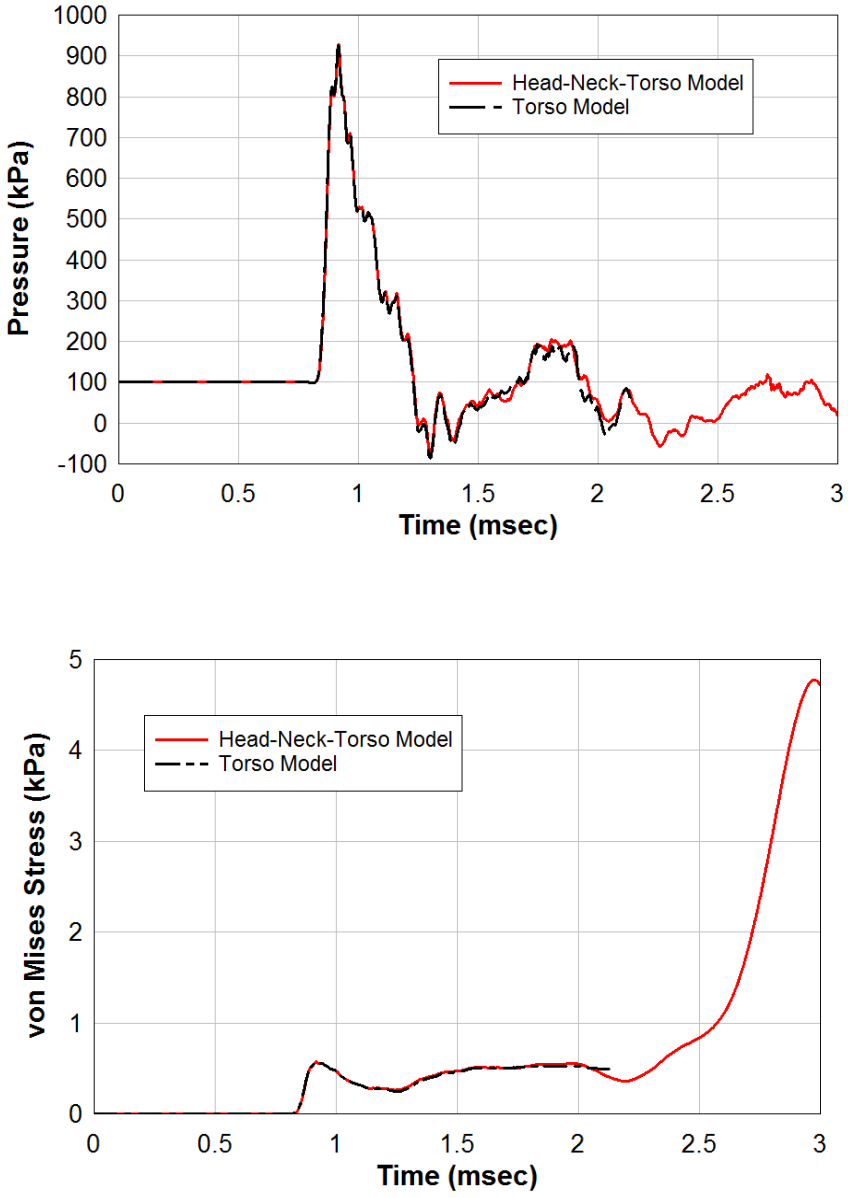

Figure 25: Right lung pressure (top) and von Mises Stress (bottom) histories with the comparison between simulation predictions using the full head-neck-torso model versus the torso model.

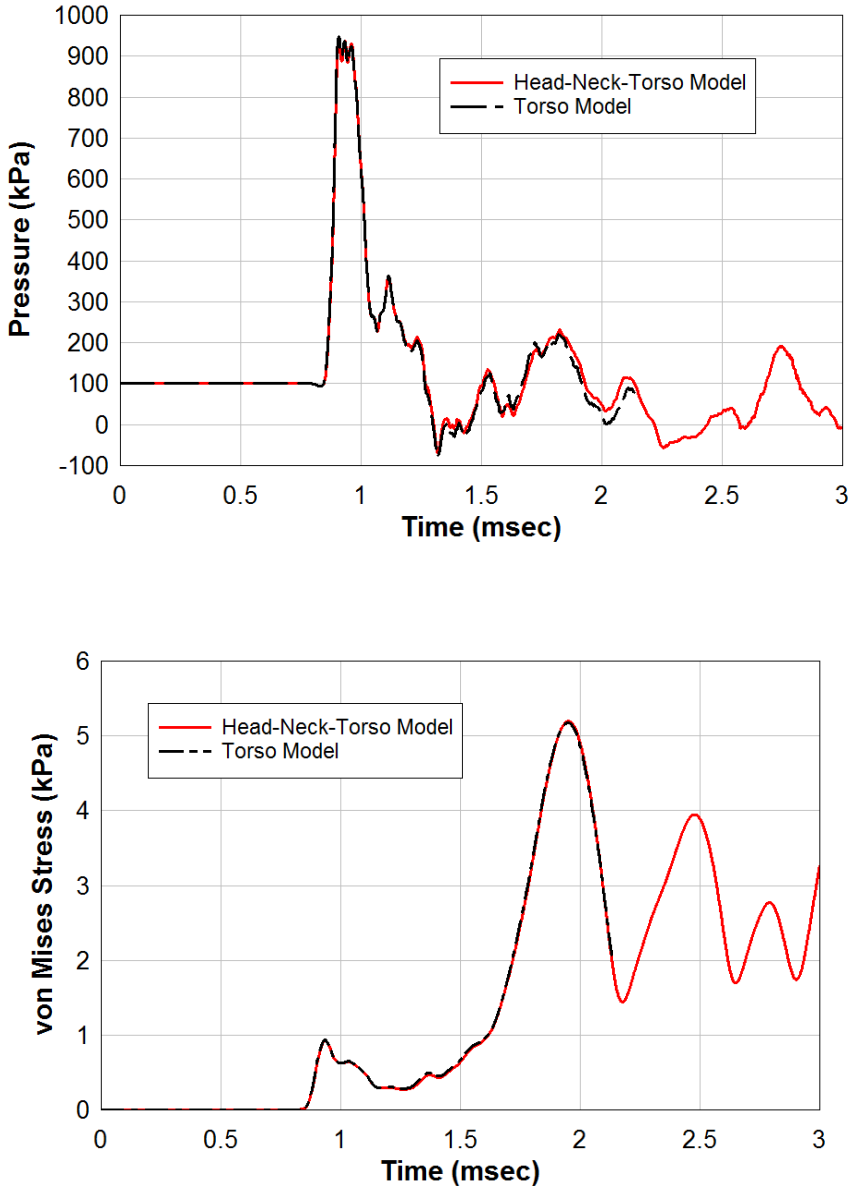

Figure 26: Left lung pressure (top) and von Mises Stress (bottom) histories with the comparison between simulation predictions using the full head-neck-torso model versus the torso model.

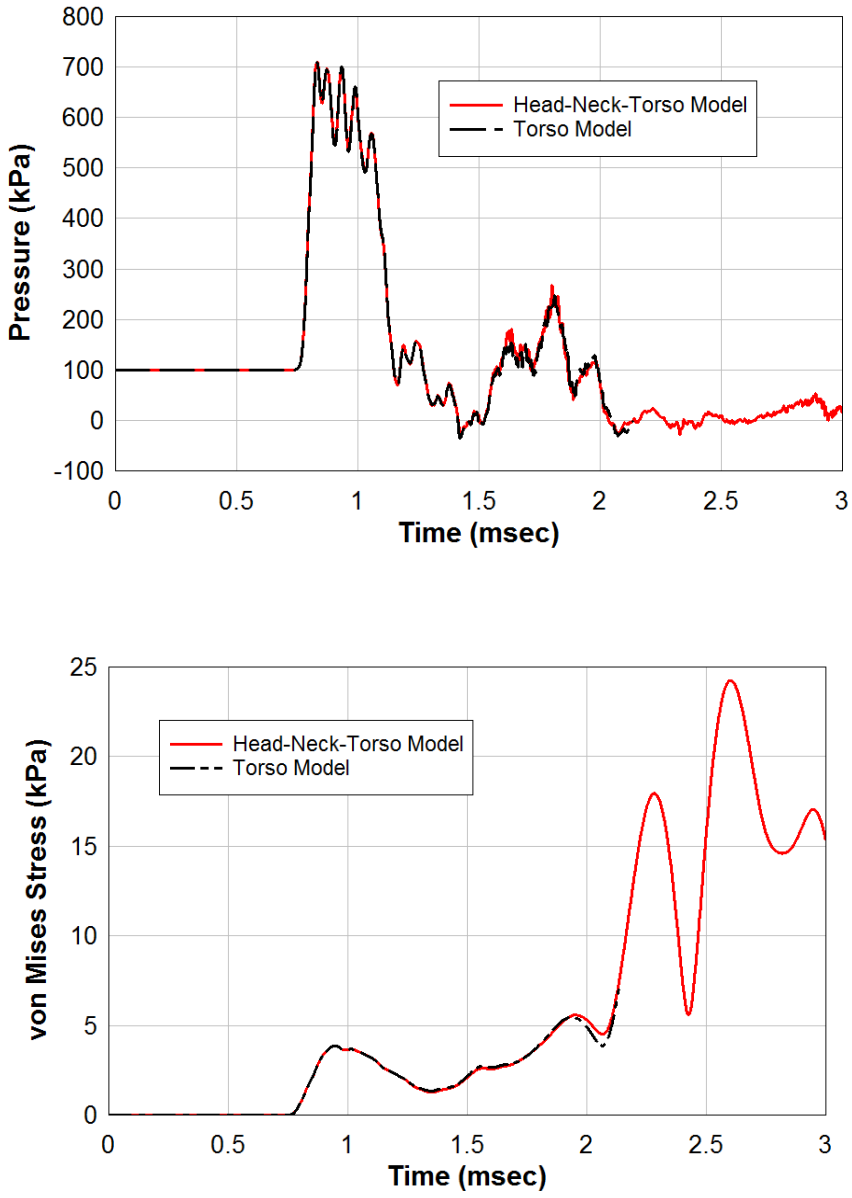

Figure 27: Liver pressure (top) and von Mises Stress (bottom) histories with the comparison between simulation predictions using the full head-neck-torso model versus the torso model.

4.4 Blast: Head-Neck-Torso vs Head-Neck

Similar to the previous section, this section presents the results for the unprotected head-neck (HN) model exposed to the same 260 kPa overpressure frontal blast conditions as experienced by the torso and head-neck torso models. Once again, the intent is to assess whether simulations of early-time wound injury to the head can be conducted with a truncated human model of the head-neck, or whether a more complete human model, such as the head-neck-torso model, is required to capture the complete physical behavior of the event.

Figure 28 is an image sequence depicting the progression of the blast as it interacts with the HN model. As seen previously with the Torso and HNT models, the blast wave creates a transmitted wave that propagates through the HN model. Lagrangian tracer points were located in several regions of the brain within both the HN model and the HNT model. More specifically, the Lagrangian tracers were located in the thalamus, tegmentum, anterior corpus callosum, posterior corpus callosum, left internal capsule, and right internal capsule. These tracer locations can be seen in Figure 29.

Figure 30 through Figure 35 present a comparison of the pressure and von Mises stress histories for these locations between the frontal blast simulations for the HN and the HNT models. It can be seen that the pressure histories have little deviation between the HN and HNT models for any of the given locations of interest. The minor deviations in pressure histories that do exist between the HN and HNT model appear to be slight differences in time, with the general trend in pressure magnitudes remaining consistent between the HN and HNT models. Larger deviations can be seen in the von Mises stress histories, especially after approximately 2 milliseconds of simulation time. As the von Mises

stresses increase and oscillate in late time simulations the deviation grows between HN and HNT model results.

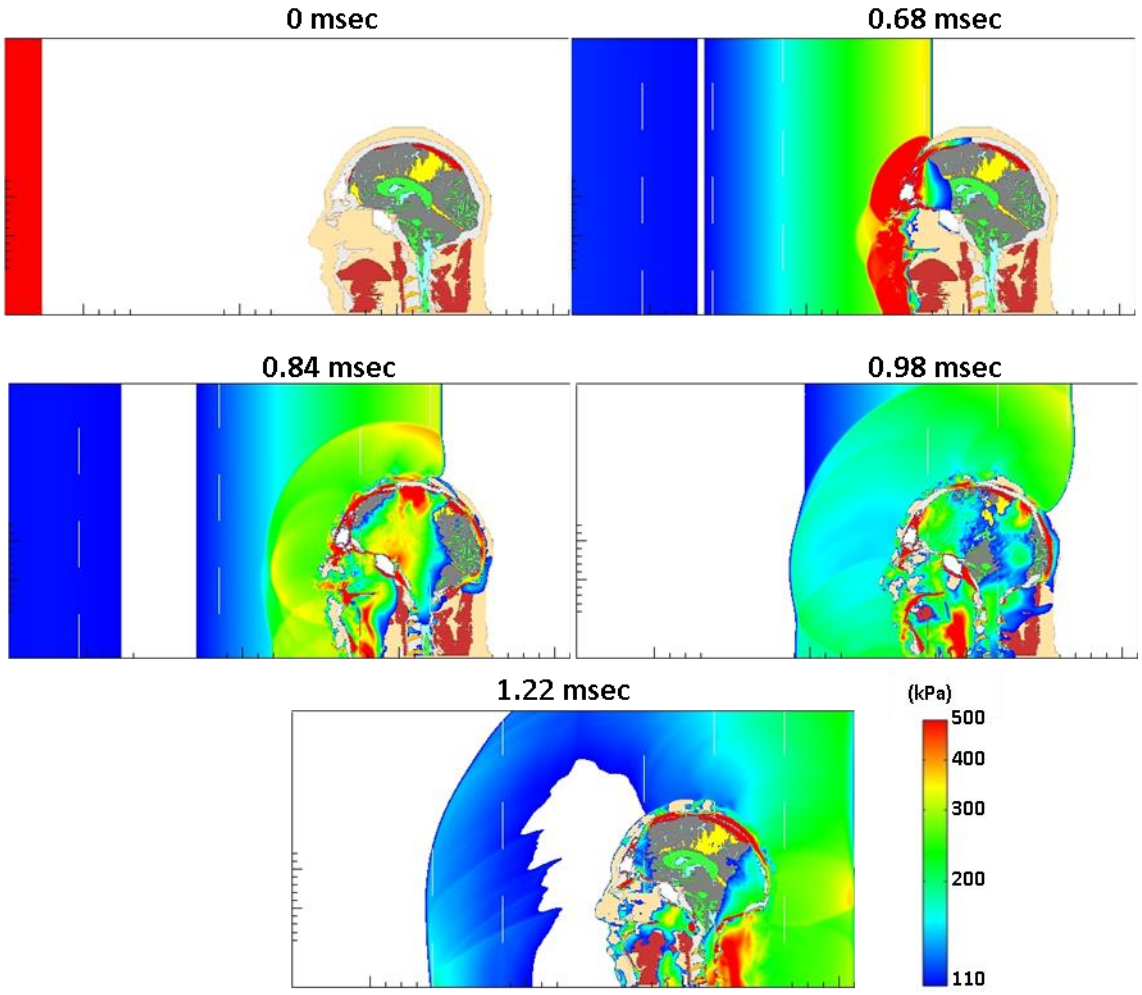

Figure 28: Pressure time-progression sequence of a 260kPa frontal blast exposure to the head-neck.

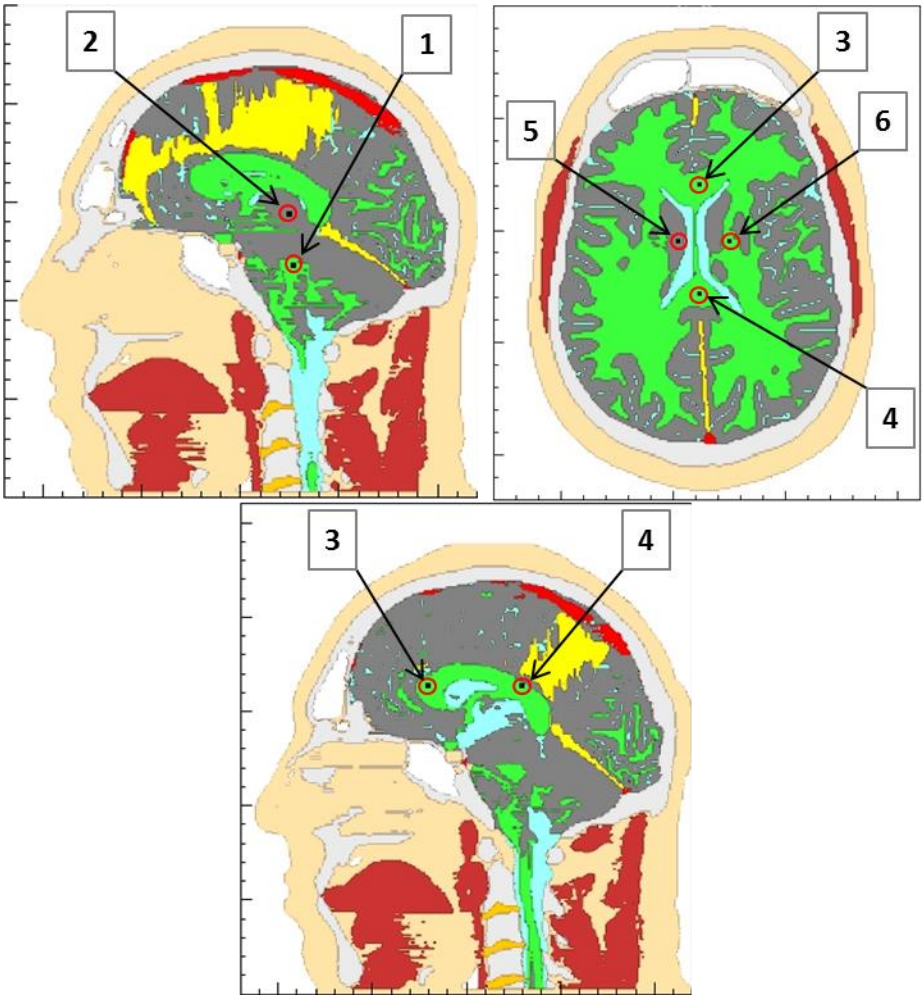

Figure 29: Lagrangian tracer point locations. (1) Tegmentum, (2) Thalamus, (3) Anterior Corpus Callosum, (4) Posterior Corpus Callosum, (5) Left Internal Capsule, (6) Right Internal Capsule.

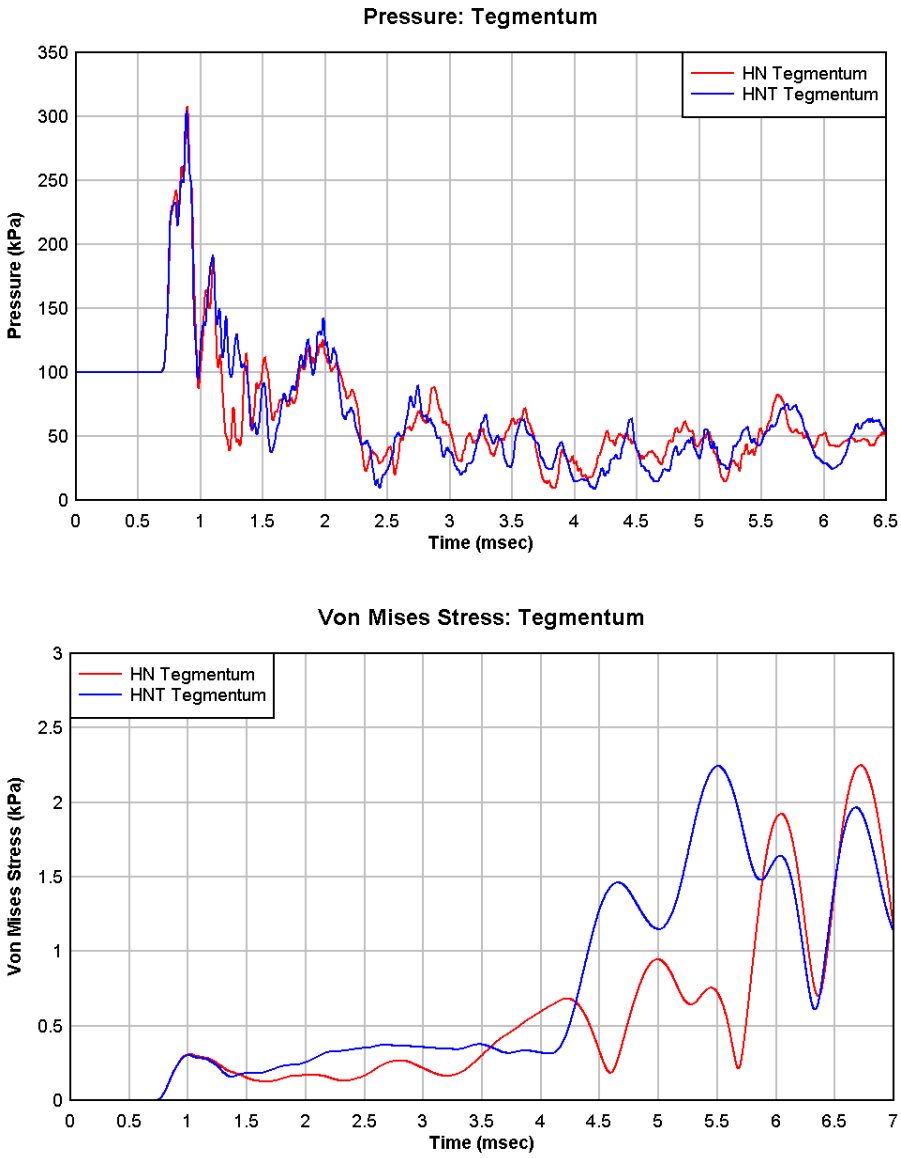

Figure 30: Tegmentum pressure (top) and von Mises Stress (bottom) histories with the comparison between simulation predictions using the head-neck model versus the full head-neck-torso model.

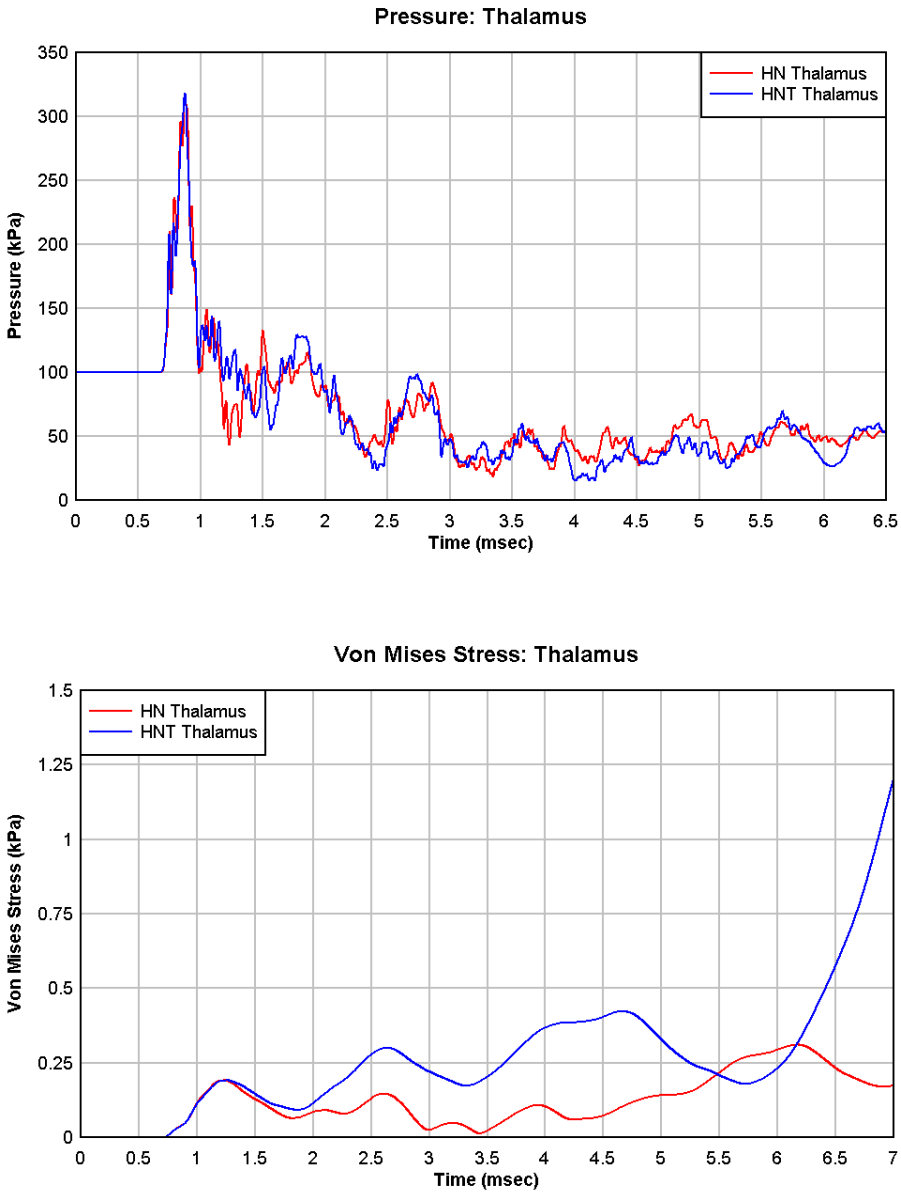

Figure 31: Thalamus pressure (top) and von Mises Stress (bottom) histories with the comparison between simulation predictions using the head-neck model versus the full head-neck-torso model.

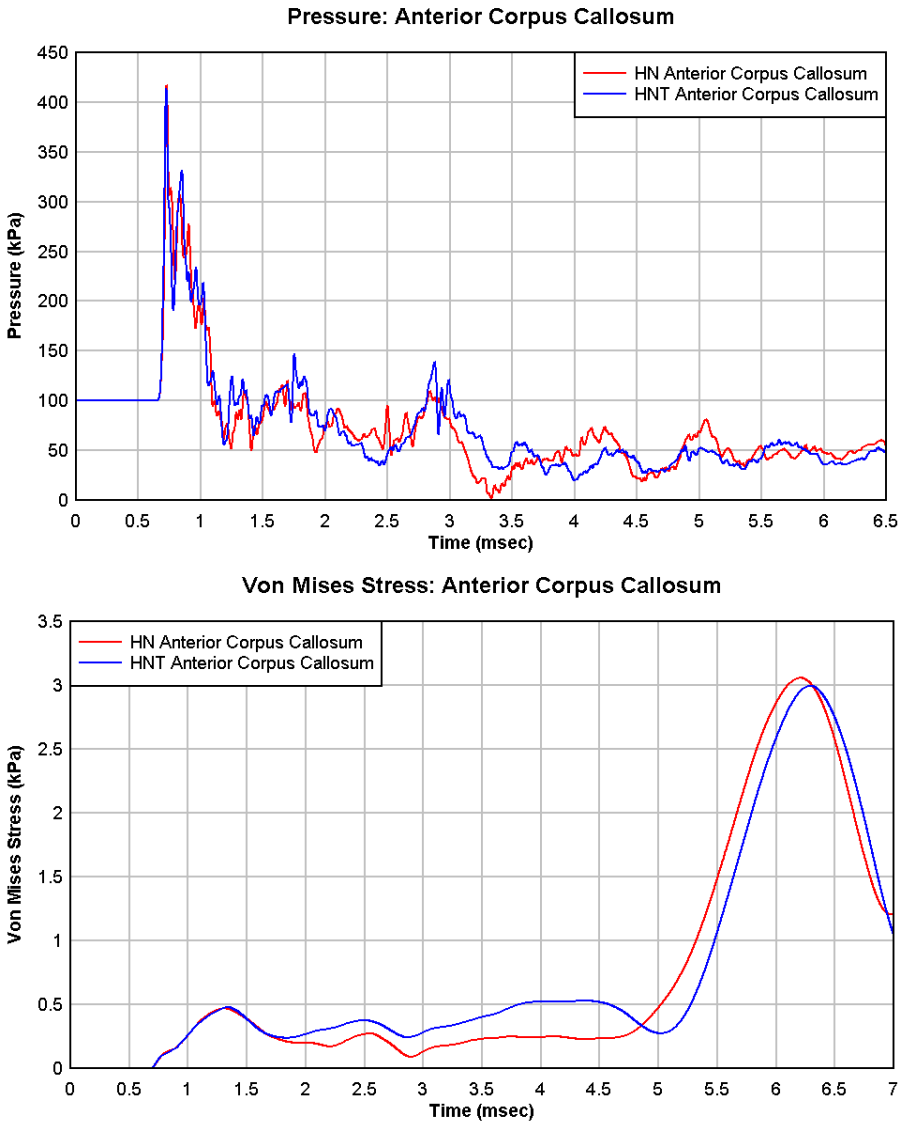

Figure 32: Anterior corpus callosum pressure (top) and von Mises Stress (bottom) histories with the comparison between simulation predictions using the head-neck model versus the full head-neck-torso model.

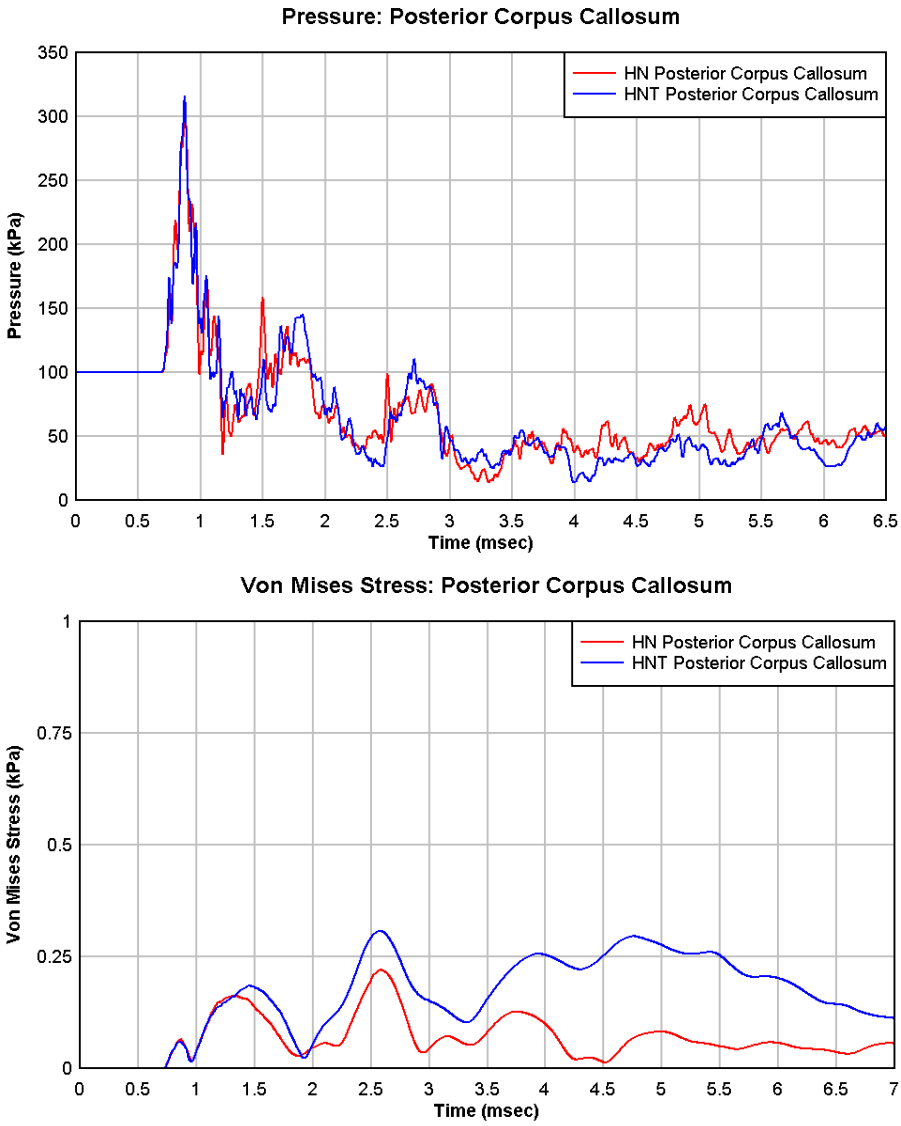

Figure 33: Posterior corpus callosum pressure (top) and von Mises Stress (bottom) histories with the comparison between simulation predictions using the head-neck model versus the full head-neck-torso model.

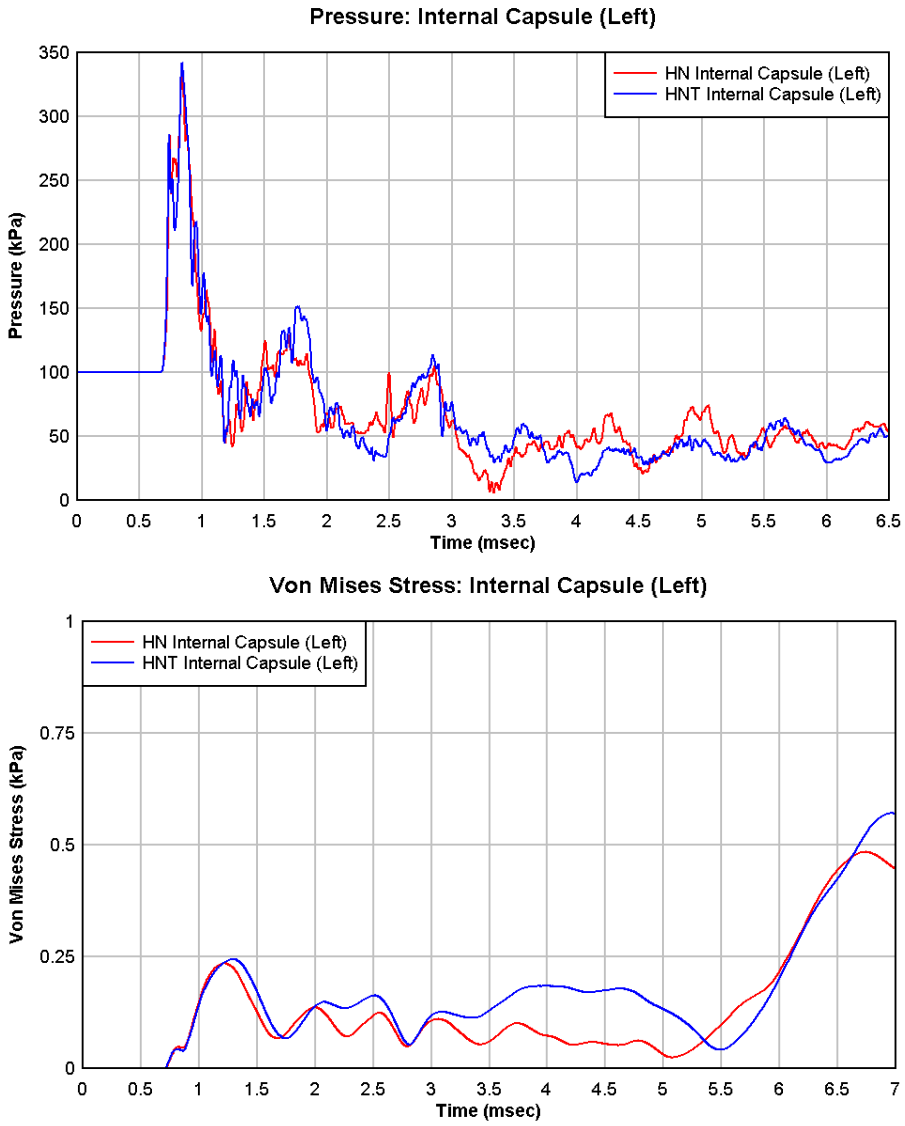

Figure 34: Left internal capsule pressure (top) and von Mises Stress (bottom) histories with the comparison between simulation predictions using the head-neck model versus the full head-neck-torso model.

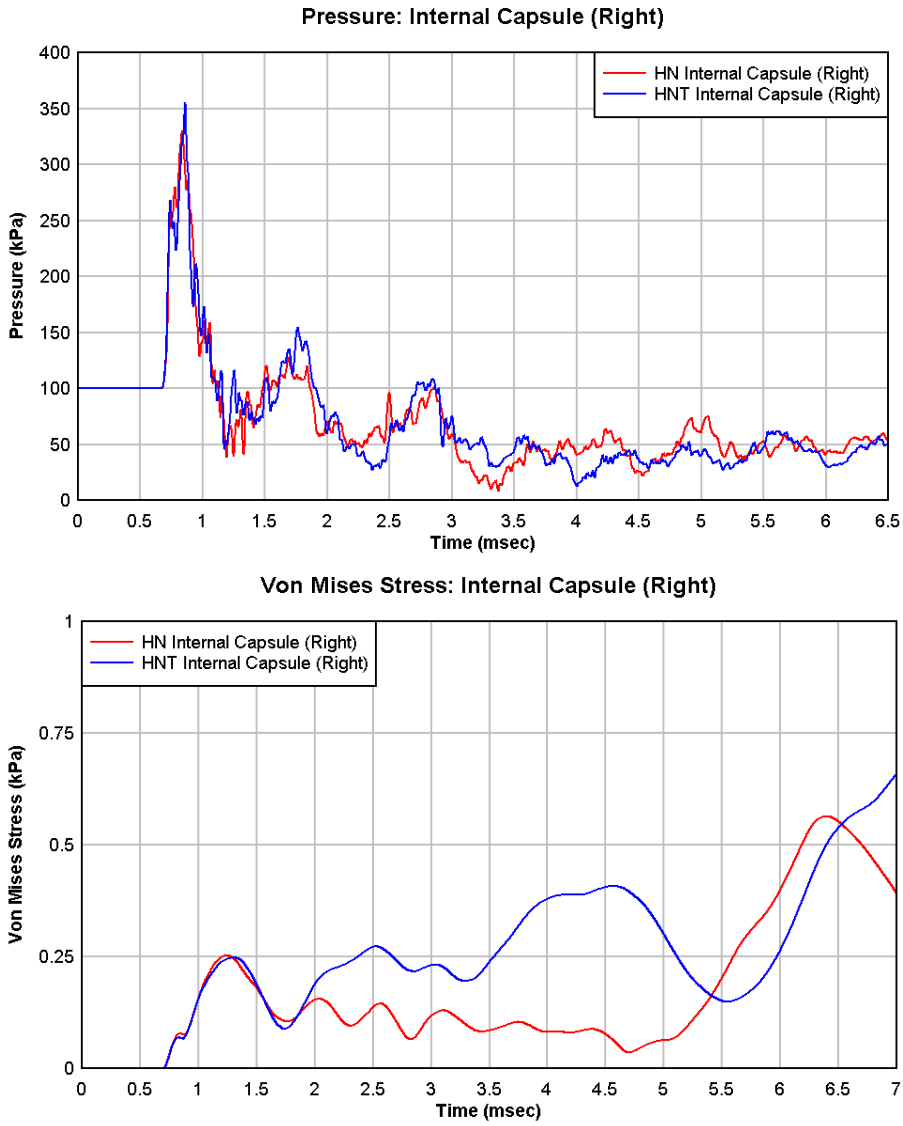

Figure 35: Right internal capsule pressure (top) and von Mises Stress (bottom) histories with the comparison between simulation predictions using the head-neck model versus the full head-neck-torso model.

To quantify the deviation in pressure histories between the HN model and HNT model simulations, the root mean square deviation (RMSD), normalized RMSD, deviation in pressure maxima, and deviation in pressure minima are calculated. The RMSD, normalized RMSD, and deviations in pressure maxima and minima are all calculated by

assessing the deviation in HN model data relative to the HNT model data at each tracer location. These results are listed in Table 3.

Table 3: Statistical deviation quantification of the pressure prediction of the head-neck simulation relative to the full head-neck torso simulation.

Tracer Location	Root Mean Square Deviation	Normalized Root Mean Square Deviation	Pressure Maxima Deviation	Pressure Minima Deviation
Tegmentum	19.24 kPa	6.0%	4.07 kPa (1%)	0.82 kPa (10%)
Thalamus	15.93 kPa	4.9%	-0.87 kPa (0%)	3.18 kPa (21%)
Anterior Corpus Callosum	20.90 kPa	4.8%	3.04 kPa (1%)	-18.29 kPa (-90%)
Posterior Corpus Callosum	17.55 kPa	5.3%	-5.50 kPa (-2%)	0.37 kPa (3%)
Internal Capsule -Left	18.74 kPa	5.5%	-9.11 kPa (-3%)	-8.35 kPa (-59%)
Internal Capsule - Right	18.99 kPa	4.9%	-25.43 kPa (-7%)	-4.39 kPa (-34%)

The relatively small normalized root mean square deviations in pressure for each tracer location indicate that pressure is predicted fairly consistently between the HN and HNT models.

The late time increases and oscillation seen in the von Mises stress histories in Figure 30 through Figure 35 may be due to an inadvertent boundary condition effect. Specific boundary conditions are employed in order to create conditions that allow the blast front to propagate in the surrounding air while preventing ambient pressure from increasing, as it would in a completely enclosed space. Specifically, the boundaries anterior and inferior

to the human models are rigid while the boundaries lateral, posterior, and superior to the human models allow for material, including air, to flow out of the computational space. Figure 36 depicts both the total air mass within the entire computational space as well as the pressure history at a Lagrangian tracer point placed external of the HNT model just anterior to the sternum. It should be noted that the 360 kPa (260 kPa overpressure) incident pressure pulse passes the Lagrangian tracer at approximately 0.5 milliseconds and a secondary pressure pulse, reflected from the HNT model back toward the front boundary of the computational space, occurs between 0.5 and 1 millisecond. After these initial external blast interactions occur, the total air mass within the computational space begins to decline just after 1 millisecond simulation time. The simulation begins with an ambient pressure of 100 kPa, or approximately 1 atmosphere; however, as the air mass begins to leave the computational space, partial to perfect vacuum conditions are created. These vacuum conditions potentially create stresses on the materials comprising the various human models at late simulation times.

To quantify the deviation in von Mises stress histories for the various Lagrangian tracer points within the HN and HNT models, two approaches were taken. The root mean square deviation (RMSD), normalized root mean square deviation, and deviation in von Mises stress maxima were evaluated for simulation time up to 2.25 milliseconds, when approximately half of the total air mass remains within the simulation, as well as for the entire simulation up to 7.0 milliseconds time.

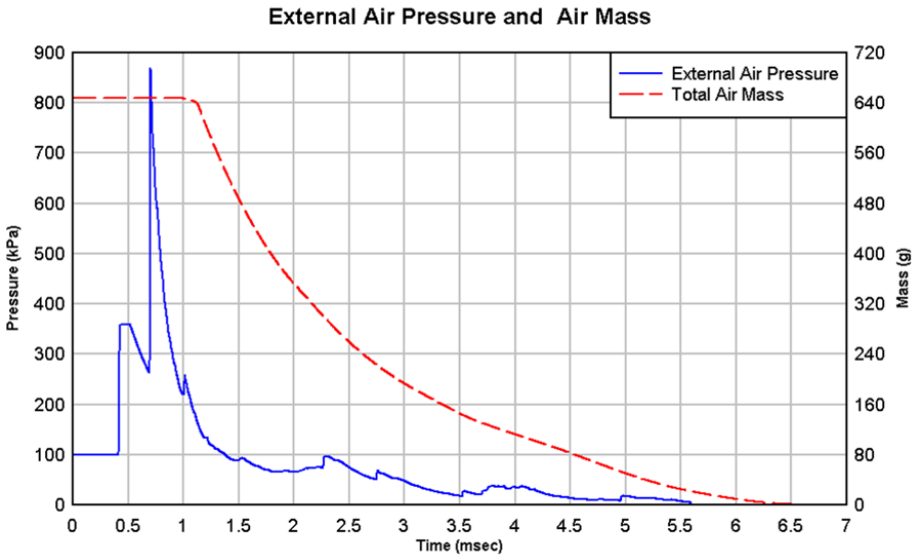

Figure 36: External air pressure history at a point located just anterior to the sternum and total air mass history within the computational space.

The RMSD, normalized RMSD, and difference in von Mises stress maxima are all calculated by assessing the deviation in HN model data relative to the HNT model data at each tracer location. Table 4 lists the statistical deviation quantification of the von Mises stress predictions up to 2.25 milliseconds simulation time and Table 5 lists the results up to 7.0 milliseconds. It is noted that the relative errors are much greater when assessing the full simulation time relative to the errors calculated up to the earlier simulation time of 2.25 milliseconds when some air still remains within the computational space. This result suggests that the simulations may be of higher accuracy if the surrounding air can somehow remain present in the simulation.

Table 4: Statistical deviation quantification of the von Mises stress prediction of the head-neck simulation relative to the full head-neck torso simulation up to 2.25 milliseconds simulation time.

Tracer Location	Root Mean Square Deviation	Normalized Root Mean Square Deviation	VMS Maxima Deviation
Tegmentum	59.0 Pa	18.0%	-17.3Pa (-5.3%)
Thalamus	27.2 Pa	14.2%	-0.6 Pa (-0.3%)
Anterior Corpus Callosum	41.8 Pa	8.8%	-8.1 Pa (-1.7%)
Posterior Corpus Callosum	28.6 Pa	15.4%	-23.3 Pa -(12.6%)
Internal Capsule - Left	21.7 Pa	8.9%	-8.7 Pa (-3.6%)
Internal Capsule - Right	30.0 Pa	12.1%	4.7 Pa (1.9%)

Table 5: Statistical deviation quantification of the von Mises stress prediction of the head-neck simulation relative to the full head-neck torso simulation up to 7.0 milliseconds simulation time.

Tracer Location	Root Mean Square Deviation	Normalized Root Mean Square Deviation	VMS Maxima Deviation
Tegmentum	505 Pa	22.5%	5.70 Pa (0.3%)
Thalamus	240 Pa	20.2%	-878 Pa (-73.9%)
Anterior Corpus Callosum	209 Pa	7.0%	62.8 Pa (2.1%)
Posterior Corpus Callosum	123 Pa	40.2%	-86.0 Pa (-28.0%)
Internal Capsule - Left	60.5 Pa	10.7%	-86.3 Pa (-15.1%)
Internal Capsule - Right	160 Pa	24.4%	-92.4 Pa (-14.1%)

In considering the deviation quantification calculations for both pressure and von Mises stress presented here, the only assessment that has been made is in understanding the deviation of the HN model data relative to the HNT model data. While the normalized RMSD errors may range anywhere from 4.8% for the pressure in the anterior corpus callosum up to 40.2% for the von Mises stress in the posterior corpus callosum, this does not necessarily indicate a deviation that is significant when considering wound injury thresholds. To determine the significance of the magnitude of these errors, more research must be done in understanding the injury thresholds for pressure and von Mises stress in these particular tissues and their locations.

To assess the variation in pressure predictions between the HN and HNT models in a more global sense, the maximum tensile and compressive pressure reached throughout the entirety of the simulation is visualized in Figure 37 through Figure 40. Figure 37 and Figure 38 depict the maximum compressive pressure on the external surface and mid-sagittal plane of the brain respectively. Figure 39 and Figure 40 depict the maximum tensile pressure on the external surface and mid-sagittal plane of the brain respectively. Although the pressures appear relatively consistent at the Lagrangian tracer points, some variation between model predictions is notable by visualizing the data in this manner. Specifically, the HN model predicts some localized regions of relatively high compressive pressure near the pons and occipital region which are not as prominent in the HNT predictions. The HN model also predicts greater tensile pressures in the brain stem, cerebellum, pons, midbrain, and the anterior region of the frontal lobe. To assist the reader in identifying the areas of the brain mentioned in this section, illustrations serving as a brief overview of the anatomy of the brain have been placed in Appendix B.

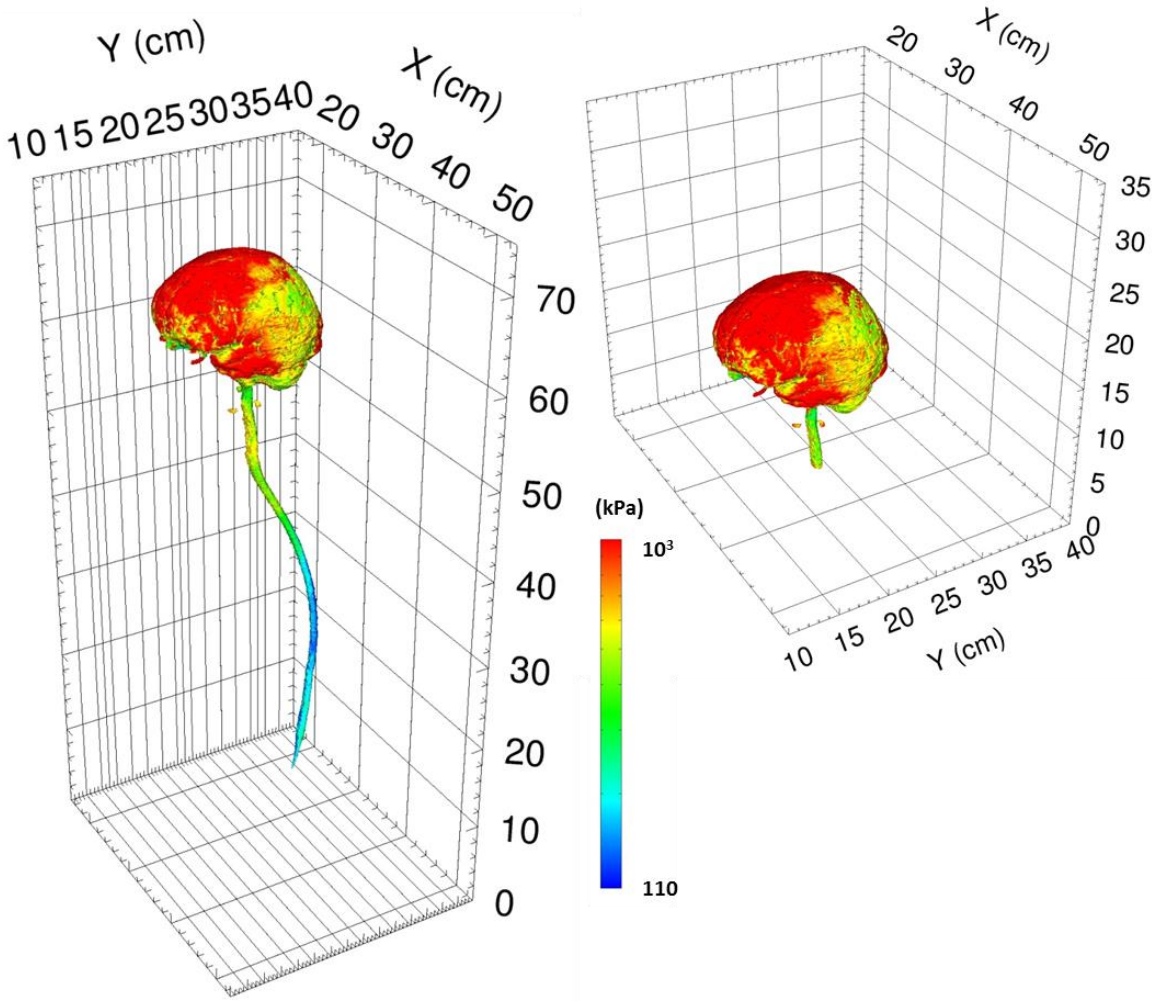

Figure 37: Maximum compressive pressure occurring on the surface of the brain at any time up to 7.0 msec simulated time for the HNT model (left) and HN model (right).

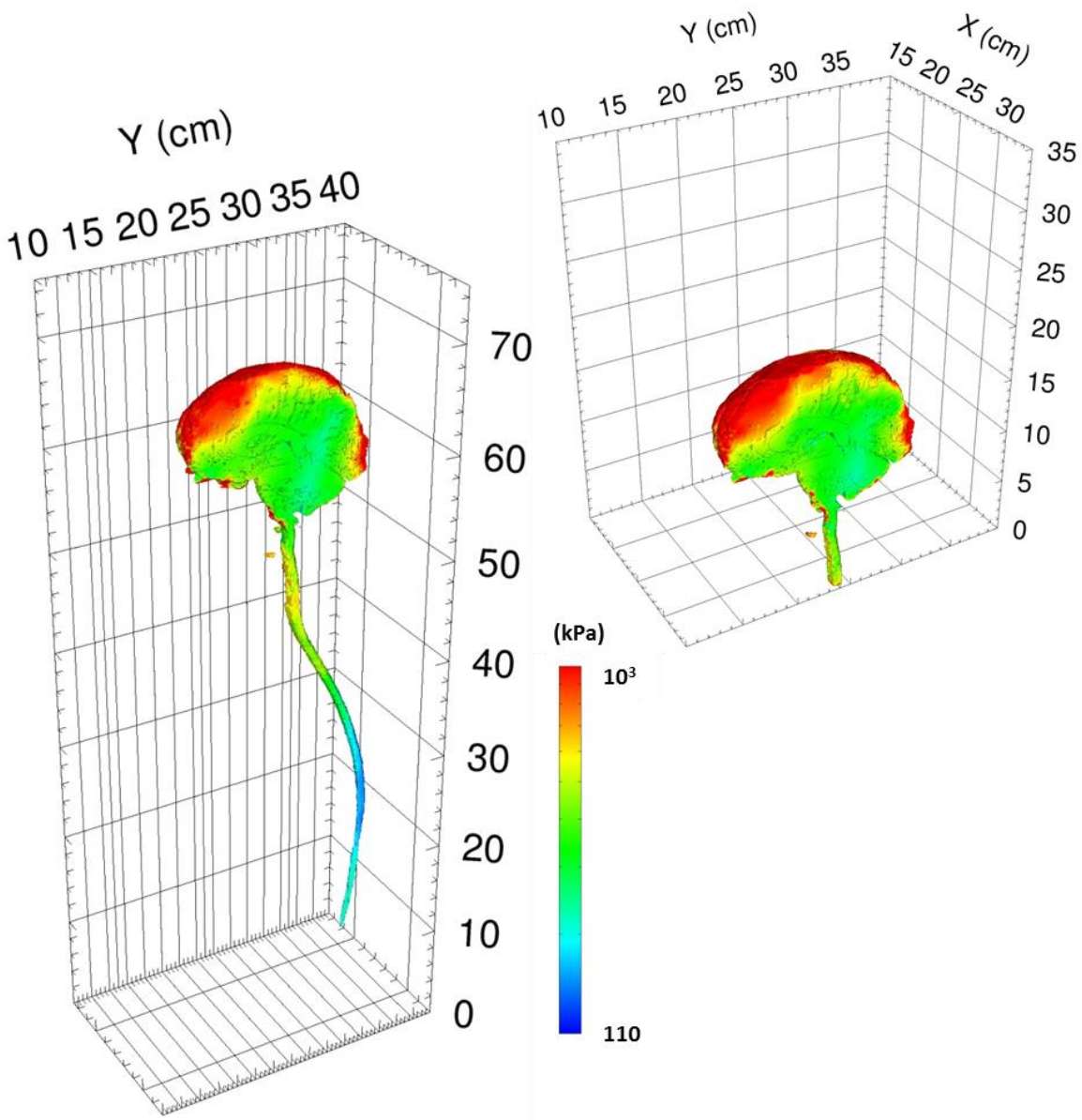

Figure 38: Maximum compressive pressure occurring at the mid-sagittal plane at any time up to 7.0 msec simulated time for the HNT model (left) and HN model (right).

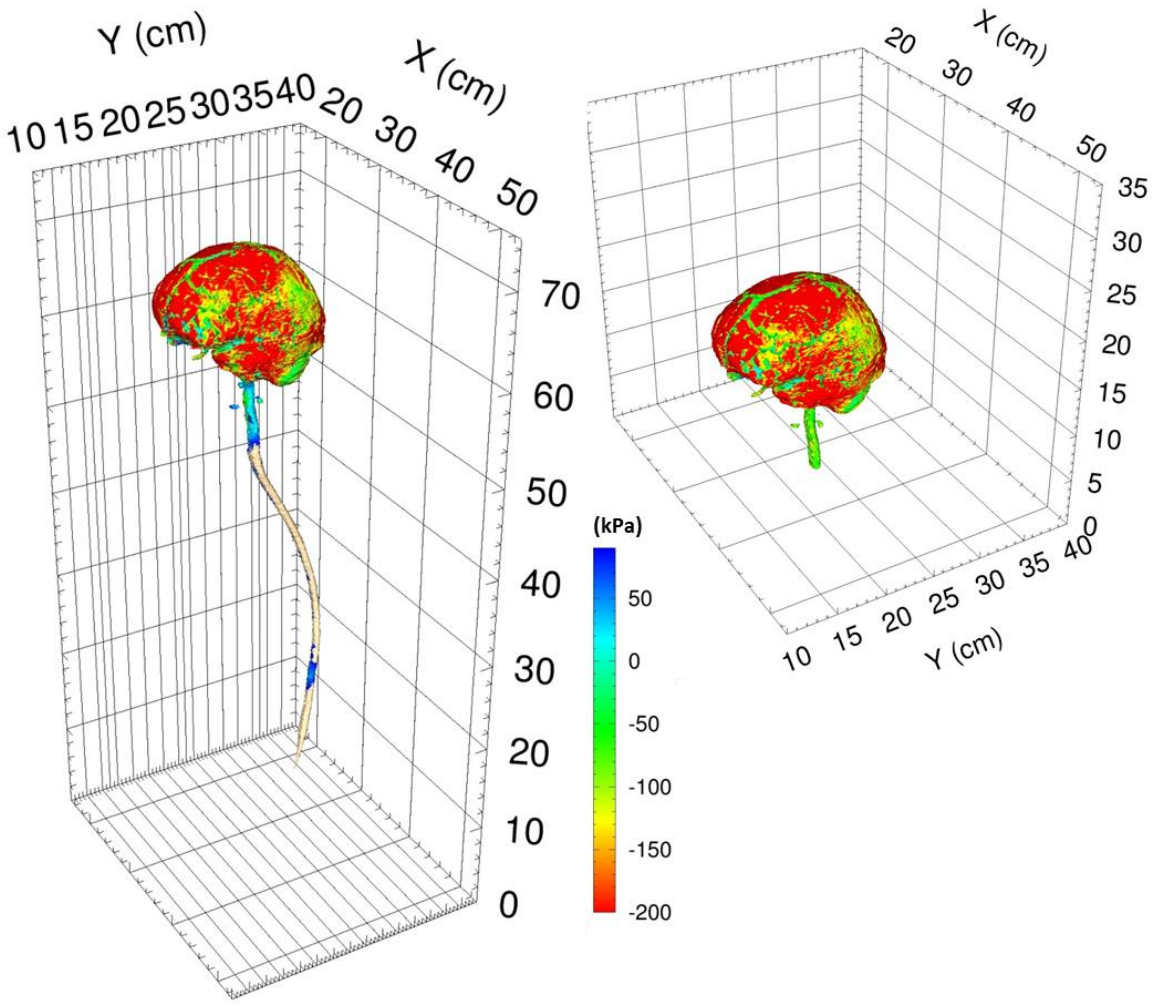

Figure 39: Maximum tensile pressure occurring on the surface of the brain at any time up to 7.0 msec simulated time for the HNT model (left) and HN model (right).

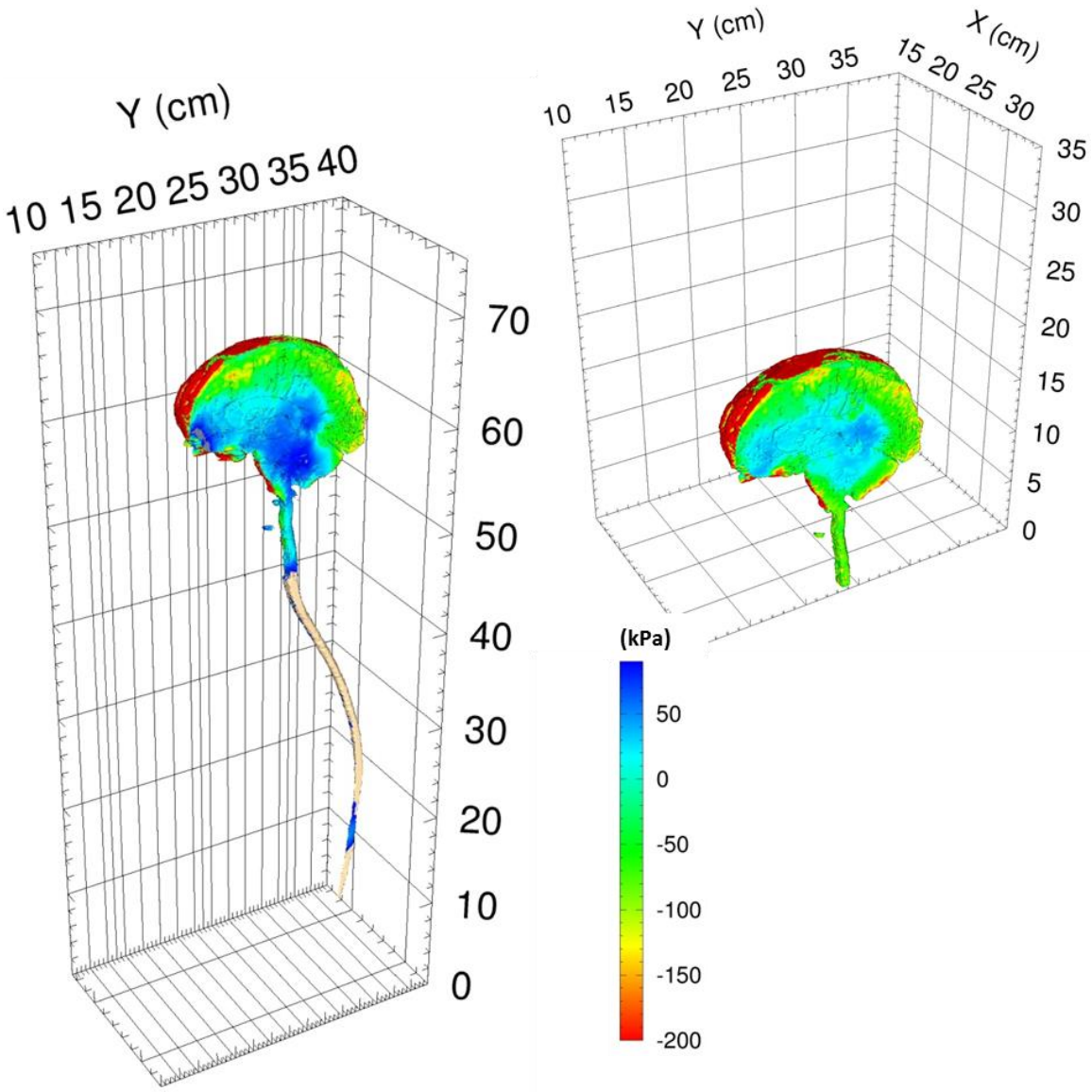

Figure 40: Maximum tensile pressure occurring at the mid-sagittal plane at any time up to 7.0 msec simulated time for the HNT model (left) and HN model (right).

5 Discussion

The execution of this research has resulted in the development of high fidelity representations of the human male torso and head-neck-torso and a simulation methodology with which to conduct wound injury investigations and relative assessments of personal armor. Simulations conducted throughout the course of this research include relative armor assessments of notional armor and simulations with which to assess the utilization of truncated torso and truncated head-neck models relative to the more complete head-neck-torso model.

5.1 Relative Armor Assessments

Relative armor assessments were conducted with the human torso model for prototype armor configurations against both projectile impact and blast impact. While the results for these simulations are not intended to describe a quantitative assessment of wound dynamics, they are valuable in illustrating the capability of the modeling and simulation approach developed through this research to provide a unique and appealing method of conducting relative armor assessments. With this modeling and simulation approach various armor designs can be assessed relative to baseline or previous armor designs through the monitoring of stress, strain, energy, stress power, acceleration, and damage measures at any location throughout the human models. Subtle trends in data that may potentially be associated with injury can be identified through post processing such as the decreased pressure load rates associated with peak pressure increases seen in the heart and liver for blast impact to the protected torso.

The extensive monitoring and post-processing capabilities also provide an opportunity to assist in the optimization of armor systems. It can be seen from the pressure and von Mises plots of the illustrative simulations described for a protected torso subjected to either projectile impact or blast impact that the inclusion of high impedance foam padding behind the armor shell results in transmitted pressure and shear stresses into the torso. By adjusting the prototype armor in the illustrative simulations to a design with no padding, the resulting pressure and von Mises stresses are reduced. While this is a simplistic illustration, it highlights the value of this modeling and simulation approach in identifying areas for improvement in various armor systems and the ability to assist in optimizing armor systems by assessing designs and design modifications without the need to produce each design variation for physical testing.

5.2 Truncated Model Utilization

Simulations were conducted assessing the performance of the truncated head-neck model and truncated torso model against the more complete head-neck-torso model. The results of the comparison between the frontal blast impact to the torso model and to the head-neck-torso model identified relative consistency between the models. This is tempered by the fact that the torso simulation develops a non-recoverable error at a relatively early simulation time of approximately 2 milliseconds due to high magnitude pressure waves created at the upper boundary. For this reason alone, it is valuable to utilize the more complete head-neck-torso model in order to reduce boundary condition effects for blast simulations or simulations that produce biomechanical responses globally throughout the human models. The truncated torso model is effective in assessing injury scenarios with localized effects, such as a projectile impact simulation or blunt impact simulation. It is

also conceivable that the torso model would be the more computationally efficient approach toward studying a specific injury mechanism if it has been identified to occur within 2 milliseconds of impact. Further calculations quantifying data deviation between the torso and head-neck-torso were considered to be unnecessary as the torso simulation terminated at a relatively early simulation time and did not provide extensive data to interrogate. This specific limitation may be negated if the boundary condition effects can be overcome.

The frontal blast simulations comparing the head-neck to the head-neck-torso model resulted in modest agreement between models for compressive pressure predictions at the Lagrangian tracer points of interest; however, upon assessing maximum compressive and tensile pressure from a global perspective, more variations in the pressure predictions between the models became evident. These results suggest that for the greatest relative accuracy, the more complete HNT model or a full human model should be used to assess blast impact. However, it may be possible that the pressure deviations seen in the HN model can be further reduced if adjustments are made to the boundary conditions employed in the HN model simulation.

Large deviations were also seen for the von Mises stress. Further investigation into the external conditions occurring after the blast event revealed a loss in air mass within the computational space accompanied by a loss in ambient pressure. These conditions lead to partial and even perfect vacuum conditions. It is believed to be the case that the vacuum conditions may lead to internal stresses on the materials comprising the head-neck and head-neck-torso models. The late time increase and oscillation in von Mises stress seen in

the results are not thoroughly understood at this time and more research must be conducted toward understanding this behavior.

The deviation in pressure or von Mises stress between models is quantified only as a relative measure between model results and does not necessarily indicate a significant deviation so far as wound injury thresholds are concerned. To determine the significance of said deviations, more research must be conducted toward understanding injury thresholds of the particular tissue types for pressure and von Mises stress at the particular locations of interest.

6 Future Work

Although significant accomplishments have been made throughout the course of this research, the important task of validating the torso and head-neck-torso model still remains to be completed. Unfortunately, there exists a significant absence of accessible battlefield injury data with which to quantitatively validate the human models. This data likely exists; however, it is extremely difficult to acquire due to restrictions imposed on said data by the data owners or archivists. Having limited access to validation data constitutes one of the greatest limitations to the modeling and simulation investigations of wound injury and personal armor assessments. Modeling and simulation efforts will continue to be hindered by this limitation until the research community can convince the archivists of warfighter injury data to release the data in order to advance the state-of-the-art of in-silico injury scenario investigations. Even without completely validated models, armor assessments can continue to be conducted in a relative manner.

The results for the blast impact simulation employing the updated HN model suggest a potential advancement in modeling accuracy from previous work conducted by Taylor et al. [6]. Significant deviations in results are seen between those which are presented here and those presented by Taylor et al. for the same blast impact simulation employing the HN model. This is potentially a result of correcting the anterior table thickness of the frontal sinus leading to greater energy transfer into the brain, whereas in previous work by Taylor, the bone around the sinus appeared to be fracturing and no longer providing a continuous medium for pressure wave propagation and transfer through the bone and into the brain. The inclusion of the intervertebral discs and vasculature in the updated HN

model may also play a role in these deviations. These assumptions require further research and understanding.

As discussed in section 3.2, many of the material model representations are simplistic in order to allow for the initiation of testing the modeling and simulation approach and illustrating the potential value of such an approach. All of the materials comprising the human models are currently modeled by isotropic best-fit approximations and most materials are modeled with linear-elastic perfectly-plastic representations. Significant advancements can be made in fitting orthotropic non-linear material models to relevant data sourced from published literature. The implementation of orthotropic material models would require a significant and novel development within the simulation code, CTH. This development would require a way to track the surface of a material, perhaps with vectors at every point on the material surface defining the surface normal direction. These vectors would describe the changing curvature of the material with which to relate the orthotropic material models. These vectors must be updated at every time step as the material deforms and potentially advects from one computational cell into another. The difficulties of such a development are complicated by the Eulerian framework, and may be better suited for a Lagrangian framework. Material models with parameters which vary based on material density as measured from CT or MRI scans would also be a valuable advancement.

The current modeling and simulation approach is limited to early-time injury investigations. This limitation exists in part due to the lack of model articulation as well as due to difficulties that exist in capturing large deformations of multiple distinct adjacent materials within an Eulerian framework such as CTH. Implementation of an

articulating model within a Lagrangian or a coupled Eulerian-Lagrangian framework would allow for investigation into later time injury scenarios as well as a virtual approach toward armor system ergonomic assessments, once again potentially reducing the necessity for producing expensive prototypes for physical testing.

An extension of the current head-neck-torso model to include the arms, hands, urogenital area, legs, and feet would provide a complete human model and broaden the applicability of the current modeling and simulation toolset. With a recent marked increase in female warfighters in combat positions, the creation of a female human model would also be a highly desirable addition, especially for conducting armor assessments for armor systems that are designed for the female warfighter.

The potential areas for growth of the described modeling and simulation approach are vast; however, it should not be considered a replacement for physical experimentation. Physical experimentation is necessary and of great value to the modeling and simulation research community. Without physical experimentation, the material properties necessary to fit material model representations would be unknown and data with which to validate against would be non-existent. Experimental research and computational research ought to continue in a symbiotic manner, each assisting the other in producing the highest quality data as efficiently and effectively as possible.

7 APPENDIX A

Contained within this appendix are the locations of the columns of Lagrangian tracer points across the head-neck-torso junction plane and their associated stress and Lagrangian strains for continuity verification discussed within section 3.1.3.

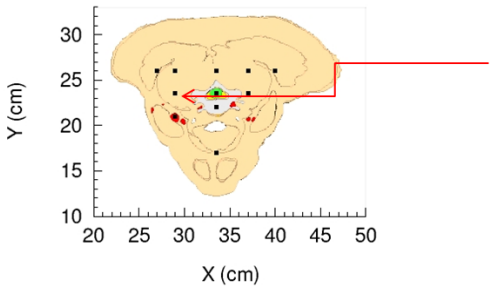

Tracer # 4 (z=49.65)
15(z=49.75)
26(z=49.85)
37(z=49.95)

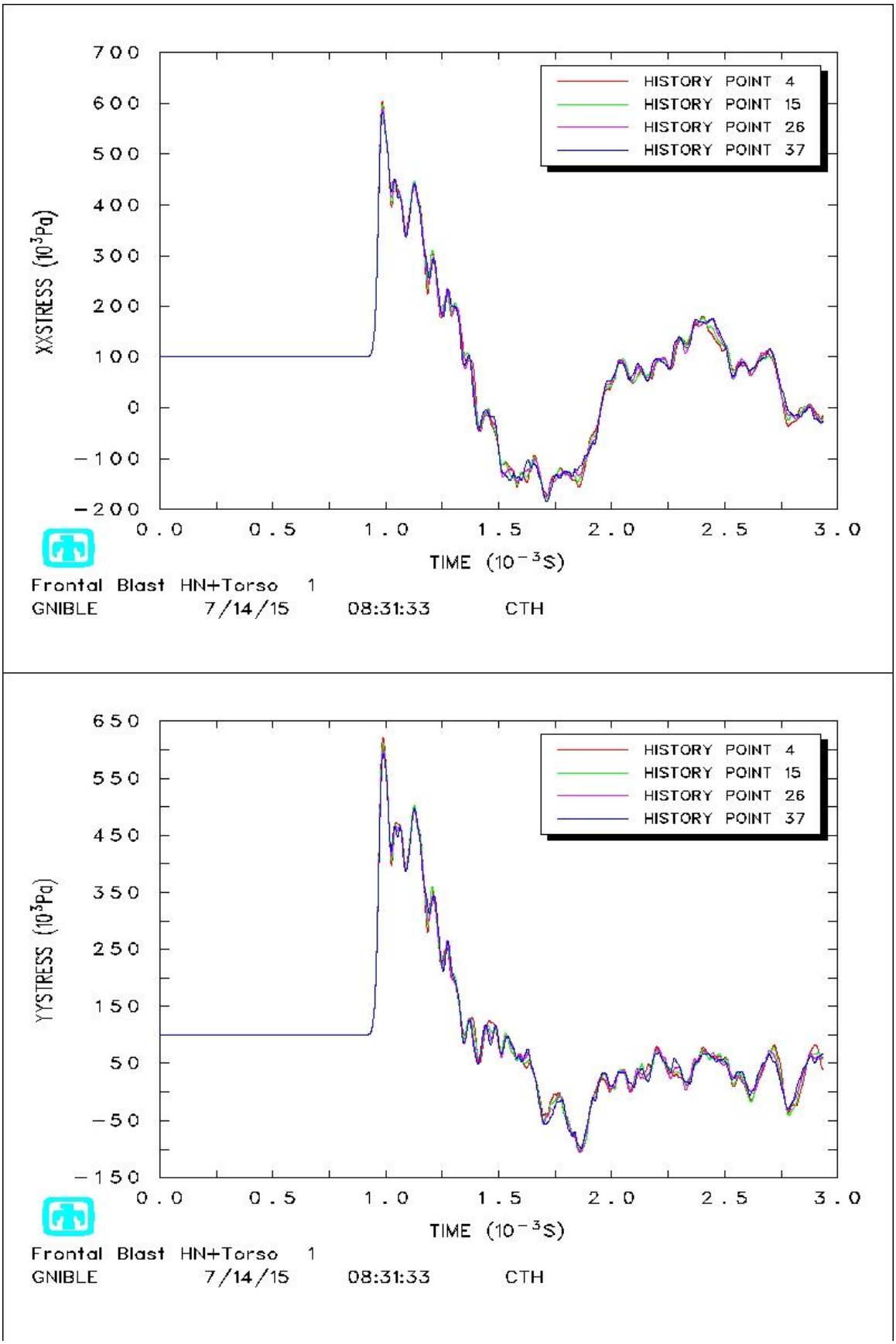
700
600
500
400
300
200
100
0
−100
−200
XXSTRESS (10³Pa)
0.0
0.5
1.0
1.5
2.0
2.5
3.0
TIME (10⁻³S)
HISTORY POINT 4
HISTORY POINT 15
HISTORY POINT 26
HISTORY POINT 37
Frontal Blast HN+Torso 1
GNIBLE 7/14/15 08:31:33 CTH
650
550
450
350
250
150
50
−50
−150
YYSTRESS (10³Pa)
0.0
0.5
1.0
1.5
2.0
2.5
3.0
TIME (10⁻³S)
HISTORY POINT 4
HISTORY POINT 15
HISTORY POINT 26
HISTORY POINT 37
Frontal Blast HN+Torso 1
GNIBLE 7/14/15 08:31:33 CTH

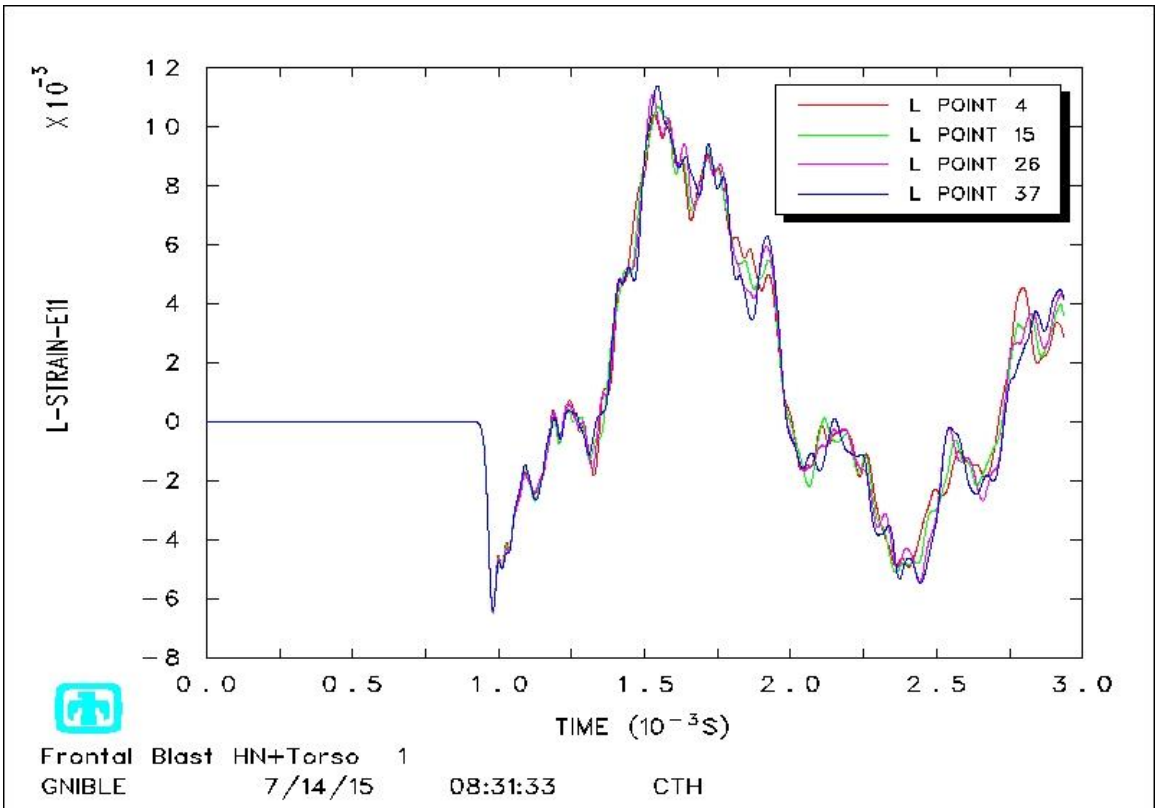
X10-3
L-STRAIN-E11
12
10
8
6
4
2
0
-2
-4
-6
-8
0.0
0.5
1.0
1.5
2.0
2.5
3.0
TIME (10-3S)
L POINT 4
L POINT 15
L POINT 26
L POINT 37
Frontal Blast HN+Torso 1
GNIBLE 7/14/15 08:31:33 CTH

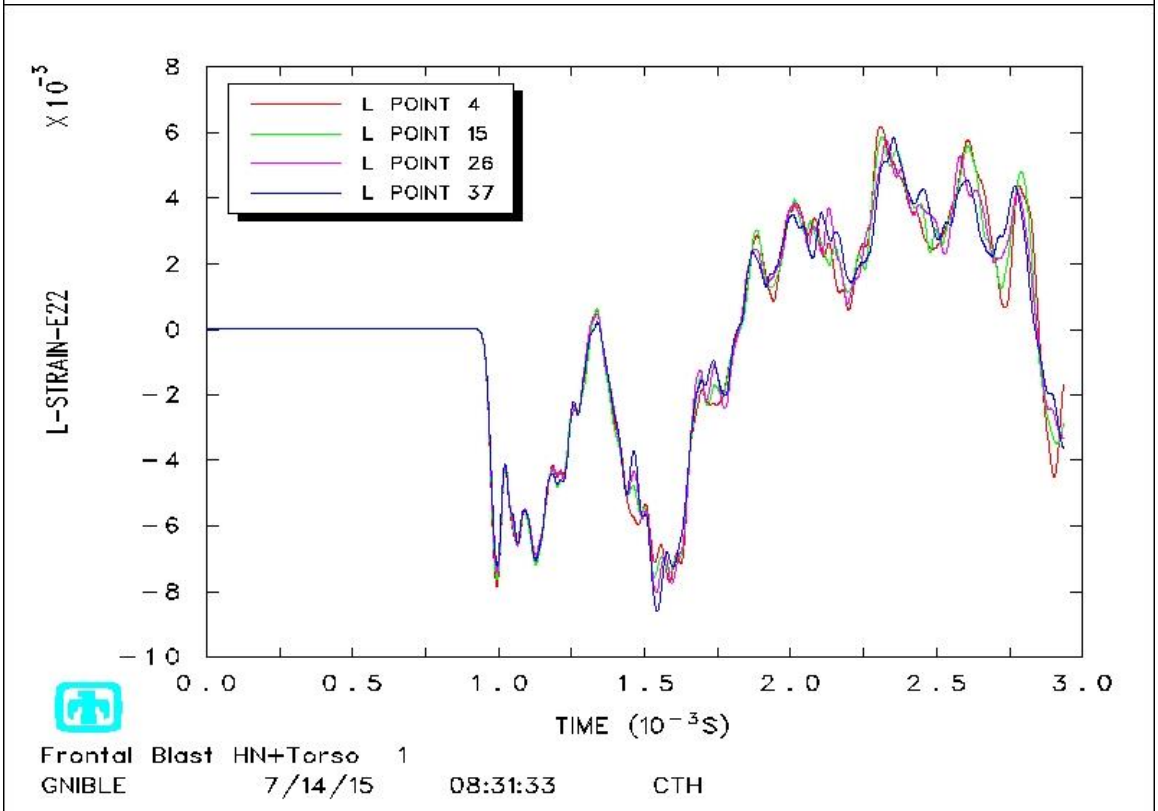
X10-3
L-STRAIN-E22
8
6
4
2
0
-2
-4
-6
-8
-10
0.0
0.5
1.0
1.5
2.0
2.5
3.0
TIME (10-3S)
L POINT 4
L POINT 15
L POINT 26
L POINT 37
Frontal Blast HN+Torso 1
GNIBLE 7/14/15 08:31:33 CTH

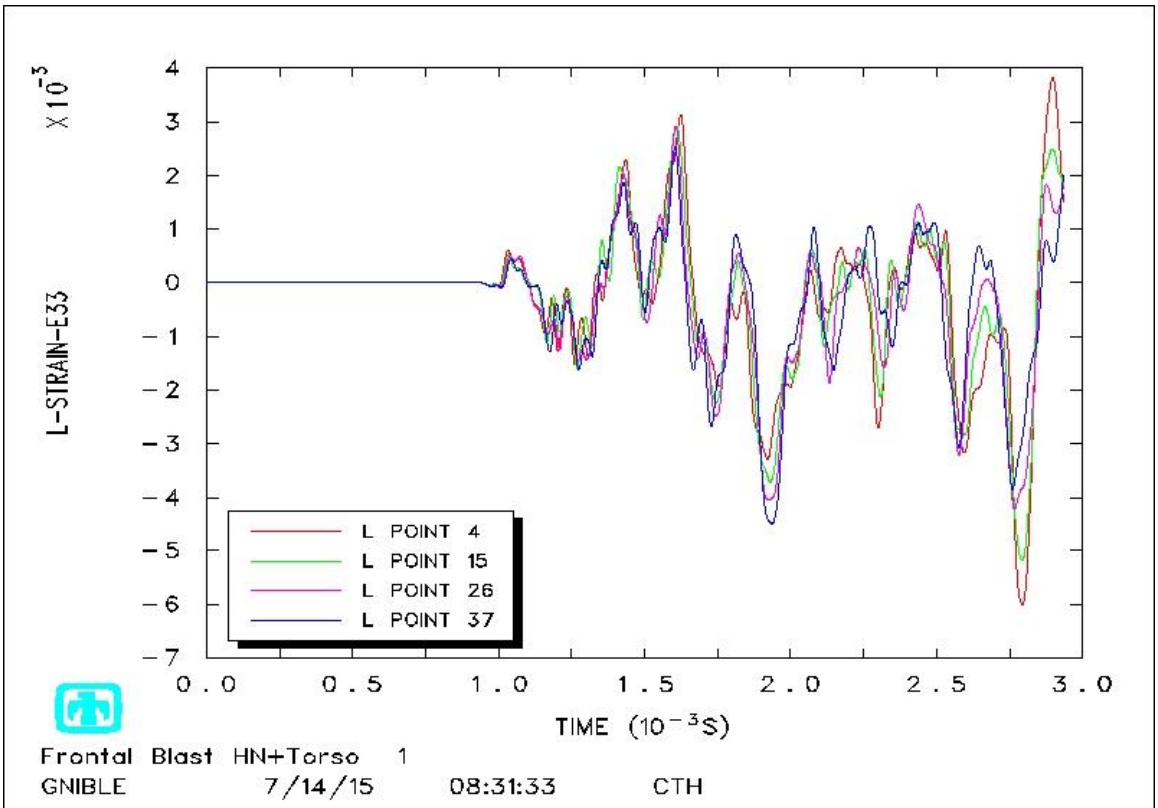
X 10^-3
L-STRAIN-E33
4
3
2
1
0
-1
-2
-3
-4
-5
-6
-7
L POINT 4
L POINT 15
L POINT 26
L POINT 37
0.0
0.5
1.0
1.5
2.0
2.5
3.0
TIME (10^-3S)
Frontal Blast HN+Torso 1
GNIBLE 7/14/15 08:31:33 CTH

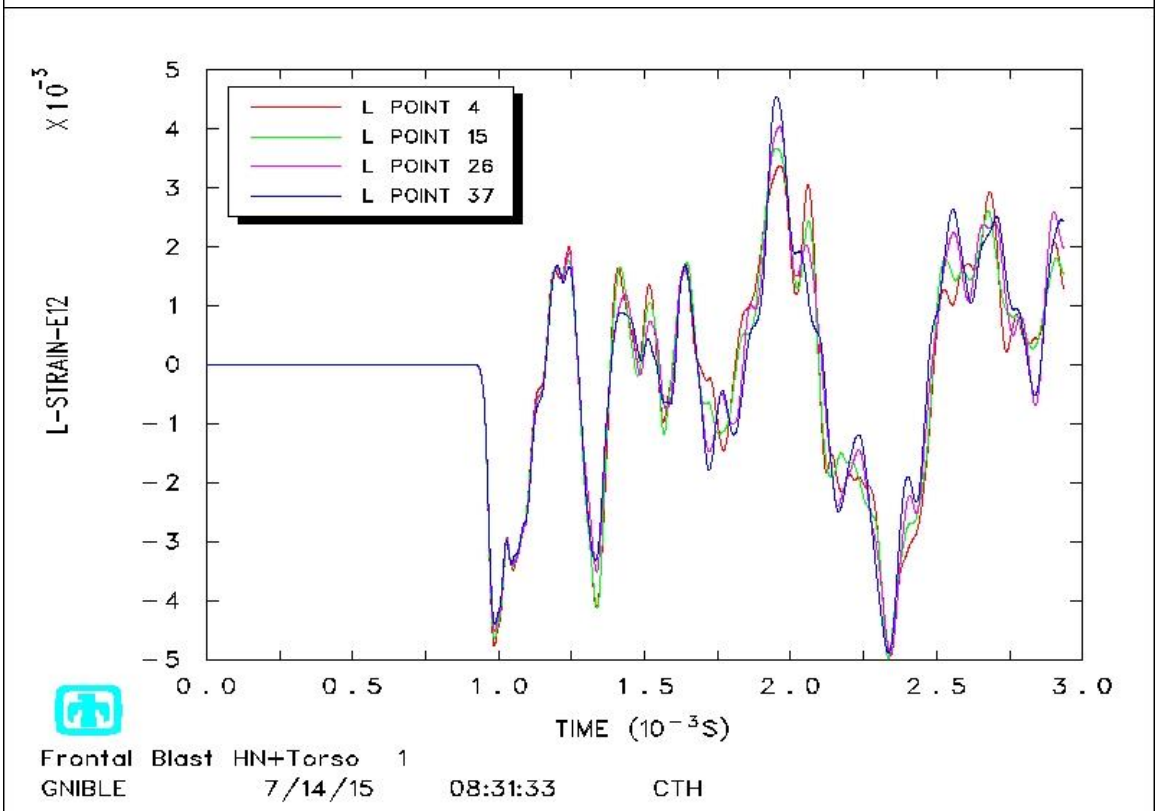
X 10^-3
L-STRAIN-E12
5
4
3
2
1
0
-1
-2
-3
-4
-5
L POINT 4
L POINT 15
L POINT 26
L POINT 37
0.0
0.5
1.0
1.5
2.0
2.5
3.0
TIME (10^-3S)
Frontal Blast HN+Torso 1
GNIBLE 7/14/15 08:31:33 CTH

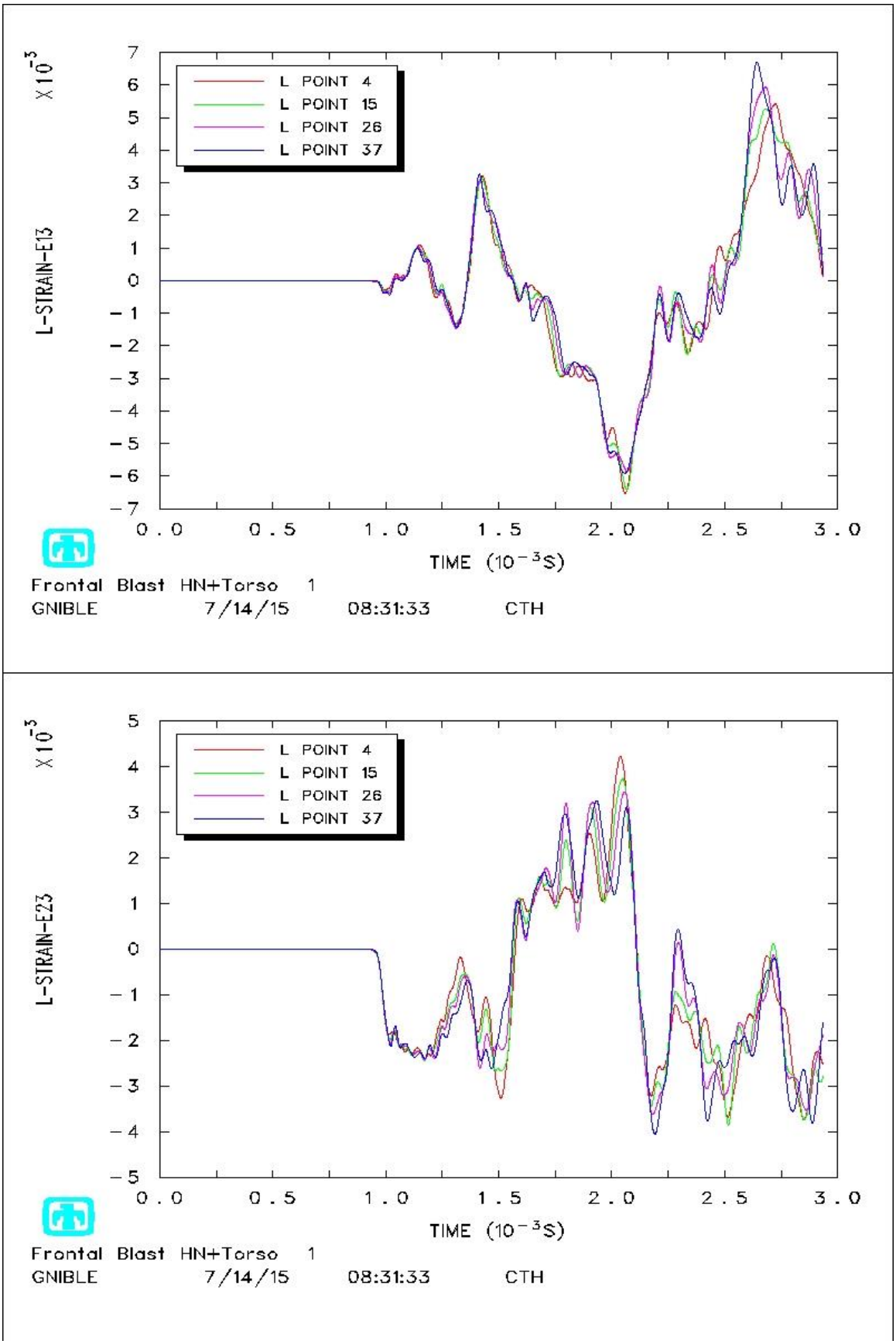
X 10^-3
L-STRAIN-E13
L POINT 4
L POINT 15
L POINT 26
L POINT 37
7
6
5
4
3
2
1
0
-1
-2
-3
-4
-5
-6
-7
0.0
0.5
1.0
1.5
2.0
2.5
3.0
TIME (10^-3S)
Frontal Blast HN+Torso 1
GNIBLE 7/14/15 08:31:33 CTH
X 10^-3
L-STRAIN-E23
L POINT 4
L POINT 15
L POINT 26
L POINT 37
5
4
3
2
1
0
-1
-2
-3
-4
-5
0.0
0.5
1.0
1.5
2.0
2.5
3.0
TIME (10^-3S)
Frontal Blast HN+Torso 1
GNIBLE 7/14/15 08:31:33 CTH

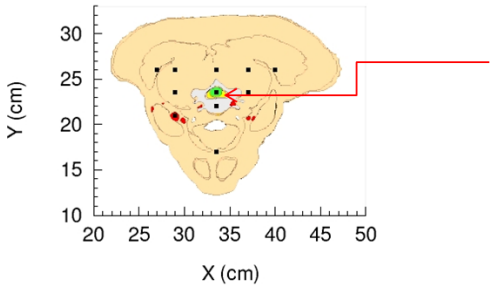

Tracer # 7 (z=49.65)
18(z=49.75)
29(z=49.85)
40(z=49.95)

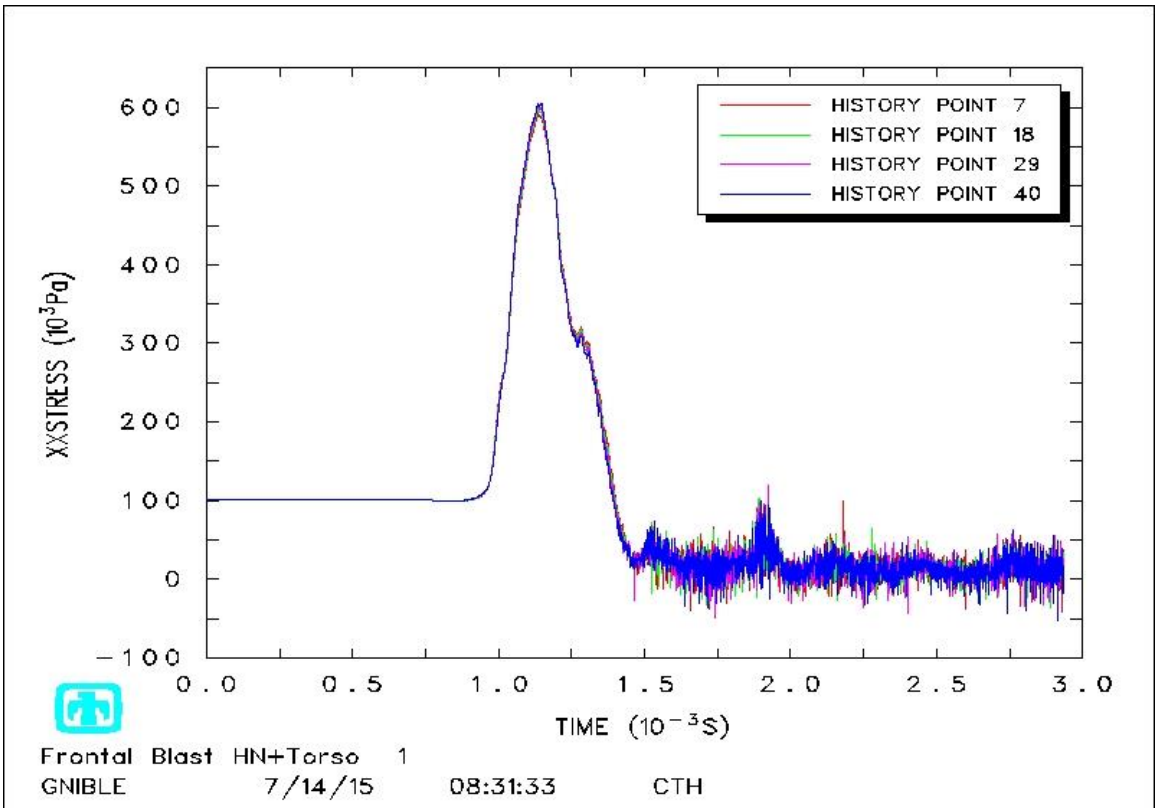
HISTORY POINT 7
HISTORY POINT 18
HISTORY POINT 29
HISTORY POINT 40
XXSTRESS (10³Pa)
600
500
400
300
200
100
0
−100
0.0
0.5
1.0
1.5
2.0
2.5
3.0
TIME (10⁻³S)
Frontal Blast HN+Torso 1
GNIBLE 7/14/15 08:31:33 CTH

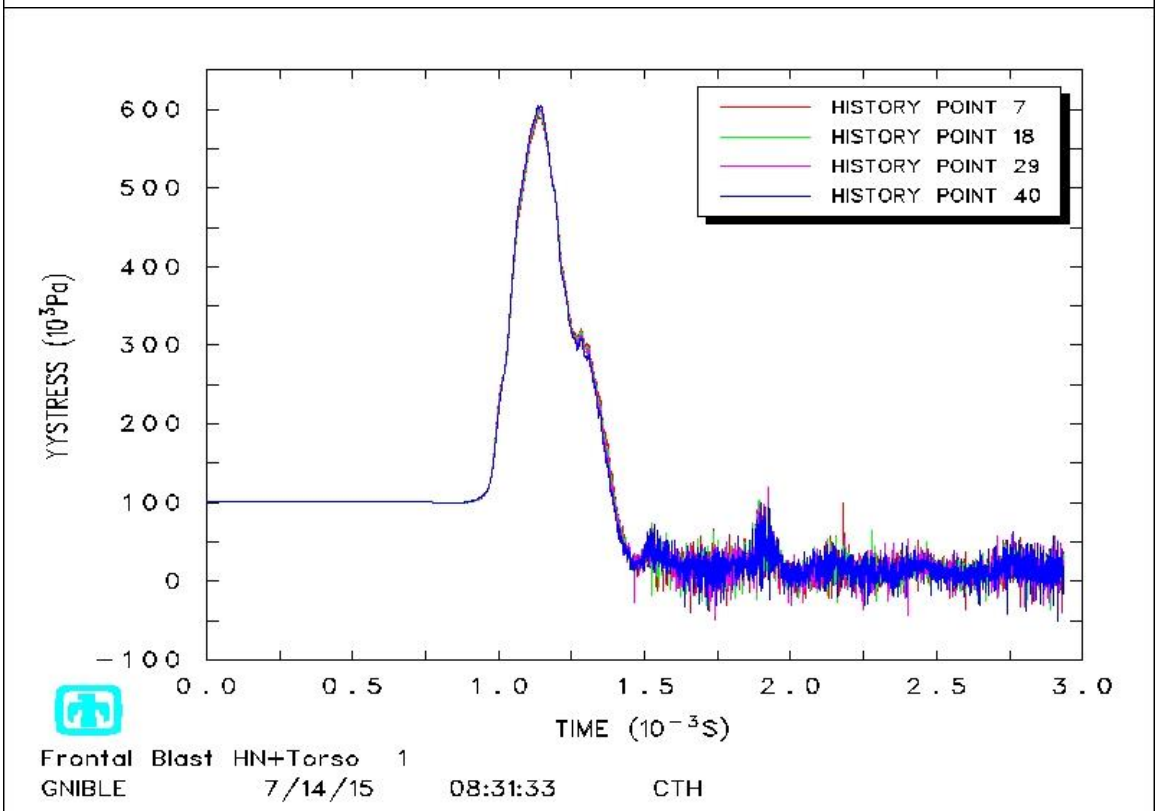
HISTORY POINT 7
HISTORY POINT 18
HISTORY POINT 29
HISTORY POINT 40
YYSTRESS (10³Pa)
600
500
400
300
200
100
0
−100
0.0
0.5
1.0
1.5
2.0
2.5
3.0
TIME (10⁻³S)
Frontal Blast HN+Torso 1
GNIBLE 7/14/15 08:31:33 CTH

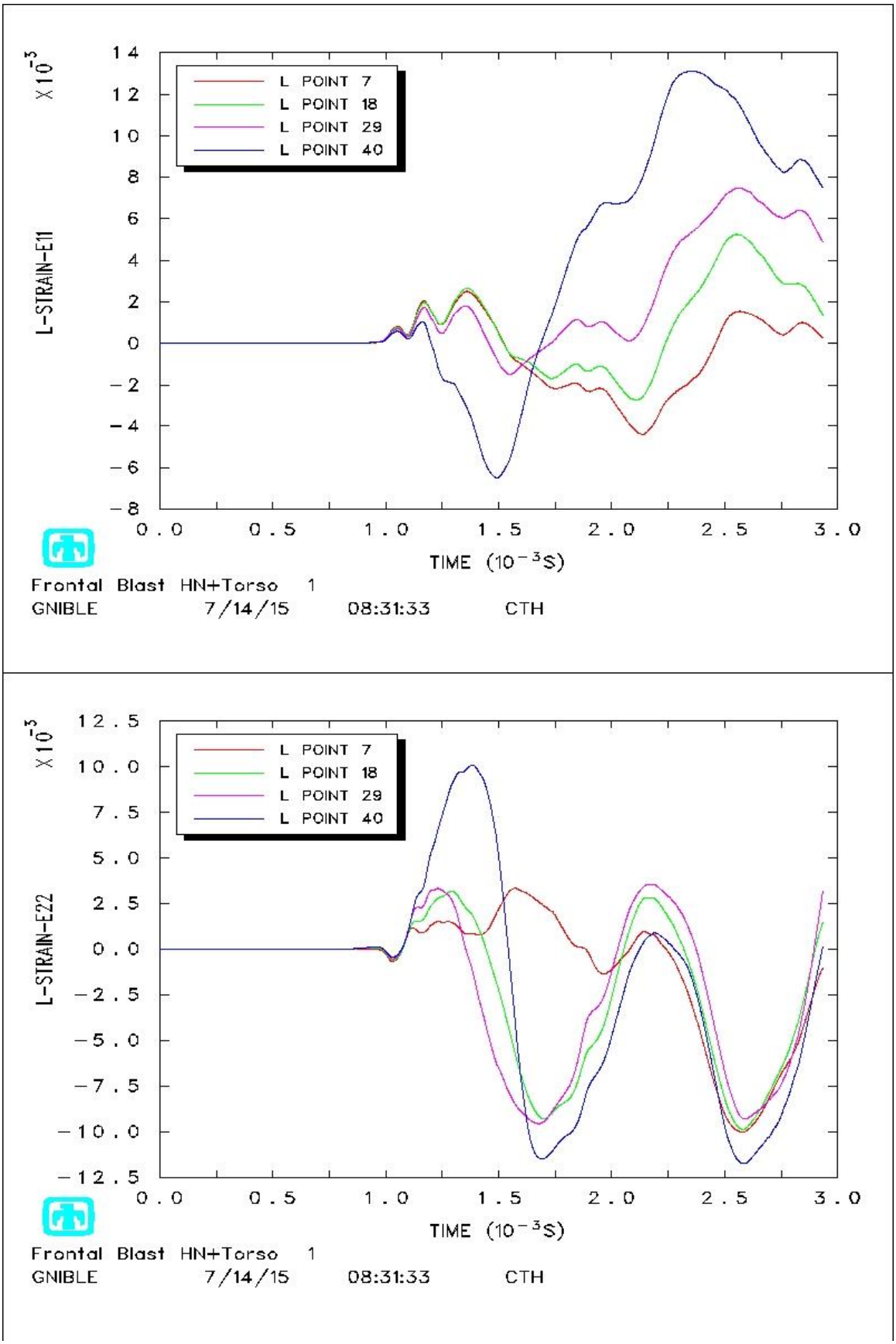
X10-3
L-STRAIN-E11
L POINT 7
L POINT 18
L POINT 29
L POINT 40
14
12
10
8
6
4
2
0
-2
-4
-6
-8
0.0
0.5
1.0
1.5
2.0
2.5
3.0
TIME (10-3S)
Frontal Blast HN+Torso 1
GNIBLE 7/14/15 08:31:33 CTH
X10-3
L-STRAIN-E22
L POINT 7
L POINT 18
L POINT 29
L POINT 40
12.5
10.0
7.5
5.0
2.5
0.0
-2.5
-5.0
-7.5
-10.0
-12.5
0.0
0.5
1.0
1.5
2.0
2.5
3.0
TIME (10-3S)
Frontal Blast HN+Torso 1
GNIBLE 7/14/15 08:31:33 CTH

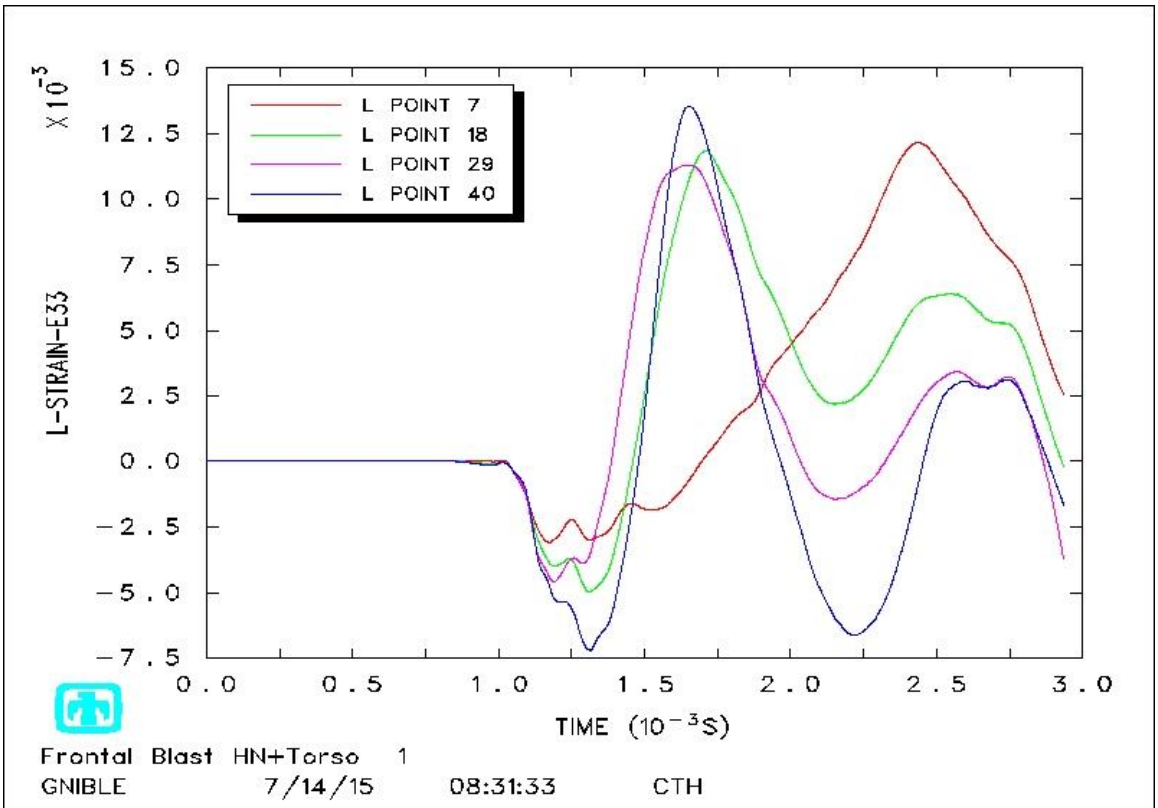
X10^-3
L-STRAIN-E33
15.0
12.5
10.0
7.5
5.0
2.5
0.0
-2.5
-5.0
-7.5
L POINT 7
L POINT 18
L POINT 29
L POINT 40
0.0
0.5
1.0
1.5
2.0
2.5
3.0
TIME (10^-3S)
Frontal Blast HN+Torso 1
GNIBLE 7/14/15 08:31:33 CTH

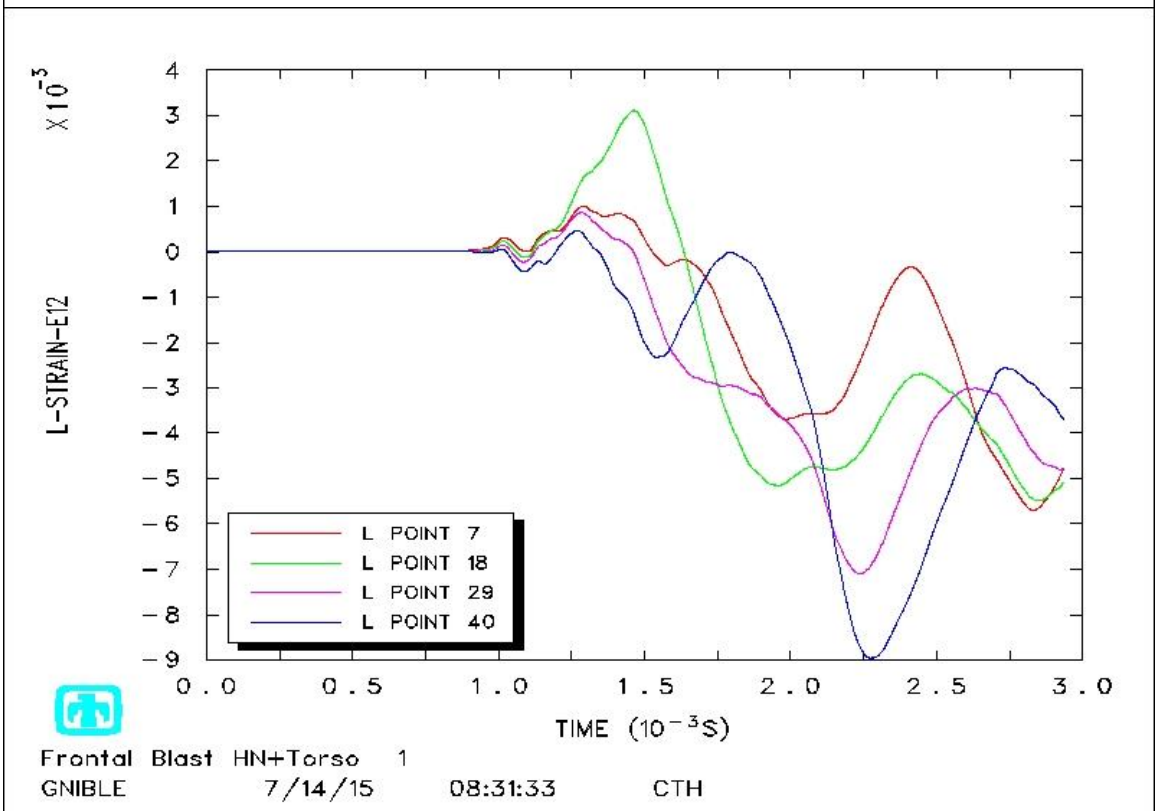
X10^-3
L-STRAIN-E12
4
3
2
1
0
-1
-2
-3
-4
-5
-6
-7
-8
-9
L POINT 7
L POINT 18
L POINT 29
L POINT 40
0.0
0.5
1.0
1.5
2.0
2.5
3.0
TIME (10^-3S)
Frontal Blast HN+Torso 1
GNIBLE 7/14/15 08:31:33 CTH

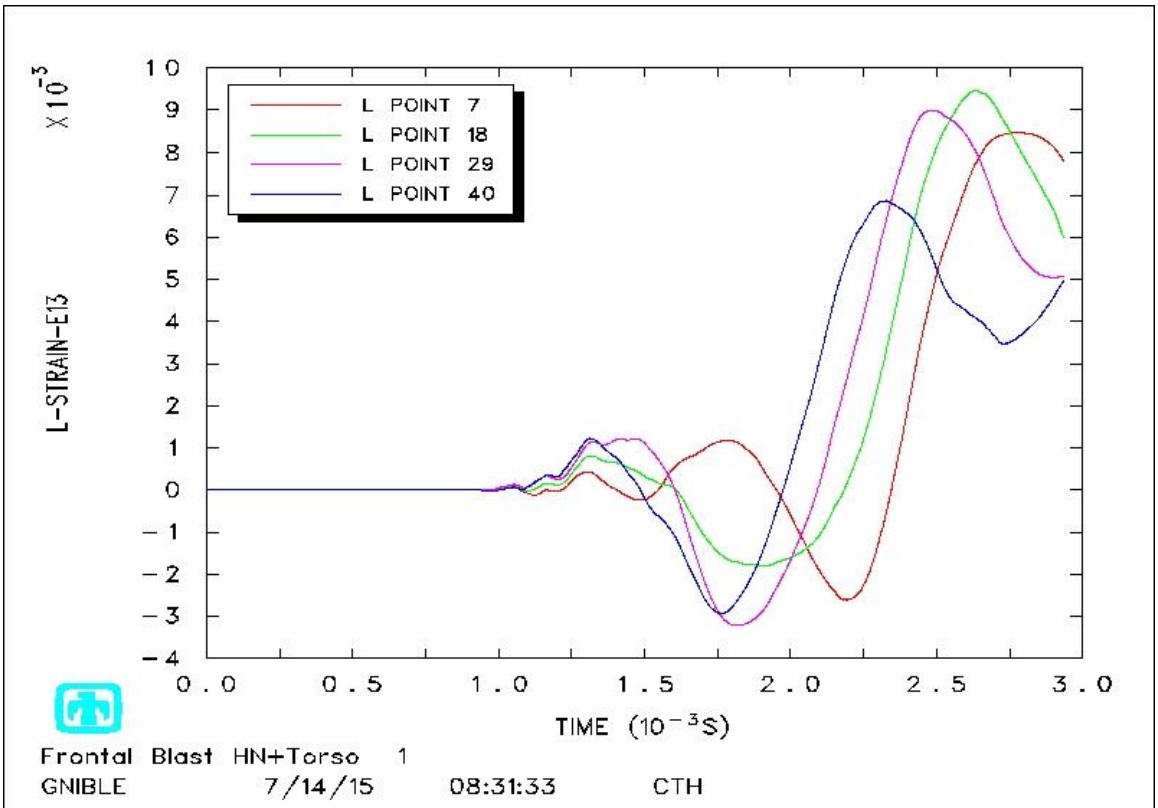
X10^-3
L-STRAIN-E13
L POINT 7
L POINT 18
L POINT 29
L POINT 40
10
9
8
7
6
5
4
3
2
1
0
-1
-2
-3
-4
0.0
0.5
1.0
1.5
2.0
2.5
3.0
TIME (10^-3S)
Frontal Blast HN+Torso 1
GNIBLE 7/14/15 08:31:33 CTH

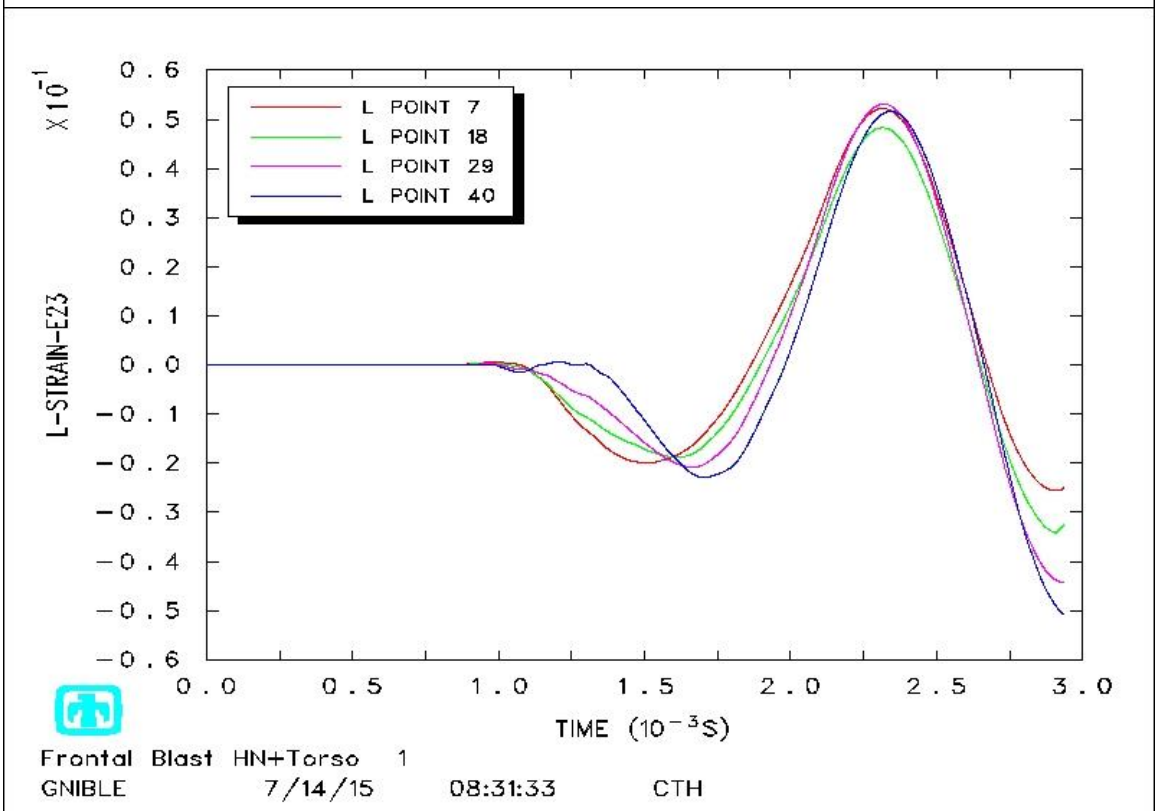
X10^-1
L-STRAIN-E23
L POINT 7
L POINT 18
L POINT 29
L POINT 40
0.6
0.5
0.4
0.3
0.2
0.1
0.0
-0.1
-0.2
-0.3
-0.4
-0.5
-0.6
0.0
0.5
1.0
1.5
2.0
2.5
3.0
TIME (10^-3S)
Frontal Blast HN+Torso 1
GNIBLE 7/14/15 08:31:33 CTH

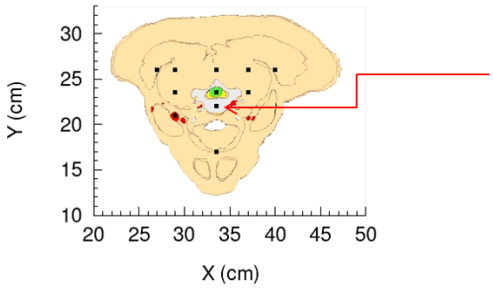

Tracer # 8 (z=49.65)
19(z=49.75)
30(z=49.85)
41(z=49.95)

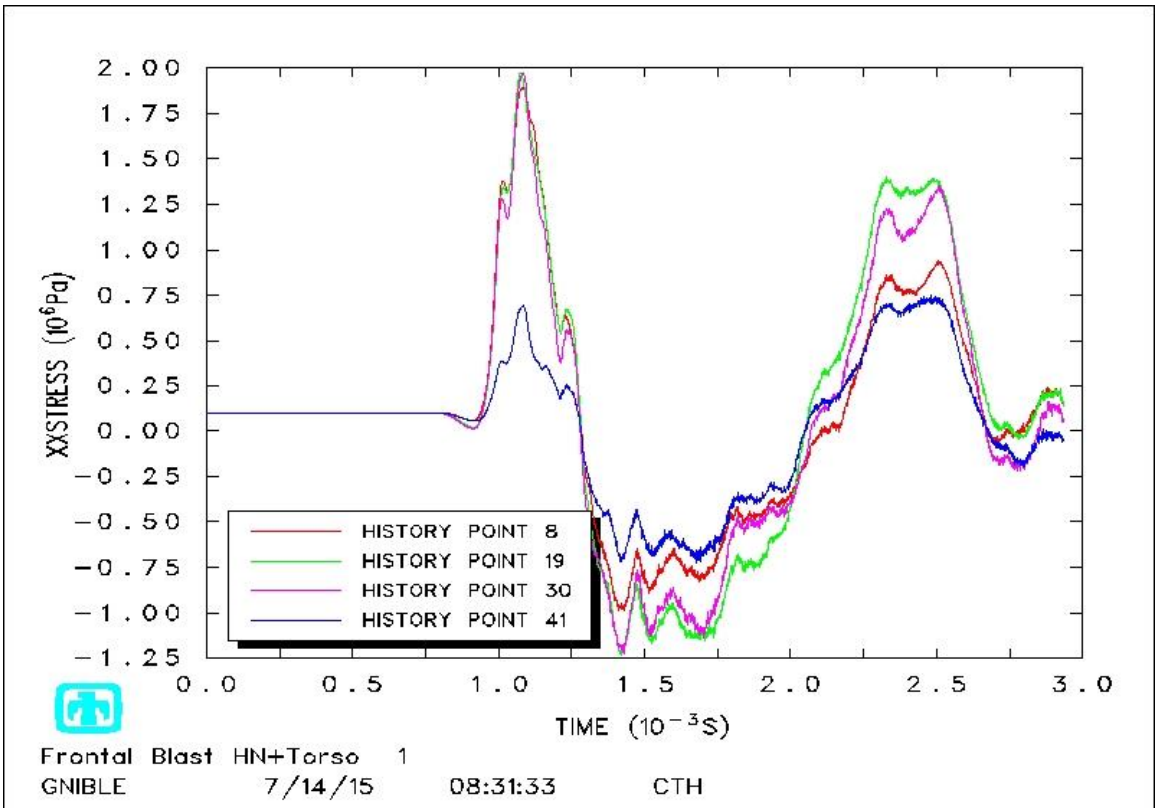
2.00
1.75
1.50
1.25
1.00
0.75
0.50
0.25
0.00
−0.25
−0.50
−0.75
−1.00
−1.25
XXSTRESS (10⁶Pa)
0.0
0.5
1.0
1.5
2.0
2.5
3.0
TIME (10⁻³S)
HISTORY POINT 8
HISTORY POINT 19
HISTORY POINT 30
HISTORY POINT 41
Frontal Blast HN+Torso 1
GNIBLE 7/14/15 08:31:33 CTH

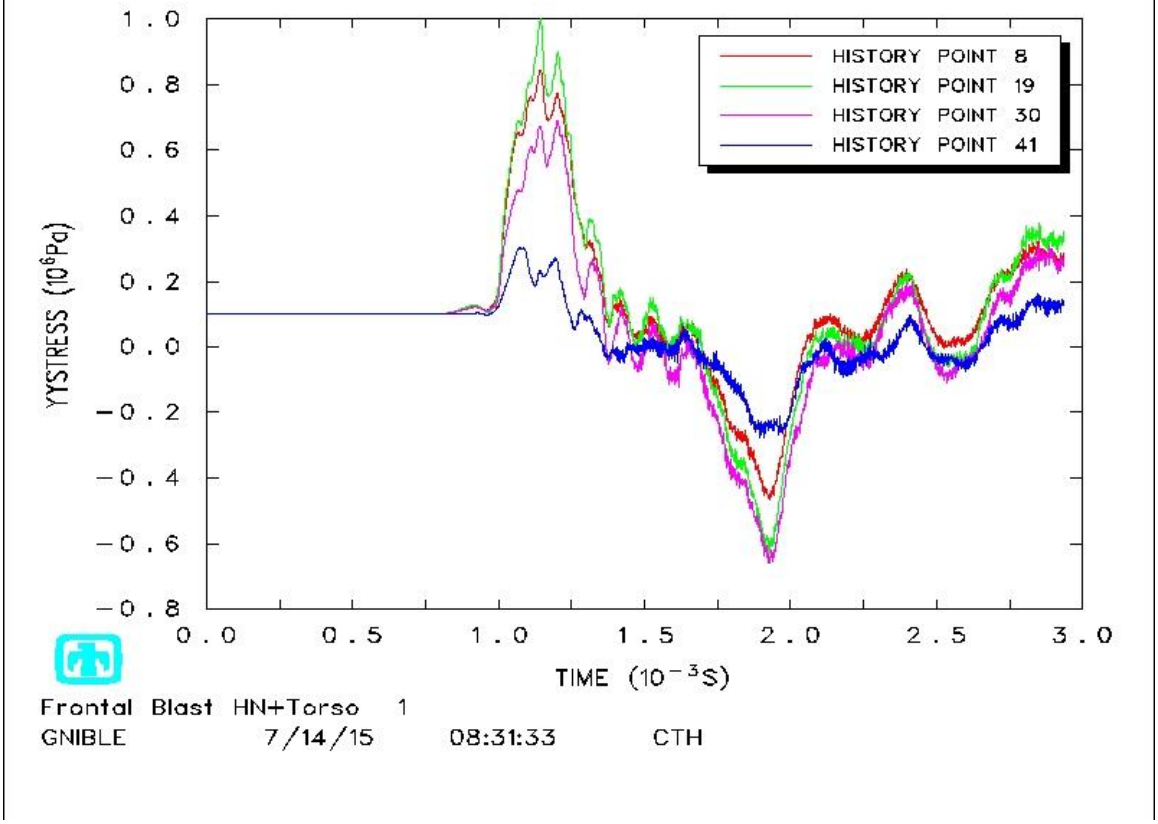
1.0
0.8
0.6
0.4
0.2
0.0
−0.2
−0.4
−0.6
−0.8
YYSTRESS (10⁶Pa)
0.0
0.5
1.0
1.5
2.0
2.5
3.0
TIME (10⁻³S)
HISTORY POINT 8
HISTORY POINT 19
HISTORY POINT 30
HISTORY POINT 41
Frontal Blast HN+Torso 1
GNIBLE 7/14/15 08:31:33 CTH

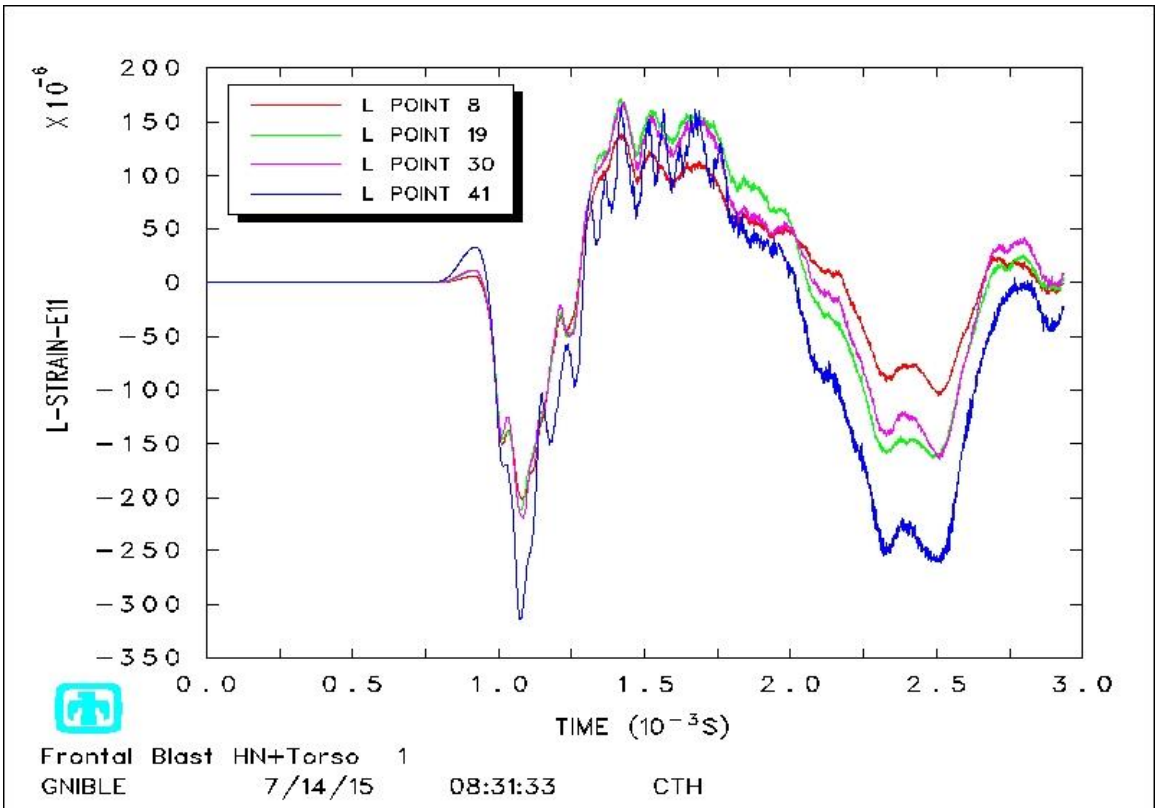
X10⁻⁶
L-STRAIN-E11
L POINT 8
L POINT 19
L POINT 30
L POINT 41
200
150
100
50
0
−50
−100
−150
−200
−250
−300
−350
0.0
0.5
1.0
1.5
2.0
2.5
3.0
TIME (10⁻³S)
Frontal Blast HN+Torso 1
GNIBLE 7/14/15 08:31:33 CTH

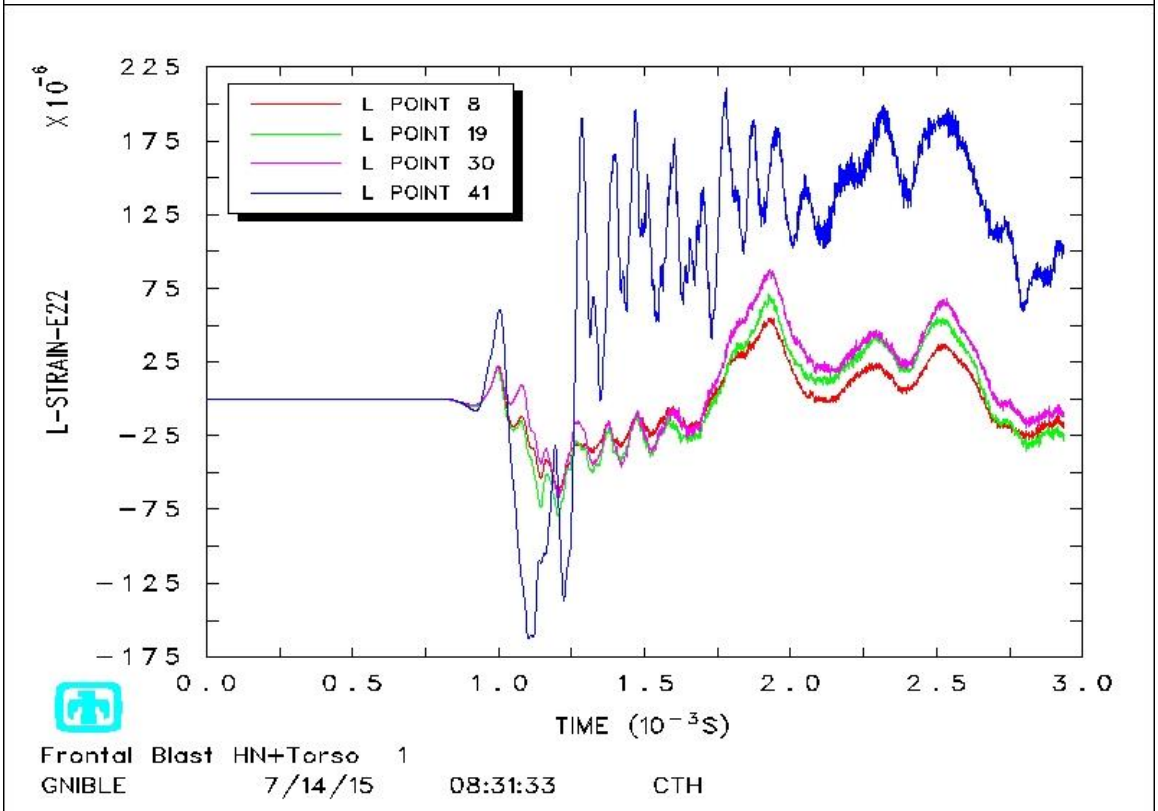
X10⁻⁶
L-STRAIN-E22
L POINT 8
L POINT 19
L POINT 30
L POINT 41
225
175
125
75
25
−25
−75
−125
−175
0.0
0.5
1.0
1.5
2.0
2.5
3.0
TIME (10⁻³S)
Frontal Blast HN+Torso 1
GNIBLE 7/14/15 08:31:33 CTH

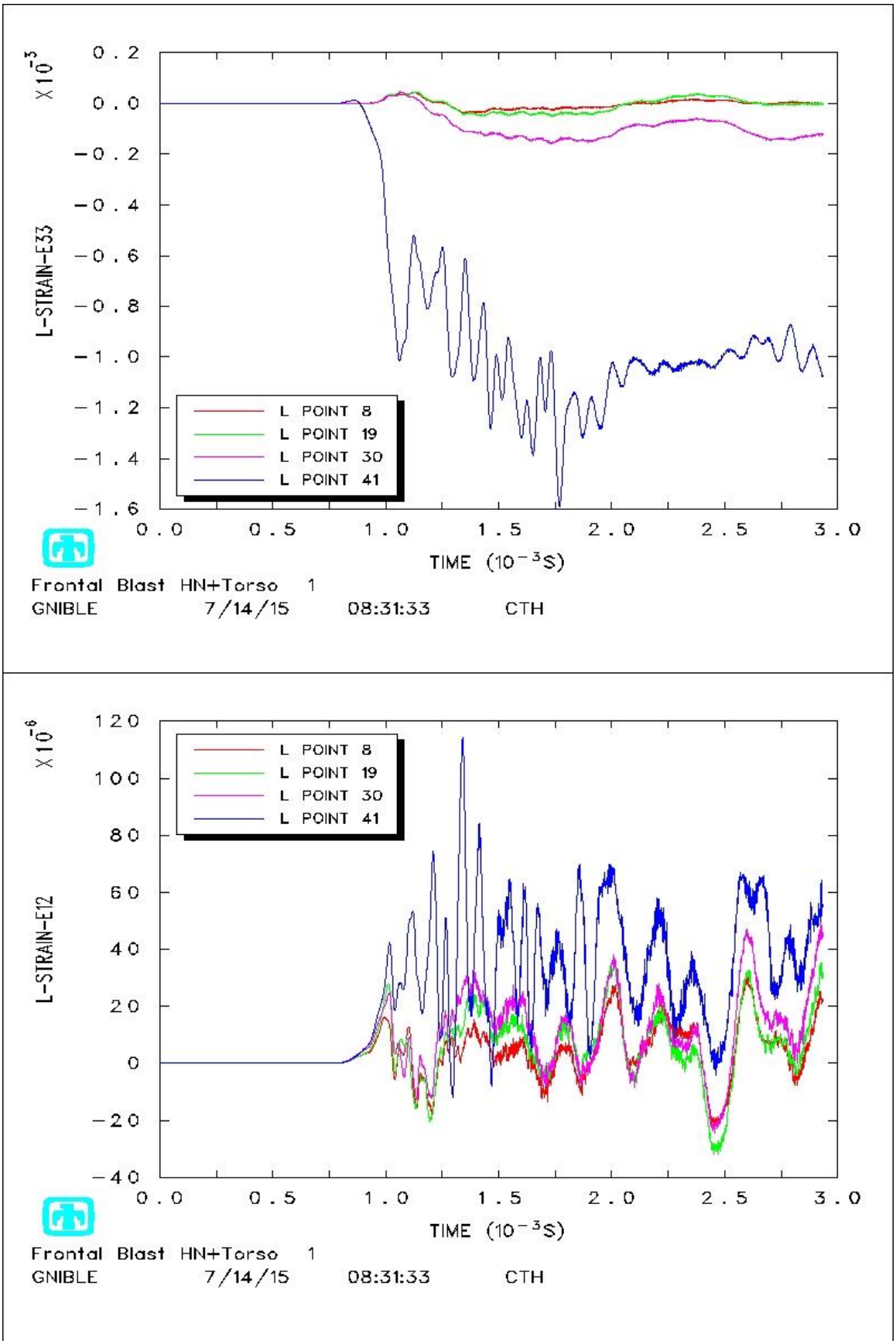
X10^-3
0.2
0.0
-0.2
-0.4
-0.6
-0.8
-1.0
-1.2
-1.4
-1.6
L-STRAIN-E33
L POINT 8
L POINT 19
L POINT 30
L POINT 41
0.0
0.5
1.0
1.5
2.0
2.5
3.0
TIME (10^-3S)
Frontal Blast HN+Torso 1
GNIBLE 7/14/15 08:31:33 CTH
X10^-6
120
100
80
60
40
20
0
-20
-40
L-STRAIN-E12
L POINT 8
L POINT 19
L POINT 30
L POINT 41
0.0
0.5
1.0
1.5
2.0
2.5
3.0
TIME (10^-3S)
Frontal Blast HN+Torso 1
GNIBLE 7/14/15 08:31:33 CTH

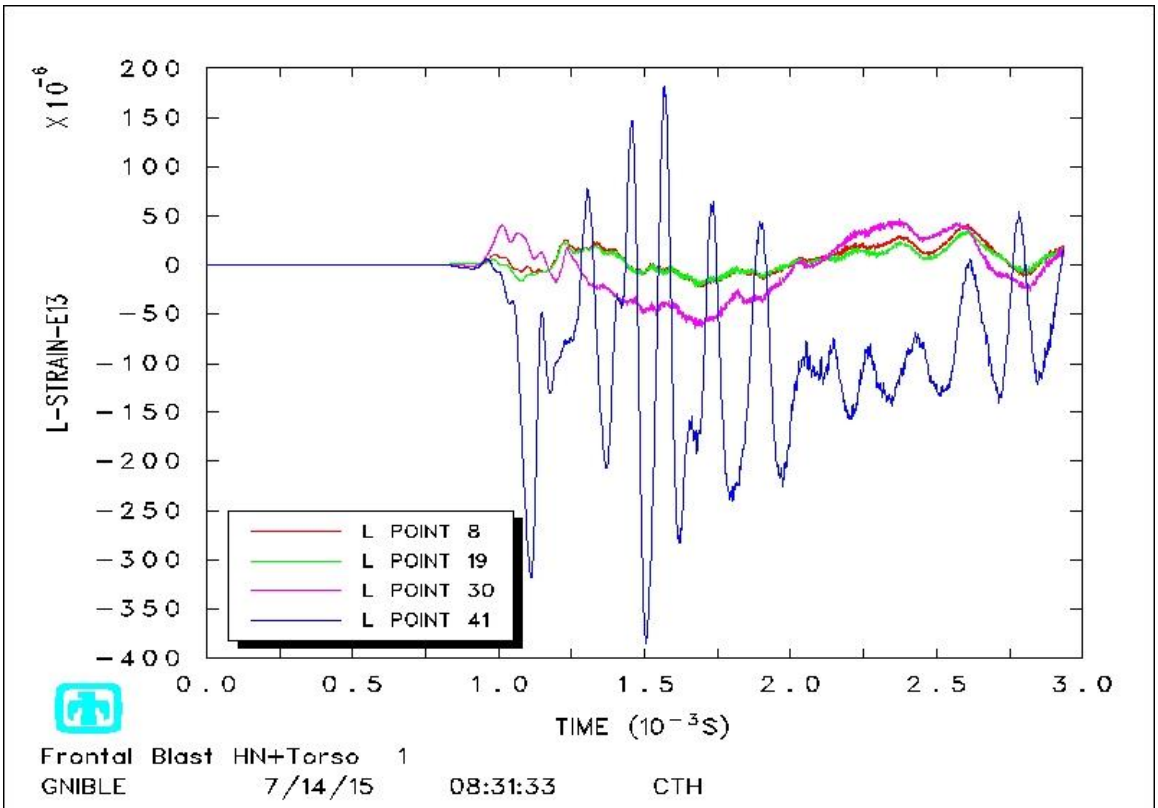
X10^-6
L-STRAIN-E13
200
150
100
50
0
-50
-100
-150
-200
-250
-300
-350
-400
0.0
0.5
1.0
1.5
2.0
2.5
3.0
TIME (10^-3S)
L POINT 8
L POINT 19
L POINT 30
L POINT 41
Frontal Blast HN+Torso 1
GNIBLE 7/14/15 08:31:33 CTH

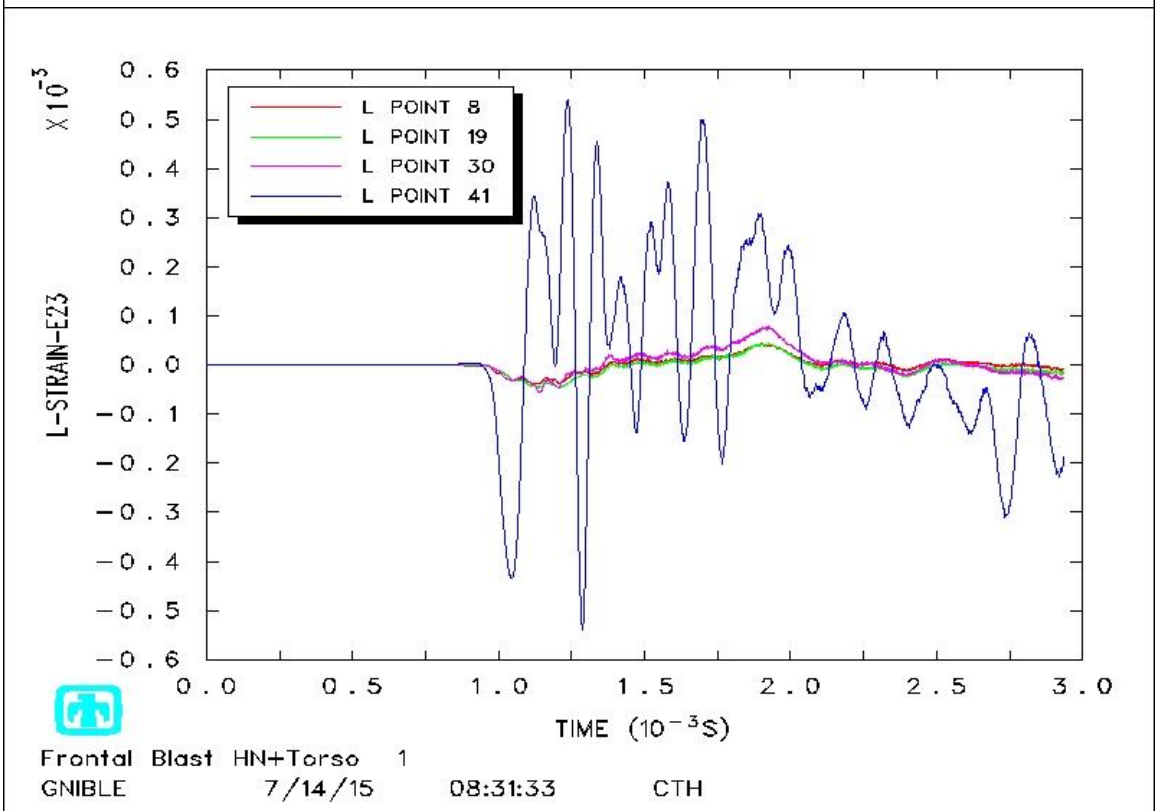
X10^-3
L-STRAIN-E23
0.6
0.5
0.4
0.3
0.2
0.1
0.0
-0.1
-0.2
-0.3
-0.4
-0.5
-0.6
0.0
0.5
1.0
1.5
2.0
2.5
3.0
TIME (10^-3S)
L POINT 8
L POINT 19
L POINT 30
L POINT 41
Frontal Blast HN+Torso 1
GNIBLE 7/14/15 08:31:33 CTH

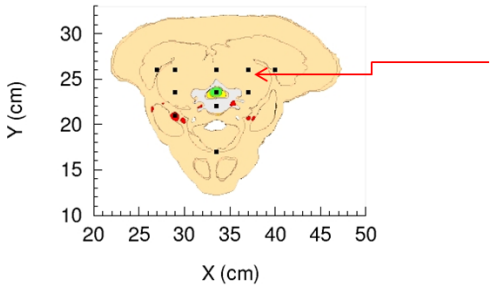

Tracer # 10 (z=49.65)
21(z=49.75)
32(z=49.85)
43(z=49.95)

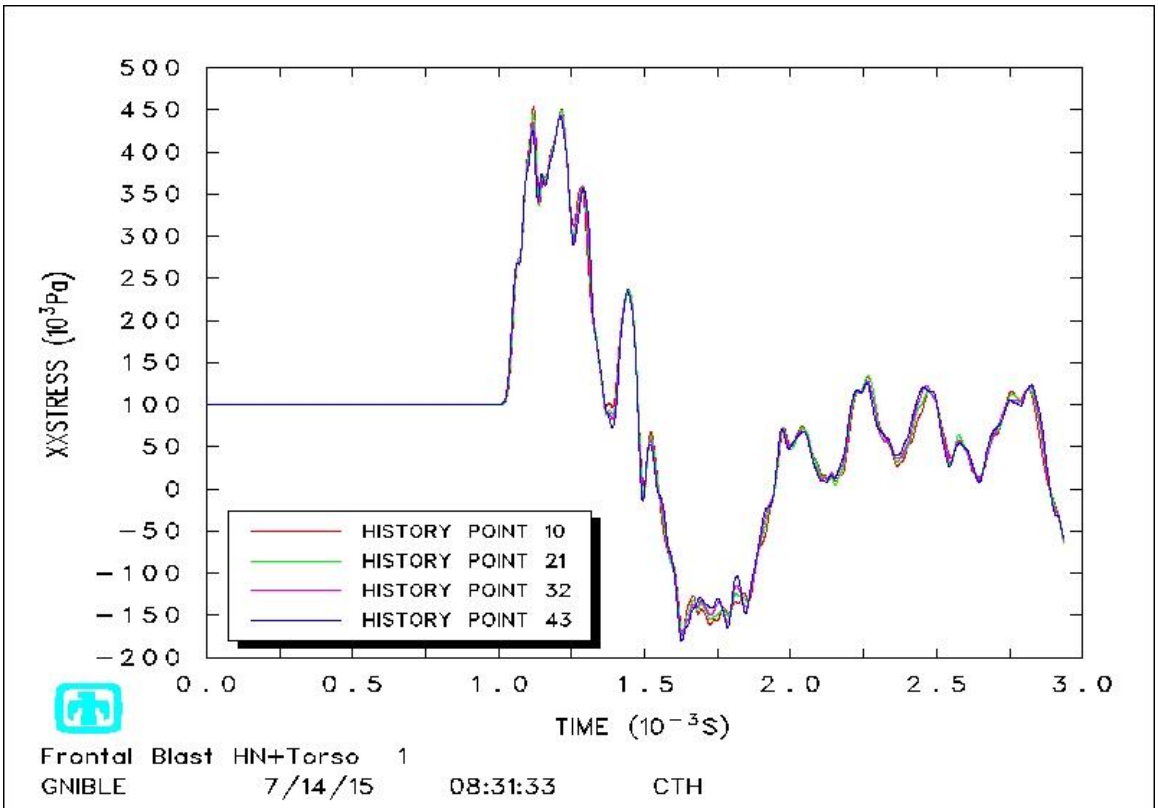
500
450
400
350
300
250
200
150
100
50
0
−50
−100
−150
−200
XXSTRESS (10³Pa)
HISTORY POINT 10
HISTORY POINT 21
HISTORY POINT 32
HISTORY POINT 43
0.0
0.5
1.0
1.5
2.0
2.5
3.0
TIME (10⁻³S)
Frontal Blast HN+Torso 1
GNIBLE 7/14/15 08:31:33 CTH

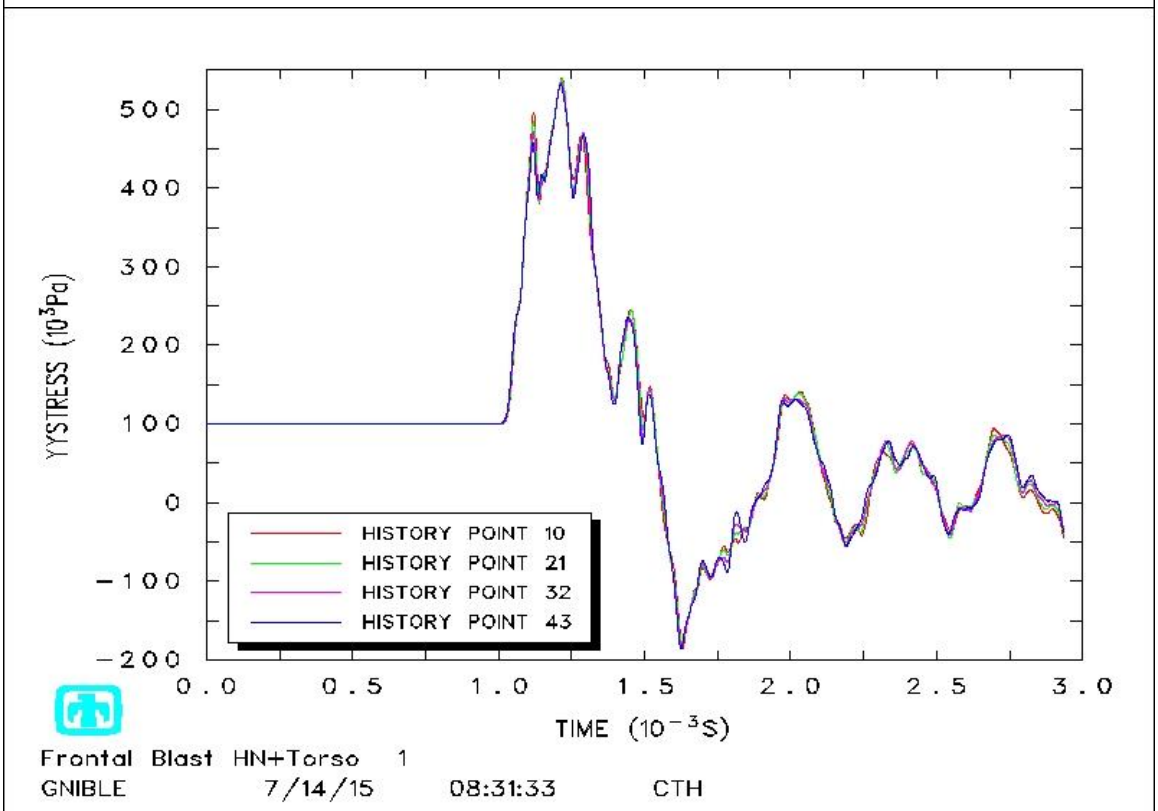
500
400
300
200
100
0
−100
−200
YYSTRESS (10³Pa)
HISTORY POINT 10
HISTORY POINT 21
HISTORY POINT 32
HISTORY POINT 43
0.0
0.5
1.0
1.5
2.0
2.5
3.0
TIME (10⁻³S)
Frontal Blast HN+Torso 1
GNIBLE 7/14/15 08:31:33 CTH

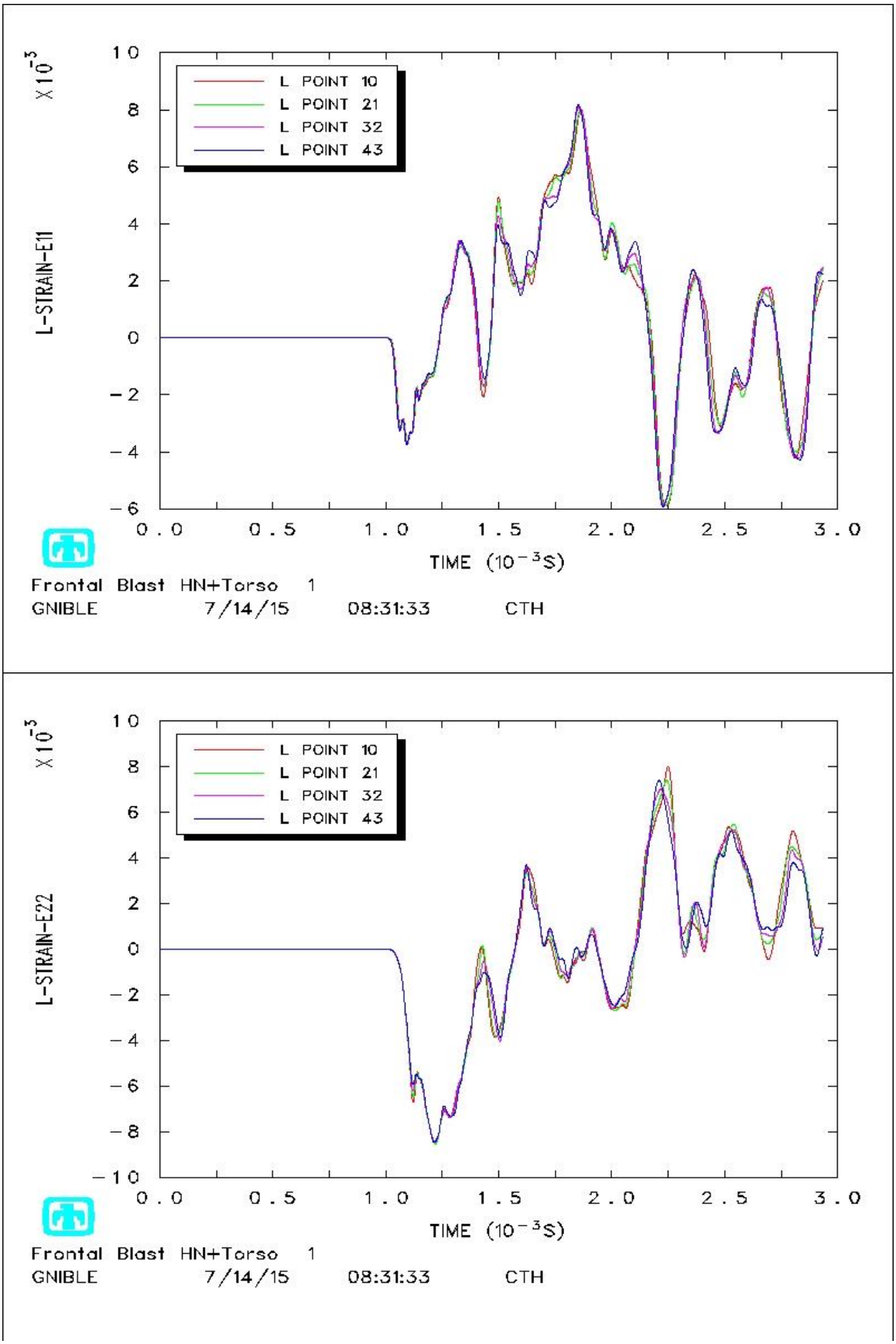
X 10^-3
L-STRAIN-E11
L POINT 10
L POINT 21
L POINT 32
L POINT 43
10
8
6
4
2
0
-2
-4
-6
0.0
0.5
1.0
1.5
2.0
2.5
3.0
TIME (10^-3S)
Frontal Blast HN+Torso 1
GNIBLE 7/14/15 08:31:33 CTH
X 10^-3
L-STRAIN-E22
L POINT 10
L POINT 21
L POINT 32
L POINT 43
10
8
6
4
2
0
-2
-4
-6
-8
-10
0.0
0.5
1.0
1.5
2.0
2.5
3.0
TIME (10^-3S)
Frontal Blast HN+Torso 1
GNIBLE 7/14/15 08:31:33 CTH

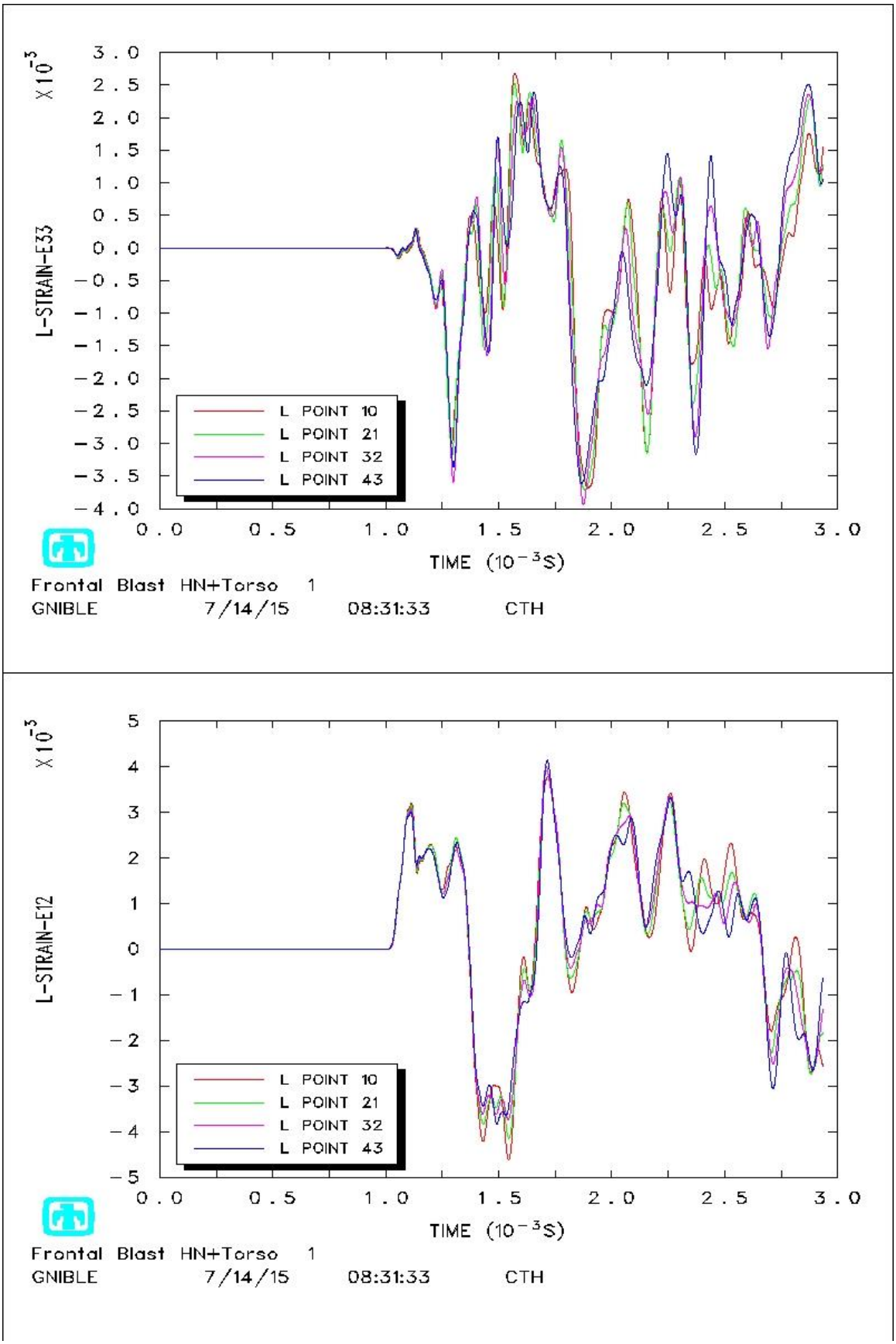
X10^-3
L-STRAIN-E33
3.0
2.5
2.0
1.5
1.0
0.5
0.0
-0.5
-1.0
-1.5
-2.0
-2.5
-3.0
-3.5
-4.0
L POINT 10
L POINT 21
L POINT 32
L POINT 43
0.0
0.5
1.0
1.5
2.0
2.5
3.0
TIME (10^-3S)
Frontal Blast HN+Torso 1
GNIBLE 7/14/15 08:31:33 CTH
X10^-3
L-STRAIN-E12
5
4
3
2
1
0
-1
-2
-3
-4
-5
L POINT 10
L POINT 21
L POINT 32
L POINT 43
0.0
0.5
1.0
1.5
2.0
2.5
3.0
TIME (10^-3S)
Frontal Blast HN+Torso 1
GNIBLE 7/14/15 08:31:33 CTH

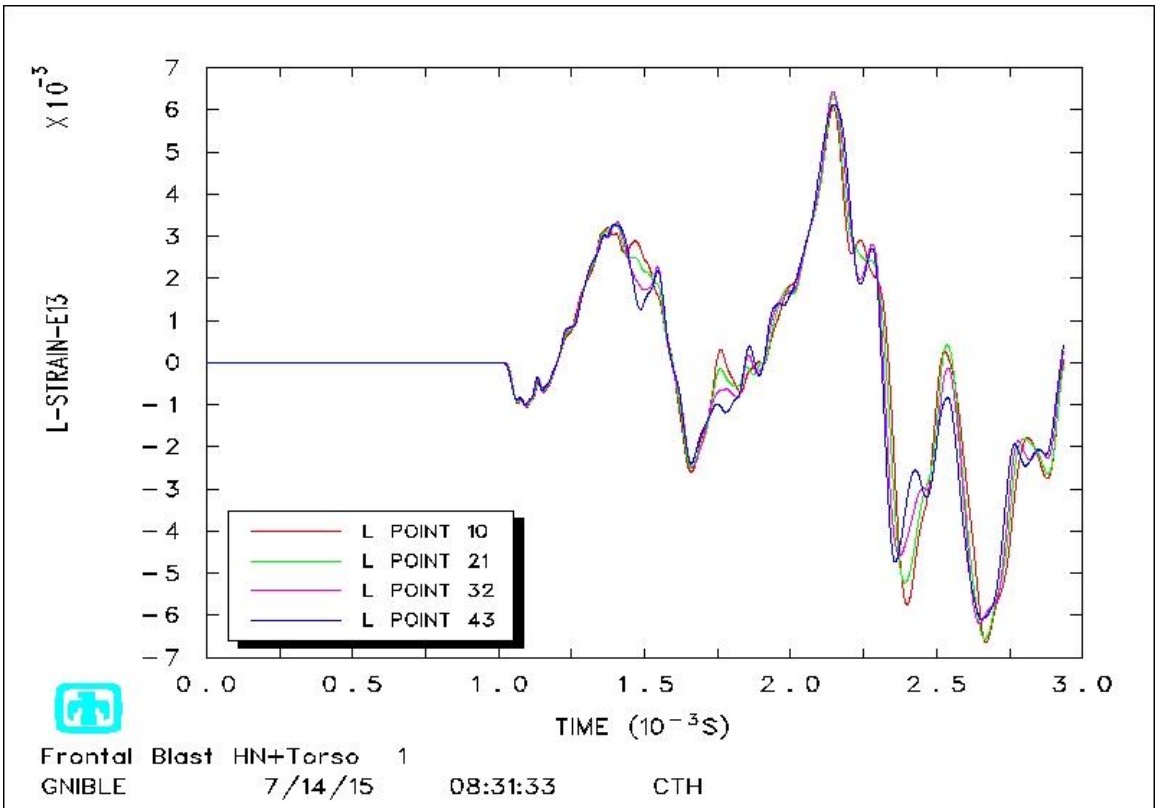
X10-3
L-STRAIN-E13
7
6
5
4
3
2
1
0
-1
-2
-3
-4
-5
-6
-7
L POINT 10
L POINT 21
L POINT 32
L POINT 43
0.0
0.5
1.0
1.5
2.0
2.5
3.0
TIME (10-3S)
Frontal Blast HN+Torso 1
GNIBLE 7/14/15 08:31:33 CTH

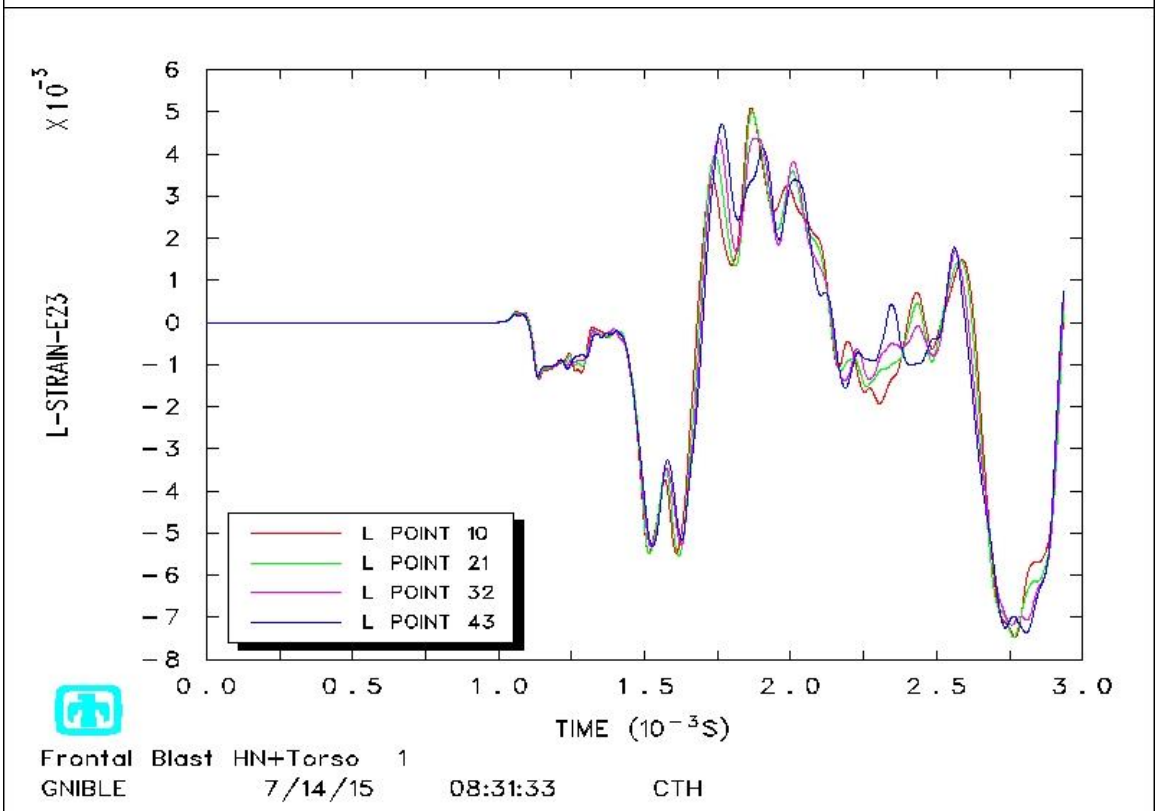
X10-3
L-STRAIN-E23
6
5
4
3
2
1
0
-1
-2
-3
-4
-5
-6
-7
-8
L POINT 10
L POINT 21
L POINT 32
L POINT 43
0.0
0.5
1.0
1.5
2.0
2.5
3.0
TIME (10-3S)
Frontal Blast HN+Torso 1
GNIBLE 7/14/15 08:31:33 CTH

8 APPENDIX B

Brief overview of brain anatomy to assist the reader in understanding statements made at the end of section 4.4.

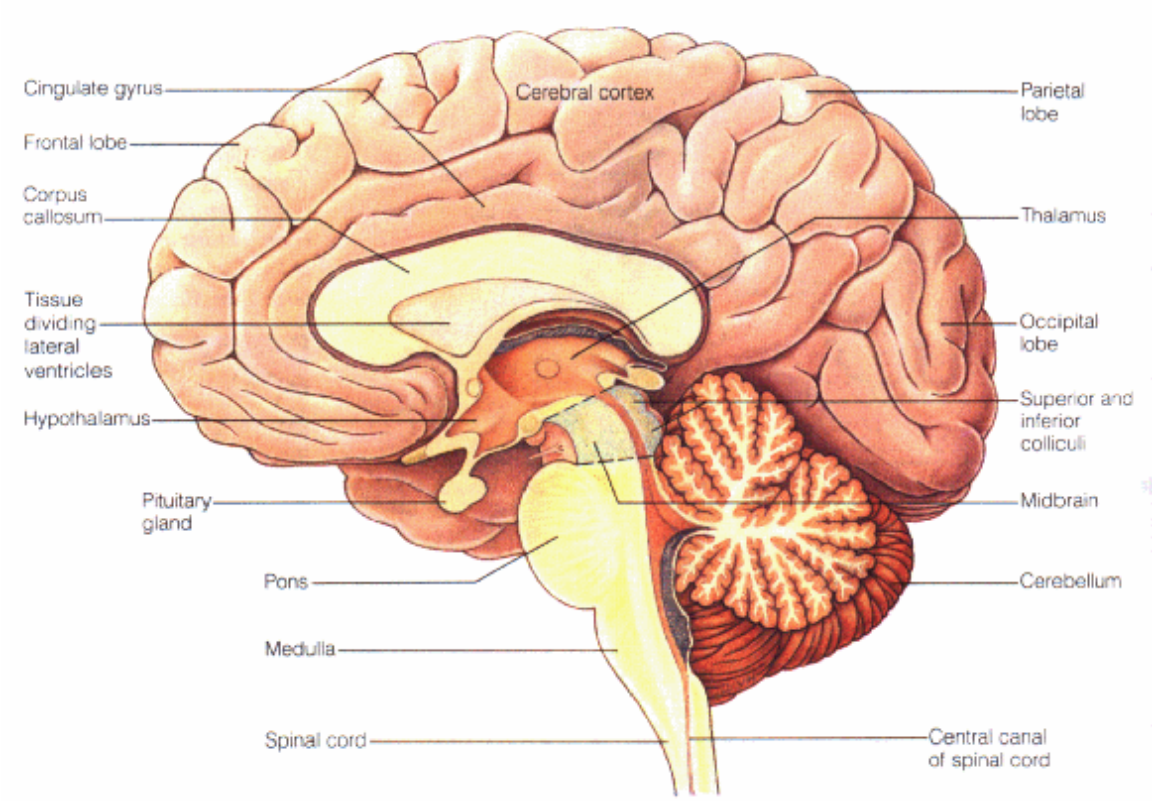

Figure 41: Mid-Sagittal section of the brain [44]

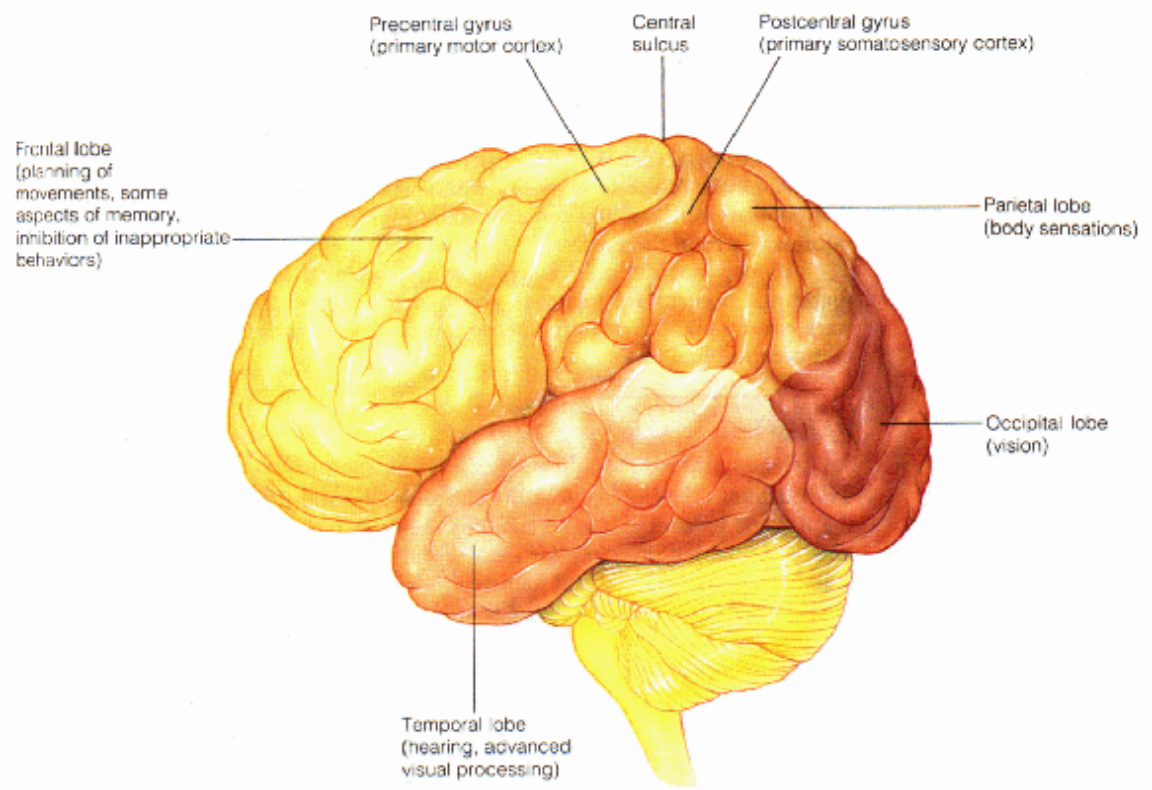

Figure 42: Functional subdivision of the cortex [44]

9 References

[1] Moore, D. F., Jérusalem, A., Nyein, M., Noels, L., Jaffee, M. S., and Radovitzky, R. A., 2009, "Computational biology — modeling of primary blast effects on the central nervous system," NeuroImage, **47**, **Supplement 2**, pp. T10–T20.

[2] Chafi, M. S., Karami, G., and Ziejewski, M., 201AD, "Biomechanical Assessment of Brain Dynamic Responses Due to Blast Pressure Waves," Ann. Biomed. Eng., **38**(2), pp. 490–504.

[3] Rezaei, A., Salimi Jazi, M., and Karami, G., 2014, "Computational modeling of human head under blast in confined and open spaces: primary blast injury," Int. J. Numer. Methods Biomed. Eng., **30**, pp. 69–82.

[4] Tan, L. B., Chew, F. S., Tse, K. M., Tan, V. B. C., and Lee, H. P., 2014, "Impact of complex blast waves on the human head: a computational study," Int. J. Numer. Methods Biomed. Eng., **30**, pp. 1476–1505.

[5] Cotton, R. T., Pearce, C. W., Young, P. G., Kota, N., Leung, A. C., Bagchi, A., and Qidwai, S. M., 2015, "Development of a geometrically accurate and adaptable finite element head model for impact simulation: the Naval Research Laboratory-Simpleware Head Model," Comput. Methods Biomech. Biomed. Engin.

[6] Taylor, P. A., and Ford, C. C., 2009, "Simulation of blast-induced early-time intracranial wave physics leading to traumatic brain injury," J. Biomech. Eng., **131**(6), p. 61007.

[7] Taylor, P. A., Cooper, C. F., and Burnett, D. J., 2015, Wound Ballistics Modeling for Blast Loading, Blunt Force Impact, and Projectile Penetration; SAND2015-7909.

[8] Cooper, C. F., and Taylor, P. A., 2015, "Virtual Simulation of Blast, Behind-Armor Blunt Trauma, and Projectile Penetration Leading to Injury of Life-Critical Organs in the Human Torso," ASME 2015 Int. Mech. Eng. Congr. Expo., **3**.

[9] Haniff, S., Taylor, P., Brundage, A., Burnett, D., Cooper, C., Gullerud, A., and Terpsma, R., 2015, "Virtual simulation of the effects of intracranial fluid cavitation in blast-induced traumatic brain injury," Proceedings of the ASME 2015 International Mechanical Engineering Congress & Exposition, ASME, Houston, TX.

[10] Panzer, M. B., Myers, B. S., Capehart, B. P., and Bass, C. R., 2012, "Development of a Finite Element Model for Blast Brain Injury and the Effects of CSF Cavitiation," Ann. Biomed. Eng., **40**(7), pp. 1530–1544.

[11] Goumtcha, A. A., Thoral-Pierre, K., and Roth, S., 2014, "Biomechanical model of the thorax under blast loading: a three dimensional numerical study," Int. J. Numer. Methods Biomed. Eng., **30**, pp. 1667–1678.

[12] Zhou, J., and Tao, G., 2015, "Biomechanical modeling for the response of human thorax to blast waves," Acta Mech. Sin., **31**(4), pp. 589–598.

[13] Shen, W., Niu, Y., Mattrey, R. F., Fournier, A., Corbeil, J., Kono, Y., and Stuhmiller, J., 2008, "Development and Validation of Subject-Specific Finite Element Models for Blunt Trauma Study," J. Biomech. Eng., **130**.

[14] Roberts, J. C., Biermann, P. J., O-Connor, J. V., Ward, E. E., Cain, R. P., Carkhuff, B. G., and Merkle, A. C., 2005, "Modeling nonpenetrating ballistic impact on a human torso," Johns Hopkins APL Tech. Dig., **26**(1), pp. 84–92.

[15] Roberts, J. C., Ward, E. E., Merkle, A. C., and O'Connor, J. V., 2007, "Assessing Behind Armor Blunt Trauma in Accordance With the National Institute of Justice Standard for Personal Body Armor Protection Using Finite Element Modeling," J. TRAUMA Inj. Infect. Crit. Care, **62**(5), pp. 1127–1133.
[16] Roberts, J. C., Merkle, A. C., Biermann, P. J., Ward, E. E., Carkhuff, B. G., Cain, R. P., and O-Connor, J. V., 2007, "Computational and experimental models of the human torso for nonpenetrating ballistic impact," J. Biomech., **40**, pp. 125–136.
[17] Shen, W., Niu, Y., Bykanova, L., Laurence, P., and Link, N., 2010, "Characterizing the Interaction Among Bullet, Body Armor, and Human and Surrogate Targets," J. Biomech. Eng., **132**(12).
[18] Wen, Y., Xu, C., Wang, S., and Batra, R. C., 2015, "Analysis of behind the armor ballistic trauma," J. Mech. Behav. Biomed. Mater., **45**, pp. 11–21.
[19] Bass, C. R., Salzar, R. S., Lucus, S. R., Davis, M., Donnellan, L., Folk, B., Sanderson, E., and Waclawik, S., 2006, "Injury Risk in Behind Armor Blunt Thoracic Trauma," Int. J. Occup. Saf. Ergon., **12**(4), pp. 429–442.
[20] Gryth, D., Rocksen, D., Persson, J., Arborelius, U. P., Drobin, D., Bursell, J., Olsson, L.-G., and Kjellstrom, T. B., 2007, "Sever Lung Contusion and Death after High-Velocity Behind Armor Blunt Trauma: Relation to Protection Level," Mil. Med., **172**.
[21] Sonden, A., Rocksen, D., Riddez, L., Davidsson, J., Persson, J., Gryth, D., Bursell, J., and Arborelius, U. P., 2009, "Trauma Attenuating Backing Improves Protection Against Behind Armor Blunt Trauma," J. TRAUMA Inj. Infect. Crit. Care, **67**(6).
[22] Kunz, S., Arborelius, U. P., Gryth, D., Sonden, A., Gustavsson, J., Wangyal, T., Svensson, L., and Rocksen, D., 2011, "Cardiac Changes After Simulated Behind Armor Blunt Trauma or Impact of Nonlethal Kinetic Projectile Ammunition," J. TRAUMA Inj. Infect. Crit. Care, **71**(5), pp. 1134–1143.
[23] Gayzik, F. S., Moreno, D. P., Danelson, K. A., McNally, C., Klinich, K. D., and Stitzel, J. D., 2012, "External Landmark, Body Surface, and Volume Data of a Mid-Sized Male in Seated and Standing Postures," Ann. Biomed. Eng., **40**(9), pp. 2019–2032.
[24] Gayzik, F. S., Moreno, D. P., Geer, C. P., Wuertzer, S. D., Martin, R. S., and Stitzel, J. D., 2011, "Development of a Full Body Cad Dataset for Computational Modeling: A Multi-modality Approach," Ann. Biomed. Eng., **39**(10), pp. 2568–2583.
[25] Shigeta, K., Kitagawa, Y., and Yasuki, T., 2009, "Development of Next Generation Human FE Model Capable of Organ Injury Prediction," Proc. Int. Tech. Conf. Enhanc. Saf. Veh.
[26] 2007, "The National Library of Medicine's visible human project" [Online]. Available: http://www.nlm.nih.gov/research/visible/visible_human.html. [Accessed: 30-Jan-2013].
[27] Ludwigsen, J. S., 2013, "Personal Communication."
[28] Lee, M. K., Sakai, O., and Spiegel, J., 2010, "CT measurement of the frontal sinus-Gender differences and implications for frontal cranioplasty," J. Craniomaxillofac. Surg., **38**, pp. 494–500.
[29] Hertel, E. S., and Kerley, G. I., 1998, CTH reference manual: The equation of state package, Sandia National Laboratories Report SAND98-0947, Albuquerque, NM.

[30] Brundage, A. L., 2013, "Implementation of Tillotson equation of state for hypervelocity impact of metals, geologic materials, and liquids," Procedia Eng., **58**, pp. 461–470.
[31] Marsh, S. P., 1980, LASL Shock Hugoniot Data, University of California Press.
[32] Tillotson, J. H., 1962, Metallic equations of state for hypervelocity impact, San Diego, CA.
[33] Cushing, V. J., 1991, Shock induced cavitation, Defense Nuclear Agency Report DNA-TR-89-289.
[34] Siedler, G., and Peters, H., 1986, "Physical properties (general) of sea water," LANDOLT-BORNSTEIN: Numerical data and functional relationships in science and technology, Springer, Berlin, pp. 233–264.
[35] Palaniappan, L., and Velusamy, V., 2004, "Ultrasonic study of human cerebrospinal fluid," Indian J. Pure Appl. Sci., **42**, pp. 591–594.
[36] Nagoya, H., Obara, T., and Takayama, K., 1995, "Underwater shock wave propagation and focusing in inhomogeneous media," Shock Waves in Condensed Matter and Heterogeneous Media, Springer, pp. 439–444.
[37] Williams, J. C., Woodward, J. F., Stonechill, M. A., Evan, A. P., and McAteer, J. A., 1999, "Cell damage by lithotripter shock waves at high pressure to preclude cavitation," Ultrasound Med. Biol., **25**(9), pp. 1445–1449.
[38] Zhang, L., Yang, K. H., and King, A. I., 2001, "Comparison of brain responses between frontal and lateral impacts by finite element modeling," J. Neurotrauma, **18**(1), pp. 21–30.
[39] Carter, D. R., 1984, Biomechanics of bone, Appleton & Lange, The Biomechanics of Trauma.
[40] Hertel, E. S., Bell, R., Elrick, M., Farnsworth, A., Kerley, G., McGlaun, J., Petney, S., Silling, S., and Taylor, P., 1993, "CTH: a software family for multi-dimensional shock physics analysis," Proc. 19th Int. Symp. Shock Waves, **1**, pp. 377–382.
[41] Taylor, P. A., 1995, CTH Reference Manual: The Transverse Isotropic (TI) Model, Sandia National Laboratories.
[42] Friedlander, F. G., 1947, "Simple progressive solutions of the wave equation," Math. Proc. Camb. Philos. Soc., **43**(3), pp. 360–373.
[43] "DPlot User Manual" [Online]. Available: http://www.dplot.com/help/index.htm?helpid_smooth.htm. [Accessed: 07-Sep-2016].
[44] "Modularity in the Nervous System" [Online]. Available: https://www.teco.edu/~albrecht/neuro/html/node28.html. [Accessed: 08-Sep-2016].